ELECTRON LIFETIME AND ITS DEPENDENCE ON TEMPERATURE AND DOSE IN a-Se PHOTOCONDUCTORS

A Thesis Submitted
to the College of Graduate Studies and Research
in Partial Fulfillment of the Requirements
for the Degree of Master of Science
in the Department of Electrical and Computer Engineering
University of Saskatchewan

by

Michael Walornyj

B. Eng

Saskatoon, Saskatchewan, Canada

Permission to Use

In presenting this thesis in partial fulfillment of the requirements for a Postgraduate degree from the University of Saskatchewan, it is agreed that the Libraries of this University may make it freely available for inspection. Permission for copying of this thesis in any manner, in whole or in part, for scholarly purposes may be granted by the professors who supervised this thesis work or, in their absence, by the Head of the Department of Electrical and Computer Engineering or the Dean of the College of Graduate Studies and Research at the University of Saskatchewan. Any copying, publication, or use of this thesis, or parts thereof, for financial gain without the written permission of the author is strictly prohibited. Proper recognition shall be given to the author and to the University of Saskatchewan in any scholarly use which may be made of any material in this thesis.

Request for permission to copy or to make any other use of material in this thesis in whole or in part should be addressed to:

Head of the Department of Electrical and Computer Engineering
57 Campus Drive
University of Saskatchewan
Saskatoon, Saskatchewan, Canada
S7N 5A9

Acknowledgments

I extend my sincerest gratitude towards my supervisor, Dr. S.O. Kasap, for his patience, encouragement and leadership throughout the course of this project. I would like to thank Dr. Robert Johanson for his assistance with the initial design and setup of the experimental system, and would also like to thank Dancho Tonchev and George Belev for their invaluable guidance, support, and assistance. This thesis would not have been possible without the financial support from Analogic Corporation and the University of Saskatchewan.

Abstract

The dependence of electron transport in a-Se x-ray photoconductors on dose and temperature was examined in this work. Recently, stabilized a-Se (amorphous selenium) has been commercialized for use in mammographic screening in flat panel digital x-ray detectors. During the mammographic screening procedure the detector is exposed to x-rays which results in the a-Se undergoing structural change leading to a reduction in detector sensitivity. The detector sensitivity is related to electron lifetime.

Electron transport in vacuum deposited a-Se films has been investigated by Interrupted-Field Time-of-Flight (IFTOF) transient photoconductivity experiments to examine the effect of sample temperature (T) and applied electric field (F) on x-ray induced changes in the electron lifetime, τ_e. Upon exposure to x-rays, the electron lifetime decreases. The decrease in normalized lifetime is almost linearly proportional to the absorbed dose, and is more significant at higher temperatures. Upon the cessation of x-ray irradiation, the lifetime recovers towards its equilibrium value through a structural relaxation process, and is characterized by a structural relaxation time τ_{sr}. τ_{sr} decreases with temperature in an Arrhenius fashion, and exhibits an activation energy that is approximately 1.4 eV. The structural relaxation time at room temperature (21 °C) is 2 - 4 hours whereas at 35 °C, it is $6 - 10$ mins. The results indicate that the rate of change of electron lifetime per unit of exposure is less than 2 %/Gy at room temperature. These measurements are important in characterizing the charge collection efficiency of a-Se based x-ray detectors, and its dependence on x-ray exposure and temperature.

Table of Contents

List of Tables

List of Figures

List of Abbreviations

AB	anti-bonding
AMA	active matrix array
a-Se	amorphous selenium
a-Si:H	hydrogenated amorphous silicon
BJT	bipolar junction transistor
CCD	charge coupled device
CFO	density of states model proposed by Cohen, Fritsche and Ovshinski
CMOS	complementary metal oxide semiconductor
CMRR	common mode rejection ratio
DOS	density of states
DPDT	double pole double throw
EHP	electron hole pair
ESR	electron spin resonance
FET	field effect transistor
FWHM	full-width half-maximum
GPIB	general purpose instrumentation bus
GUI	graphical user interface
HEXFET	hexagonal shaped MOSFET
HV	high voltage
HVIN	high voltage input
HVOUT	high voltage output
IFTOF	interrupted field time-of-flight
ITO	indium tin oxide
IVAP	intimate valence alternation pair
LCD	liquid crystal display
LP	lone pair
MOSFET	metal oxide field effect transistor
MTF	modulation transfer function

NB	non-bonding
NSB	normal structure bonding
PACS	picture archiving and communication systems
PC	personal computer
PCB	printed circuit board
PCI	peripheral component interconnect
PID	proportional with integral and derivative control
PPM	parts per million
RFI	radio frequency interference
SRT	structural recovery time
SCR	silicon controlled rectifier
SNR	signal to noise ratio
SPDT	single pole double throw
SPST	single pole single throw
TFT	thin film transistor
TOF	time-of-flight
TP	transient photoconductivity
VAP	valence alternation pair

1. Digital Radiography and Amorphous Selenium

1.1 Introduction

Radiography is a well established diagnostic tool for medical treatments around the world. Radiography consists of the creation of an image by measuring the differential attenuation of ionising radiation which occurs in an object. The form of ionizing radiation used in radiography are x-rays. An image is developed using a photographic film deployed in cassette form in a film based x-ray image detector. Photographic film is placed in between two fluorescent screens composed of phosphorescent crystal grains which fluoresce when exposed to ionising radiation producing visible light.

Current radiography employing film cassettes which imposes limits on the radiographic medical procedure. Film detectors as compared to digital detectors do not offer real time x-ray image capture or immediate exposure adjustment. As a consequence, a time consuming trial and error procedure must be employed with the exposure level modified only after the film is developed in each iteration. Film being a physical medium, does not lend itself to easy to storage and also poses a problem with duplication and distribution.

There are several advantages to medical radiographic images being developed and stored in a digital format. A digital image allows for computer manipulation. Picture archiving and communication systems (PACS) take advantage of computer networking to share the digital images, offering the potential for remote medical expert assessment.

Another advantage to using an image in digital form is that it allows for the computerized detection and characterization of mass lesions. This technique employs the automated computerized identification of possible masses, several feature-analysis techniques, and the

reporting of possible masses. This computer aided method is made possible by comparing and contrasting images of both breasts [15]. Computerized detection and characterization techniques have already been developed in dental radiography where a radiograph after surgery is compared to a baseline radiograph prior to surgery. By comparing the image intensity in selected regions, a change in bone density can be determined [16].

Digital flat panel detectors generally fall into two categories; direct and indirect conversion detectors. Examples of direct and indirect detectors are shown in Figures 1.3 and 1.4, respectively.

Photoconductors which are used in direct digital x-ray detectors offer several advantages over film detectors. Patient exposure can be reduced with direct detectors as they are more sensitive to x-ray radiation. Lower energy x-rays can be employed due to the increase in sensitivity. Digital x-ray detectors have an advantage over film detectors because computer algorithms can be employed which optimally adjust patient exposure and which reduce the number of exposure adjustment iterations. This has a clear advantage over the alternative trial and error method employed when using film based detectors. Digital images also offer higher image quality and resolution as charge carriers are optimally collected. Charge carriers created through an x-ray attenuation process in the photoconductor travel perpendicular to the detector surface and along electric field lines thus reducing lateral spreading into neighbouring charge collection capacitors. In a film detector, the visible light photons created at the fluorescence screen are scattered in all directions. Emitted light does not follow the same incident path as the x-ray resulting in a loss of resolution. A basic diagram of a film detector is shown in Figure 1.1.

Digital indirect detectors offer many of the same advantages as digital direct detectors except that there is mainly a loss in resolution in digital indirect detectors. The main benefit of a digital indirect detector is a reduction in the manufacturing cost. The cost reduction comes from employing photodiodes in the device structure. The loss in resolution in an indirect detector occurs at the phosphorescent layer placed in between the incident x-ray and the photodiode. The layer is used to convert incident x-rays into visible light. In the process the visible light is scattered resulting in a loss of resolution. This effect can be reduced

by thinning the phosphorescent layer and by reducing the distance to the photodiode.

There are several hardware advantages in converting from a film based detector to a digital detector. The main hardware advantage is that the digital detector fits into a film cassette. An active-matrix array (AMA) panel is used in digital sensors and flat panel displays. Digital sensors using an AMA panel fit into existing film cassette slots allowing for an economical and easy operational transition to digital imaging using existing systems. The conversion is not costly as AMA panels can be economically fabricated with large area thin film deposition techniques.

Several photoconducting materials have been identified which are applicable at the x-ray energies used in mammography. Each photoconductor varies in its x-ray sensitivity, x-ray attenuation efficiency, and electron hole pair (EHP) creation energy. Arsenic containing chalcogenides, especially the selenium rich alloys, belong among the most intensely studied glassy semiconductors due to their physico-chemical properties and due to their glass forming ability. They have won recognition in numerous civil, medical, and military areas [17]. Amorphous selenium (a-Se) has several advantages over other photoconductors. a-Se can be deposited using conventional vacuum deposition techniques onto large area AMA panels. The substrate temperature during deposition does not damage the AMA. a-Se has comparatively low dark current. Its material properties can be changed by alloying the element.

1.1.1 Objectives of the Work

The semiconductor property that was measured in this thesis was the electron deep trapping lifetime. The lifetime is the average duration that a charge carrier exists in the conduction band before it is captured by a deep trap centre. The method that was employed in measuring the electron lifetime was the interrupted-field time-of-flight (IFTOF) technique. This technique uses the conventional time-of-flight (TOF) experiment, which measures the photocurrent that is produced by injected charge carriers moving under an applied electric field across the photoconductor. The IFTOF technique is a modification of the TOF technique in that the charge carriers are briefly interrupted midway in their travel across the photoconductor by the removal of the applied electric field. What is measured us-

ing the IFTOF technique is the fraction of recovered photocurrent after the reapplication of the applied field. By considering the fractional recovered photocurrent and the interruption time, the deep trapping lifetime is calculated. The current just after the interruption is less than the current just before the interruption, as carrier deep trapping takes place during the interruption time.

In this thesis, the IFTOF technique was used to measure the change in lifetime of five a-Se based samples upon exposure to x-ray irradiation as well as the lifetime recovery following x-ray irradiation. Exposure to x-rays leads to certain changes in the structure of the a-Se and therefore in the carrier lifetime. In nearly all observed cases, the lifetime decreased with exposure; due to x-ray induced temporary or permanent structural changes. The decrease in lifetime upon exposure was measured in the "irradiation experiments". The recovery of the lifetime to its equilibrium value following exposure was measured in the "recovery experiments". The irradiation and recovery experiments were performed under a combination of three temperatures (10 °C, 21 °C and 35 °C) and two applied electric fields (0 V/μm, 5 V/μm).

The term that characterized the lifetime decrease upon exposure is referred to in this thesis as the normalized lifetime change rate (NLCR) given by $\left|\frac{d\tau}{dD}\right|$, where τ is the normalized lifetime and D is the absorbed x-ray dose in the bulk of the sample. The term that characterized the exponential lifetime recovery to its equilibrium value was the structural relaxation time (SRT) given by τ_{sr}. NLCR and SRT were terms used in this thesis and are not prevalent in the literature.

The objectives of this work were to observe the change in NLCR and SRT upon absorbed dose under several sample temperatures and applied fields. The sample temperature refers to the temperature of the bulk of the sample. Applied field refers to the electric field created across the sample and applied during irradiation. Detector performance is improved if NLCR and τ_{sr} are reduced.

The study on the effects of x-ray induced lifetime changes relates to photodetector device performance. Device performance is decreased if there is a reduction in lifetime. This

is because at lower lifetime, fewer generated carriers are collected by the detector which results in a lower image intensity. Since x-ray irradiation reduces the normalized lifetime and since full lifetime recovery upon a heavily applied x-ray absorbed dose was observed to take approximately 20 hours on average at room temperature, the operating conditions (applied field and temperature) which minimize x-ray induced lifetime changes and increase the rate of recovery may be of interest in commercial application.

1.2 Radiographic Imaging

Generally speaking there are three main parts to any medical radiographic imaging system. These are the x-ray source, patient, and x-ray detector. The x-ray source produces a homogeneous source of x-rays which pass through the patient and are attenuated at varying degrees. The intensity of the transmitted x-rays are spatially detected by the x-ray detector which is placed in line with the x-ray source. An image is formed by the spacial differences in x-ray attenuation. The operating principles of the x-ray source itself are covered in the experimental procedures section.

X-ray attenuation is an important factor to consider when capturing a radiographic image. X-rays can be controlled via the x-ray tube where they can be produced at a controlled peak energy and intensity. The x-rays pass through a patient where they are attenuated. X-rays are attenuated more in dense matter. As a result there is greater attenuation in bones as compared to tissue. Any unattenuated x-rays are collected by the detector where their spatial intensity is measured.

The x-ray detector measures the integrated intensity on a two dimensional spatial plane. The energy of the x-rays employed is dictated by the medical application. This in turn applies design restrictions on the detector which are namely the chosen photoconducting material and the thickness of the material. In an example application, dense bone matter is imaged in chest x-ray imaging at higher x-ray energy than is used to image breast tissue. Film as an imaging medium employs a phosphorus screen between the patient and detector as shown in Figure 1.1. X-rays originate from the x-ray source, are attenuated in an object and hit a phosphorescent screen where visible light is emitted. The visible light is attenuated

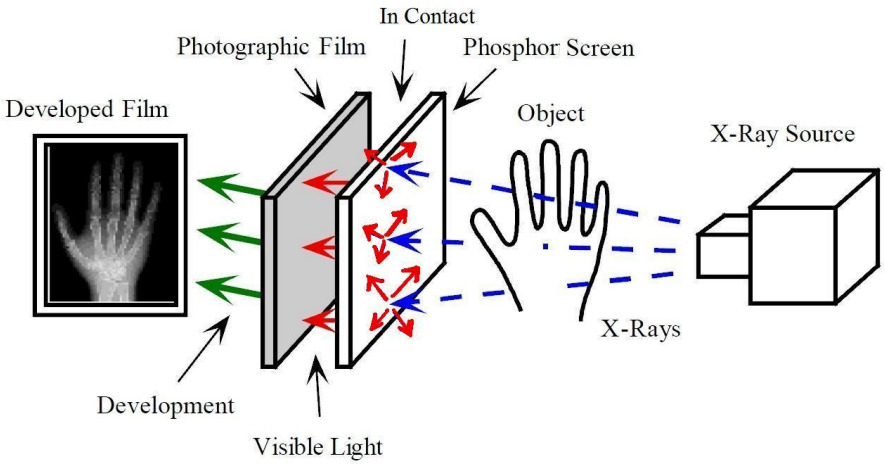

Figure 1.1: Simplified x-ray imaging system utilising a phosphorescent screen and a photographic film. After Allen [2].

in the photographic film. The last stage which is not shown in the figure is the development of the photographic film.

Dynamic range is an important factor to consider in medical radiography as the image contrast plays a key role in distinguishing tissue. Chest x-rays for example require a large dynamic range as density varies widely between bone and tissue. In contrast, mammography requires a small dynamic range in order to contrast soft tissue between either normal or malignant tissue. The required imaging area affects the detector size. Mammographic imaging requires a smaller imaging area than chest radiography. A sample mammogram is provided in Figure 1.2.

1.3 Digital X-ray Imaging

Images can be digitized by either direct or indirect conversion methods. In the direct conversion method, x-ray photons undergo mass and energy attenuation as they travel through the photoconducting material. The x-ray's energy is converted ultimately to pairs of charge carriers which are called an electron-hole pair (EHP). Roughly ten thousand electron hole pairs are created per x-ray photon used in mammography. The typical x-ray photon energy is approximately 20 keV while the bandgap of selenium is 2.2 eV.

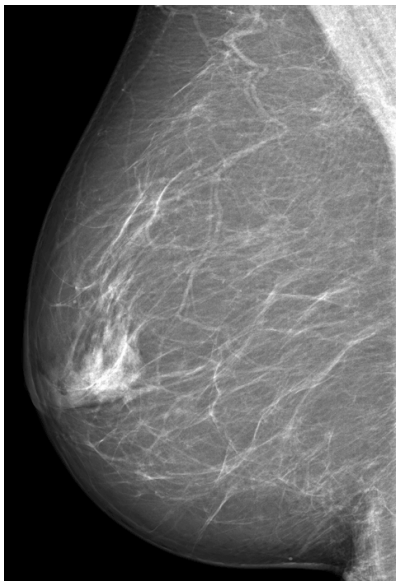

Figure 1.2: A sample mammogram from a direct-converstion flat panel x-ray image detector utilizing stabilized a-Se as a photoconductor. The image is provided courtesy of Analogic Corporation [3].

Klein derived a formula that states the absorbed photon energy (W_o) should be 2.8 times the band gap of the semiconductor [18]. A large number of semiconductors have been found to agree with this formula. EHP formation begins with the attenuation of an x-ray photon and the emission of an energetic primary electron via the photoelectric effect. The energetic primary electron, also known as a ballistic electron, loses energy to ionization events as it collides with atoms in the lattice as well as through lattice vibrations. Each ionized atom has an electron which is excited from the valence band to the conduction band. The excited electron typically has more energy than the bandgap. The additional energy of the ionized electron is lost to lattice scattering events until its velocity reaches the thermal equilibrium velocity of other conduction band electrons [19, 20].

The number of charge carriers created by a photon is proportional to its energy. The EHP creation energy is a material property. The total charge collected is a function of the x-ray beam fluence and duration. The x-ray fluence is the profile of the intensity of photons, at their respective energies, which make up the x-ray beam. The x-ray generated EHPs are collected under an applied electric field in an a-Se direct conversion x-ray detector as shown

in Figure 1.3.

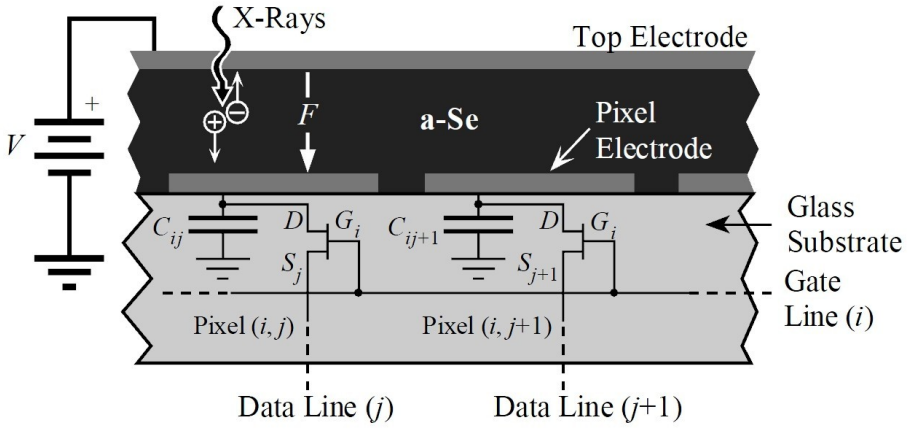

Figure 1.3: Cross-sectional view of an a-Se direct conversion x-ray detector. After Kasap [4].

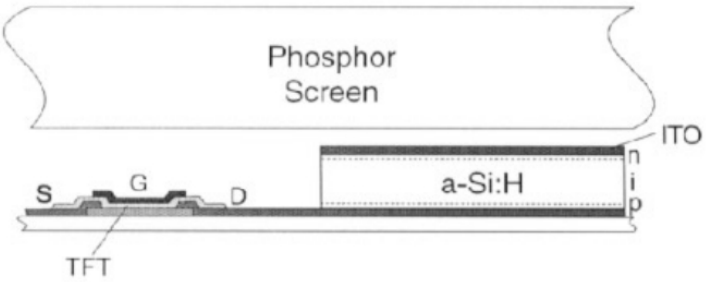

Figure 1.4: Cross-sectional view of an amorphous silicon indirect conversion x-ray detector. After Yaffe [5].

One solid state digital indirect conversion detector design incorporates a luminescent phosphor. The visible light is then converted to EHPs in an a-Si:H photodiode. A TFT acts as a switch controlled by the gate voltage. The switch connects the drain to the source. The signal which results from drifting charge carriers is integrated by the photodiode when the TFT is held in a nonconducting state. The Thin-Film-Transistor (TFT) switch is then switched to a conducting state by gate control circuitry and is read out [21]. A cross sectional view of a solid state indirect detector design is shown in Figure 1.4. The detector uses an n-i-p a-Si photodiode. The top electrode is composed of indium-tin oxide (ITO) and is transparent. The bottom electrode is connected to the drain of the TFT.

In another design a large area phosphorescent screen is composed of a cesium iodide

phosphor acting as an intensifier. The screen is coupled to a CCD camera using fibre optic cables with each cable paired with a pixel [5]. In yet another method of indirect digital conversion known as computer radiography (CR), a photostimulable phosphor system utilises a storage phosphor layer which is read out with a laser scanner [6].

Direct conversion has several advantages over indirect conversion. In digital direct conversion, EHP charge carriers travel parallel to the applied field with relatively insignificant lateral movement. Three factors can be optimized: the photoconductor material band gap can be selected to suit the x-ray energy, the operating bias can be modified to increase the signal strength, and the photoconductor layer thickness can be increased to increase x-ray attenuation [22].

A digital indirect conversion detector has several limiting factors. The limiting factors are the reduction in conversion efficiency of the phosphorescent screen and the reduced resolution as a result of visible light scatter. Many indirect detectors benefit from a columnar phosphor in which the column guides the luminescent light to the photodiode. The result is an increase in resolution.

Capturing the intensity and spatial data in a digital direct conversion detector is accomplished by the use of a large area Active-Matrix-Array (AMA). The technology is based on the amorphous silicon (a-Si:H) AMA device which is used in Liquid Crystal Displays (LCD). In an AMA display, the picture is composed of an $M \times N$ array of pixel elements. Each element contains a charge collection capacitor (C) and a TFT switch.

A cross section of the direct conversion detector is shown in Figure 1.3. In a direct conversion detector an $\sim$ 1 mm layer of a-Se is deposited on top of the AMA array. An electrode is deposited on top of the a-Se to allow for the application of a bias. The applied voltage (V_{DD}) is connected to the photoconductor. The photoconductor is connected to both the capacitor (C) and the TFT. C is connected to ground and the TFT is connected to an output line. The base of the TFT is biased high or low and acts as a switch. C is discharged when the TFT is on. When the TFT is off, the photoconductor is biases to V_{DD} and the photocurrent charges the capacitor.

A section of a direct conversion detector using a thin film transistor active-matrix-array is shown in Figure 5.22. The gate terminals i are connected to a control line. The source terminals j are connected to a common data line. All data lines are read out when a gate line is selectively activated. Each row is consecutively digitized, multiplexed, and transmitted serially to a computer. All circuitry in a digital direct conversion detector is onboard which makes the detector self scanning and compact.

The pixel and array dimensions determine the image resolution and size respectively. Commercial pixel pitch is 85 μm [3, 23] with an AMA scalable to 10^3 cm^2 [24]. The pixel pitch which is most suitable to mammography is 50 μm [25].

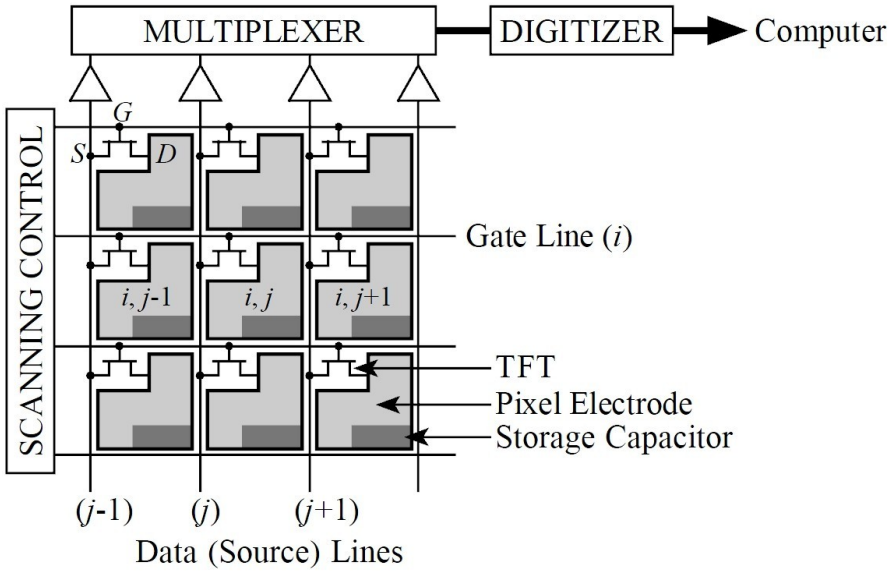

Figure 1.5: A section of a direct conversion detector which employs a thin film transistor active-matrix-array. The detector operates using a self-scanning readout. After Kasap [6].

1.4 X-ray Photoconductor and Detector Performance

Factors affecting detector performance and the properties of an ideal photoconductor material are presented in this section. The detector performance is a function of the charge transport properties, pixel size, and photoconductor (PC) thickness. The measures of performance are the sensitivity (S), quantum efficiency (DQE), and resolution, in terms of the modulation transfer function (MTF) [23].

The sensitivity is dependent on three factors. The first factor is the quantity of absorbed irradiation. The second factor is the charge conversion efficiency. The third factor is the charge collection efficiency. The first factor is characterized by the attenuation coefficient or by the attenuation depth. The second factor is characterized by the EHP creation energy $W\pm$. The third factor is characterized by the range $\mu\tau$. These three characteristics are covered in the next sections.

1.4.1 X-ray Attenuation

X-ray attenuation in a-Se mainly results from the photoelectric effect at low x-ray energies of less than 30 keV [26]. In K-photon generation and reabsorption, an x-ray is absorbed and a primary electron is promoted from an inner atomic shell. X-ray energies in excess of the primary electron's binding energy go towards the electron's kinetic energy. The primary electron's kinetic energy is dissipated by collision events and in the release of other electrons. The released electrons are namely secondary electrons. The vacancy left by the primary electron is replaced by an outer electron. Characteristic radiation is emitted. The characteristic radiation is named after the shell receiving the electron. The energy of the radiation is equal to the difference of the binding energy of both electrons. For example, if the K-shell vacancy is filled by an L or M shell electrons it is called K_α or K_β fluorescence respectively. The fluorescent x-ray can be reabsorbed in the a-Se releasing more electrons. If reabsorption occurs in a lateral direction, a reduction in spatial resolution may occur as well as an increase in image noise [26].

The fractional transmitted x-ray fluence is given by

$$T = \exp(-\alpha(E, Z, d)L), \tag{1.1}$$

where T is the fraction of incident x-ray flux transmitted, α is the attenuation coefficient, and L is material thickness. The attenuation coefficient is a function of photon energy E, atomic number Z, and density d.

The attenuation depth is defined as $\delta = 1/\alpha$. At the attenuation depth, 63% of incident photons are absorbed. At 2δ, 86% of incident photons are absorbed. In mammography the

mean photon energy is 20 keV which corresponds to $\delta = 50$ μm in a-Se. The thickness of a-Se required at 98% attenuation or $(1 - e^{-4})$ is 200 μm. In chest radiography the mean photon energy is 60 keV which would require a thickness of a-Se of $L = 2000$ μm if $L = 2\delta$.

Ideally the material thickness would be infinite which would result in zero transmittance. Increasing the material thickness is not practical for several reasons. The first reason is that non-uniformity of L across the AMA increases with L due to limitations in the manufacturing process [27]. The second reason is that the a-Se material cost increases with L, which impacts the detector unit cost. The third reason is that as L increases, the operating bias must increase in order to maintain the operating field. The magnitude of the operating bias is limited by the dielectric breakdown and by damage to sensitive AMA circuitry. The fourth reason is that as L increases, the probability of charge carrier trapping increases resulting in less charge being collected. The fifth reason is that the likelihood of a carrier becoming trapped for the duration of the experiment increases the further a carrier must travel. The average distance travelled before trapping, known as the *schubweg*, is given by $\mu\tau F$, where μ is the mobility, τ is lifetime, and F is the operating field. L should therefore be in the range of $1/\delta < L < \mu\tau F$.

1.4.2 EHP Creation Energy

A highly energetic electron is promoted to the conduction band when an x-ray photon is absorbed. This ballistic electron travels in the conduction band colliding with other bound electrons causing further ionization. The total amount of charge generated from this process is given by equation (1.2),

$$\Delta Q = \frac{e\Delta E}{W_{\pm}} \tag{1.2}$$

where ΔQ is the generated charge, e is the elementary charge, ΔE is the photon energy, and $W_{\pm}$ is EHP creation energy. $W_{\pm}$ is also known as the ionization energy. The reason for defining $W_{\pm}$ by equation (1.2) is that all experiments indicate that the total charge generated depends on the energy of the x-ray photon. Detector sensitivity is inversely proportional to the EHP creation energy making low bandgap materials desirable for creating a larger quantity of charge upon the attenuation of irradiation (however, narrow bandgap semiconductors

have higher conductivities which leads to higher electronic noise due to the dark current). In crystalline semiconductors, the EHP creation energy $W_{\pm}$ is reasonably well defined and is given by [28],

$$W_{\pm} = 2.8E_g + E_{\text{phonon}}, \tag{1.3}$$

where E_{phonon} is an average energy term that represents phonon processes involved in the EHP creation process. This term is usually very small (< 0.1 eV). E_g is the bandgap energy. Equation (1.4) for crystalline semiconductor includes the conservation of the k-vector and the density of states. $W_{\pm}$ depends on E_g therefore a smaller E_g semiconductor material seems to be a better choice as an x-ray photoconductor. In amorphous semiconductors, there is no k-vector associated with an electron, and the EHP creation energy has been shown to be given by [29]

$$W_{\pm} = 2.2E_g + E_{\text{phonon}}, \tag{1.4}$$

The a-Se case seems to be an exemption. In the presence of an applied field, the following columnar type of recombination limited EHP creation energy has been proposed [30]

$$W_{\pm} \approx W_{\pm}^{o} + \frac{C}{F}, \tag{1.5}$$

where $W_{\pm}^{o}$ is the EHP creation energy under an infinite electric field, C is a constant depending on the photon energy, and F is the electric field. Equation (1.5) seems to describe $W_{\pm}$ in a-Se reasonably well.

1.4.3 Charge Transport and Schubweg Limited Sensitivity

In order for a charge carrier to reach the collecting electrode it must travel through the photoconductor (PC). The velocity is governed by the drift mobility (μ) and the field (F). The product gives the drift velocity. The transit time is the time for a charge carrier to travel across the sample. Assuming the charge carrier is created at the surface of the PC, the transit time is given by $L/\mu F$ where L is the thickness of the PC. The PC contains deep traps which remove charge carriers from the conduction band and thereby prevent these charges from reaching the collecting electrode. The average time a charge carrier exists in the conduction band before it is deep trapped is given by the PC deep trap lifetime (τ). The

detector sensitivity is a measure of how many charge carriers reach the collecting electrode per unit of incident radiation.

The product of $\mu\tau F$ gives the average distance a charge carrier travels before becoming trapped and is called the Schubweg. In order to be collected at the collecting electrode, the charge carrier must travel across the length of the sample L without being trapped. Ideally, the Schubweg should be much larger than L ($\mu\tau F \gg L$) in order to ensure collection. At the same time, L must be kept large enough to maximize x-ray attenuation in order to maximize detector quantum efficiency (DQE) ($L \gg 1/\alpha$). The following relationship should therefore hold $\mu\tau F > L > 1/\alpha$.

With the photoconductor material selected, only F and L can be altered in the above relationship. Increasing L will maximize the detector quantum efficiency A_Q but this will be at the expense of charge collection and in the case of a-Se, also at the expense of charge generation efficiency (See Eq. (1.5)).

1.4.4 Ideal X-ray Photoconductor

The performance of a direct conversion x-ray detector is dependent on the photoconductive layer. An ideal photoconductor has the following properties [31]

1. High x-ray attenuation efficiency.
2. Small EHP creation energy.
3. Minimal dark current.
4. Minimal bulk carrier recombination.
5. Minimal deep trapping.
6. Carrier transit time shorter than pixel access time.
7. Minimal x-ray induced structural change.
8. Underlying AMA circuit should be able to be coated without damage to sensitive electronics.

Ideally, to reduce the probability of trapping, the mobility and lifetime product should be large, as should be the field $\mu\tau F \gg L$. To ensure good x-ray photogeneration efficiency, the EHP creation energy must be as small as possible.

Choosing a PC with a larger bandgap, and therefore large EHP creation energy, can minimize the dark current and increase SNR. The current can also be limited to bulk thermal generation when electrical contacts are totally blocking [30]. The desire to raise SNR must be balanced with the previously stated ideal of a small EHP creation energy, which requires a small bandgap.

Amorphous selenium is a photoconductor which is in use in mammographic detectors. The material has acceptable x-ray attenuation efficiency, good carrier transport, and low dark current. In a commercial detector, a-Se is deposited onto an AMA array of dimensions $40\,\text{cm} \times 40\,\text{cm}$. During evaporation, TFTs located on the array are not damaged because TFT damage occurs at $\sim$ 300 °C while the substrate temperature during evaporation is $60 - 70$ °C. The behaviour of a-Se and its alloys is well established through extensive study in electrophotographic and xeroradiographic applications [4, 32].

1.5 Research Objectives

The dependence of electron transport in a-Se x-ray photoconductors on dose and temperature will be examined in this work. Electron transport in vacuum deposited a-Se films will be investigated by Interrupted-Field Time-of-Flight (IFTOF) transient photoconductivity experiments to examine the effect of sample temperature (T) and applied electric field (F) on x-ray induced changes in the electron lifetime, τ_e. These measurements are important in characterizing the charge collection efficiency of a-Se based x-ray detectors, and its dependence on x-ray exposure and temperature.

The dependence of the electron lifetime on the absorbed dose will be studied in this work. The magnitude of the change in electron lifetime upon an absorbed x-ray dose will be measured with the IFTOF technique. The temperature and field dependence of this change will be reported. It is expected that upon the cessation of x-ray irradiation, the lifetime will

recovers towards its equilibrium value. The recovery of electron lifetime upon the cessation of an absorbed x-ray dose will be measured using the IFTOF technique. The dependence of the lifetime recovery on temperature and field will be reported.

Mathematical expressions will be selected which best fit the irradiation experiment data and the recovery experiment data. A mathematical expression relating the change in electron lifetime with absorbed dose will be selected. A mathematical expression for the relaxation process will be selected. An inference as to the fundamental structural changes will be made based on the mathematical expressions. The inference will attempt to relate the observations to basic background structural theory.

1.6 Thesis Outline

This chapter provided an outline of both digital radiography and direct-conversion flat panel detectors. An x-ray sensitive photodetector such as a-Se is used in the direct conversion of an x-ray into electrical charge carriers. These carriers are collected providing intensity information and a read out using a TFT AMA provides spatial information. The detector type is compact, self-scanning, and produces high-quality digital x-ray images. a-Se is a good photodetector material due to factors such as: its ability to be coated onto a large-area AMA without damaging sensitive electronics, good x-ray sensitivity, small dark current, and good transport properties.

The rest of the thesis is presented in five chapters. In Chapter 2, electrical properties of a-Se are explained using a band model. In Chapter 3, the principles behind the TOF and IFTOF techniques are described, and the techniques outlined. Derivation of several theoretical expressions for the TOF transient photocurrent are covered. In Chapter 4, the experimental apparatus used in this work and the methodology used to create the a-Se samples are described. In Chapter 5, the results and discussion from the measurements of the irradiation and recovery experiments are presented. Finally, in Chapter 6 the conclusions from the experimental work are presented.

2. Theory

2.1 Introduction

Amorphous selenium and its alloys were intensely studied in the 1960s and 1970s for their commercial xerography application. Renewed research interest has resulted from the commercial application of flat panel x-ray detectors for use in medical imaging. Large area thin film deposition techniques can be applied to amorphous selenium. a-Se is therefore suitable for the manufacture of large area chest detectors. A detector's sensitivity is affected by the optical and electronic properties of the constituting semiconductor material. Device performance can therefore be optimized by altering the semiconductor's material properties.

The band theory of solids is a well recognized model which is derived from quantum mechanics. It is applied in a modified and simplified form to noncrystalline semiconductors. Solid state devices have either a crystalline or amorphous structure. The structures differ in atomic arrangement. A periodic arrangement is observed in a crystalline solid whereas an arrangement lacking in long range order is observed in an amorphous solid. Crystalline solids have a periodic lattice structure. The mathematical models used to describe these structures are simplified due to the structure's periodicity. The band model used to describe the amorphous structure is modified from the crystalline band model. The modifications are based on hypotheses founded in experimental observation.

2.2 Semiconductor Atomic Structure

A solid is a three dimensional networks of atoms. The probable location of an atom's electron is given by its ground state wave function. In a solid the atoms are close enough

together that their electrons interact and their wave functions overlap. Covalent bonding can be understood by considering the atom's ground state wave function. A selenium atom in its ground state lacks the valence shell electrons to fill its outer orbitals. For a selenium atom sufficiently far away from a neighbouring selenium atom the probability of finding an electron is localized around the atom. If two atoms are brought together to form a covalent bond the ground state wave functions overlap over the distance between the two atoms.

The bonding arrangement for a crystalline and amorphous semiconductor is illustrated in Figure 2.1. A bond is represented by a line. The position of an atom at equilibrium is represented by a sphere. The highly ordered arrangement of the crystalline structure is depicted in Figure 2.1 (a). A crystalline structure exhibits the same coordination number, bond lengths, and bond angles for all atoms. Long range order throughout the bulk of the solid results from the network's periodicity.

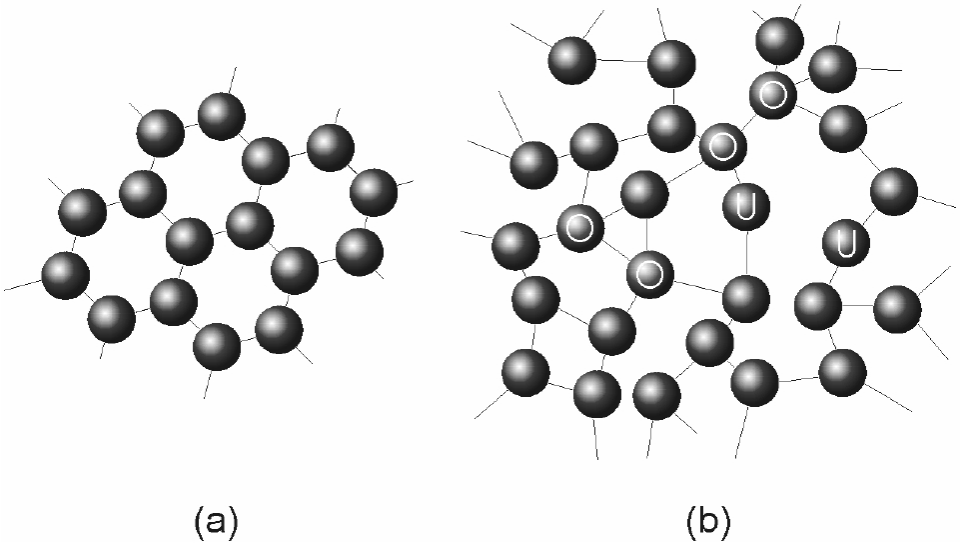

Figure 2.1: Representation in two dimensions of a three dimensional atomic structure. A crystalline semiconductor is represented in (a) and an amorphous semiconductor is represented in (b). Over-coordinated and under-coordinated atoms are represented by O and U respectively. After Fogal [1].

There is a variation in the bond length and bond angle in an amorphous semiconductor which results in a periodicity of only a few atomic radii. Crystalline and amorphous electronic structures are similar under short-range order. Disorder in the amorphous network causes the

localization of the electron wave function resulting in localized electronic states. The optical and electronic properties of an amorphous semiconductor is determined by the physical location within the material, the energy level, and density of states.

Optical and electronic properties of crystalline and amorphous semiconductors are also affected by defects in the atomic structure. Defects are classified differently in crystalline and amorphous semiconductors. A defect in a crystalline semiconductor is classified as an atom which is not in its equilibrium position. A defect in an amorphous semiconductor is classified as an atom with incorrect coordination number. The coordination number is also referred to as the normal structural bonding (NSB). Position cannot be used to define a defect in an amorphous semiconductor since position is not a practicable reference point [33]. Amorphous defects are categorized as under-coordinated (U) or over-coordinated (O) as shown in Figure 2.1 (b). A localized electronic state is located at each defect.

2.3 Density of States Theory

The band model of solids is used to explain electronic and optical properties of semiconductor materials. The model describes the behaviour of electrons in a solid by using quantum mechanics. The model is derived from an application of quantum mechanics in which atoms are brought from a distance into close proximity to form a solid. Discrete electron energy states exist in a single atom in infinite space. Virtually continuous electron energy states exist for each atom in a solid. The density of states function $g(E)$ describes the density of electron states for a given energy E.

An energy band refers to a range of electron energy density of states. There are two energy bands in metals which are the valence band and the conduction band. Valence band states are involved in bonding. The conduction current is the result of electrons travelling in the conduction band. In a metal the valence and conduction bands overlap. In a metal, a nearly continuous electron energy range exists above the valence band.

Figure 2.2 (a) is an illustration of an energy band diagram for a crystalline semiconductor. A *band gap* of forbidden energy states exists in a crystalline semiconductor. The forbidden

gap exists between the conduction band and valence band. An increase in electron energy in which the electron moves from the valence band to the conduction band is accompanied by the absorption by the electron of energy equal to or greater than the band gap energy. The conduction and valence band edges are denoted E_c and E_v, respectively. The energy level at which the probability of occupancy is 1/2 is the Fermi energy E_F and is dictated by the Fermi-Dirac function $f(E)$.

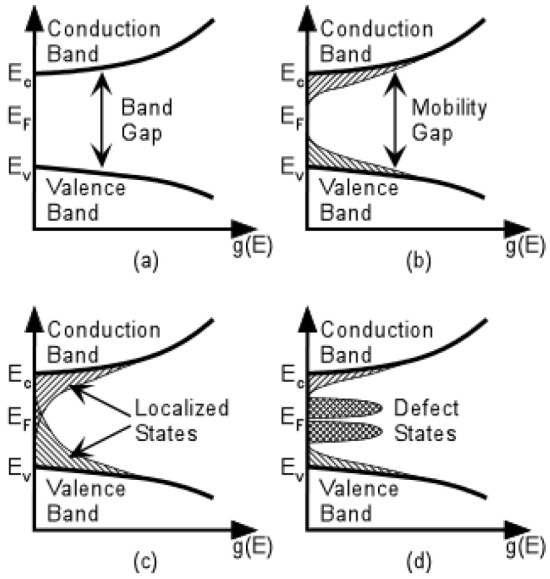

Figure 2.2: Four Density of States (DOS) models. All DOS models represent amorphous semiconductors except for (a) which is for crystalline semiconductors. Localized states are indicated by the shaded regions. Localized states occur in the band gap. (a) The crystalline DOS model. (b) The Mott model in which localized states encroach. (c) The CFO model in which localized states extend continuously. (d) Marshall and Owen model in which localized states occur deep in the band gap. After Fogal [1].

A density of states derivation for amorphous semiconductors cannot be determined quantitatively due to of a lack of topological order. Similarities in the electronic properties and optical properties between crystalline and amorphous semiconductors have been observed [34]. A similarity in short range order can therefore be concluded.

A band model for amorphous semiconductors was first proposed by N.F. Mott in the 1960s [35]. The following universal features were noted:

1. Bloch wave-functions which possesses long range order in both amplitude and phase can be used to describe crystal electrons.

2. A gap of "forbidden" energies which are well defined separates the allowable bands of electron energies.

A universal characteristics assumption is made by Mott for all amorphous semiconductors. Mott postulated that the Bloch wavefunction's amplitude has long-range order and that its phase has short-range order. The model predicts that localized states encroach into the band gap.

The Mott model is influenced by the solution to a random network developed by P.W. Anderson in 1958 [36]. The model postulates the existence of Anderson electronic states which are defined by their energy and density. The distribution of state energies and state densities spreads with the randomness of the network. The Anderson model is limited as it does not account for lattice imperfections.

The Mott model DOS diagram is shown in Figure 2.2 (b). Localized states encroach into the energy band gap. The localized states begin at the band edges E_v and E_c, and trail off into the forbidden energy gap region. The localized and extended band states are postulated to be well defined due to an abrupt change in electron mobility [37]. Mobility in the extended states is finite and determined by the effective mass of the electron.

An extension to the Mott model was performed by Cohen, Fritzsche and Ovshinksi [38]. The CFO model is shown in Figure 2.2 (c). The CFO model argues that the topological and compositional disorder is more pronounced. Localized states extend continuously into the band gap and overlap at the Fermi level. Metallic conduction does not take place as continuity does not exist locally as gap states are highly localized in space.

Local states exist outside of those described by the normal structural bonding (NSB) of the CFO model. These states occur locally and do not appear on the CFO DOS diagram. These states are a result of defects such as dangling bonds, chain ends, vacancies, substitutional impurities, and interstitials.

Local defect states are assumed to be in much larger concentration in the Marshal and Owen model [39] shown in Figure 2.2 (d). Two bands of highly concentrated local defect states appear above and below the Fermi level and act as donor- and acceptor-like states. A self-compensating mechanism ensures each band is of equal concentration. These bands have been found to have significant impact on electronic properties even in small concentrations.

2.4 Amorphous Selenium Atomic Structure

Selenium is a chalcogen found in group VI of the periodic table. The valence shell is comprised of two electrons in s-states and up to six in p-states. Selenium has an atomic number of thirty four (Z=34). It has twenty eight inner core electrons and six valence shell electrons. The two s-state electrons form lone pairs (LP). A LP is a non-bonding state. In most cases a p-state LP exists. The remaining two p-state electrons are free for covalent bonding. Selenium atoms have a two-fold coordinated bonding configuration. The optimum bond angle is 105° [7].

The crystalline form exists in two phases as a result of two-fold coordinated bonding. The two phases are α-monoclinic Se (α-Se) and trigonal Se (γ-Se). α-Se is composed of Se_8 rings. γ-Se is composed of trigonal molecules arranged in a parallel spiral chain (Se_n).

The amorphous phase has a two-fold coordinated chain structure. The dihedral angle has a constant magnitude but random varying sign [40]. The dihedral angle is the angle between two adjacent bonding planes and is illustrated in Figure 2.3. Intersection of the two planes occurs along the bond between the second and third atoms.

Atomic position is fixed by symmetry, bond length r, and bond angle θ in the crystalline phase of selenium. The magnitude of ϕ is a function of r and θ. The sign of ϕ in γ-Se varies so as to form a spiral structure, in α-Se it varies so as to form a ring structure, and in a-Se it varies randomly to form either a ring-like or chain-like structure. If the relative phase of ϕ is allowed to be given by the symbols + and -, a ring like structure is expressed as $+-+-$. A chain-like structure is expressed as either $++++$ or $----$ [7].

Structural studies of a-Se have revealed a characteristic ϕ sequence [41, 42] illustrated

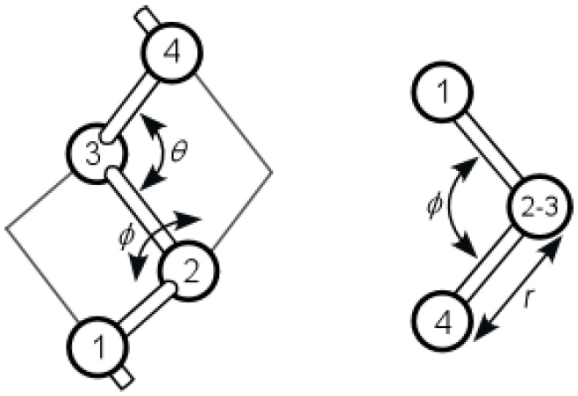

Figure 2.3: Molecular structure illustration for the molecule constituting the random chain model of amorphous selenium. Dihedral angle is given by ϕ. Bond angle is given by θ. Bond length is given by r. After Kasap [4].

in Figure 2.4. The ϕ sequence is $+++-+-+--$. Se_8-like spectral features have been explained by this ϕ sequence in infrared spectra and Raman scattering spectra. Local molecular order is implied by the ϕ sequence.

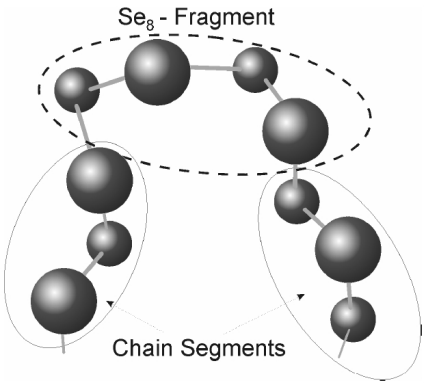

Figure 2.4: An illustration of the ϕ sequence of the random chain model which can be used to explain the infrared spectra and Raman scattering spectra features. After Lucovsky [7].

a-Se contains under- and over- coordinated atoms. Bonding configurations are shown in Figure 2.5 for selenium. The two-fold coordinated state is denoted by Se_2^0. It is the lowest energy bonding state. This bonding state is involved in normal structural bonding. The trigonally coordinated bonding state is denoted by Se_3^0. It forms an electrically neutral defect of lowest energy. The single coordinated bonding state is denoted by Se_1^0. It is a neutral defect state.

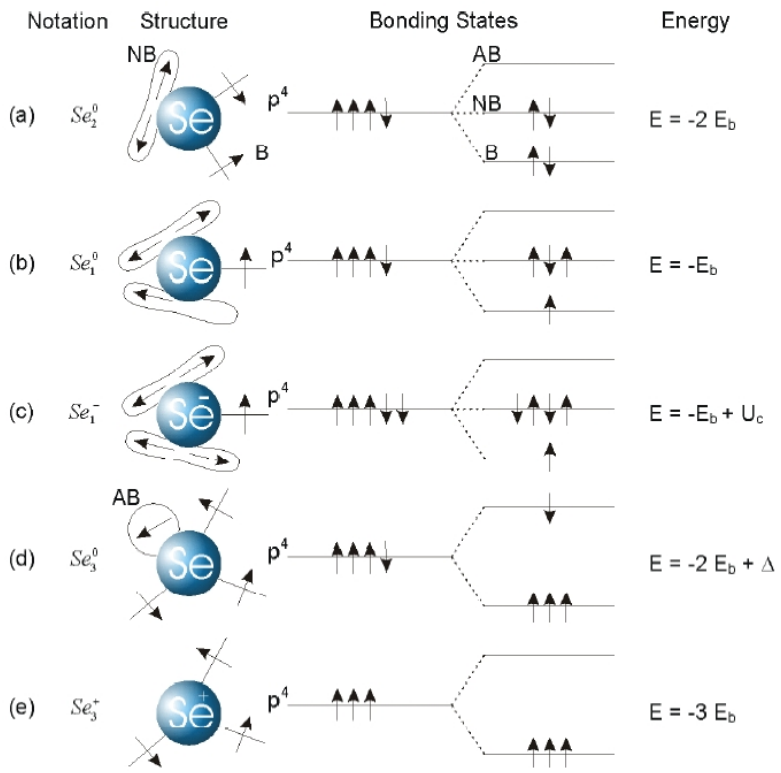

Figure 2.5: Simple bonding configuration structure and energy for selenium. A straight line is a bonding orbital. A lobe is a lone-pair. A circle is an antibonding orbital. Lone pairs have zero energy. After Adler [8]

There are several bonding arrangements in a-Se. There are no unpaired bonds in a-Se [43, 44] as confirmed by the absence of a signal in electron spin resonance (ESR). A valence alternation pair (VAP) is a suspected defect in a-Se. The concentration is believed to be large at approximately $10^{20} - 10^{28}$ cm^{-3}. The VAP defects are indicated by Se_1^- and Se_3^+ in Figure 2.5.

A diagmagnetic pair of VAP centres is formed in a-Se because it is energetically more favourable than a single bonded defect or trigonal defect. A diagmagnetic pair is a pair of VAP centres one of which is over-coordinated and the other under-coordinated. An energetically favourable arrangement exists in an intimate valence alternating pair (IVAP). An IVAP is formed because the energy of Se_1^0 is lowered by this arrangement. A schematic representation of an IVAP centre is illustrated in Figure 2.6. The VAP reaction is shown in Equation (2.1). Lone pair electrons join the dative bonding scheme of the a-Se chain. The

resulting reaction is exothermic.

$$Se_2^0 + Se_2^0 \rightarrow Se_1^- + Se_3^+ \tag{2.1}$$

Certain photoelectric properties of a-Se can be explained with VAP- and IVAP-type defects.

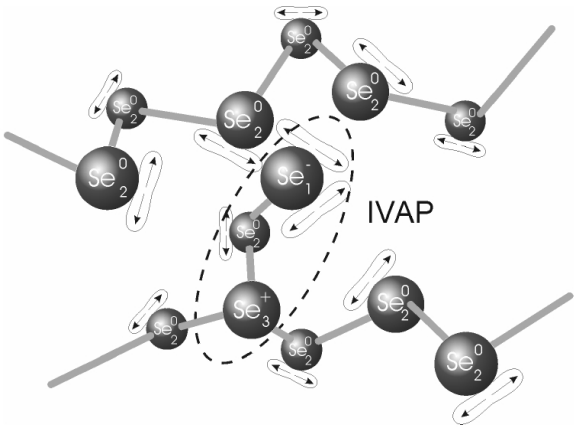

Figure 2.6: Illustration of the a-Se structure indicating an IVAP defect. After Fogal [1].

A fundamental physics explanation of such properties is found in the literature [45, 46]. As an example, these defect states can be used to explain the linearly dependent relationship between photoconductivity and light intensity [47].

2.5 Properties

a-Se and its alloys were studied during the 1960s and 1970s because of their commercial application to xerography. A density-of-states (DOS) diagram is used to interpret the experimental observation of the electronic and optical properties of a-Se. No universal agreement exists as to the exact shape of the DOS diagram. The properties of a-Se are explained in this section in relation to the most accepted DOS function.

2.5.1 Density of States

The currently held DOS model for a-Se is the Abkowitz model proposed in 1988 [9]. The Abkowitz model is an extension of the Marshall and Owen model. The type of experiment performed to derive the model includes: time-of-flight (TOF), xerographic cycled-up residual voltage decay, and xerographic dark discharge. The Abkowitz model DOS is illustrated in

Figure 2.7. The band gap energy is 2.22 eV. The Fermi energy is 1.06 eV. The notable difference in the Abkowitz model as compared to the Marshall and Owen model is that there are four localized energy state ranges which occur at a higher density. A higher density of localized states is represented by a horizontal peak in the figure. Shallow electron trap states occur near the conduction band. Shallow hole trap states occur near the valence band. Electron deep trap states occur near to but above the Fermi level. Hole deep traps occur near to but below the Fermi level.

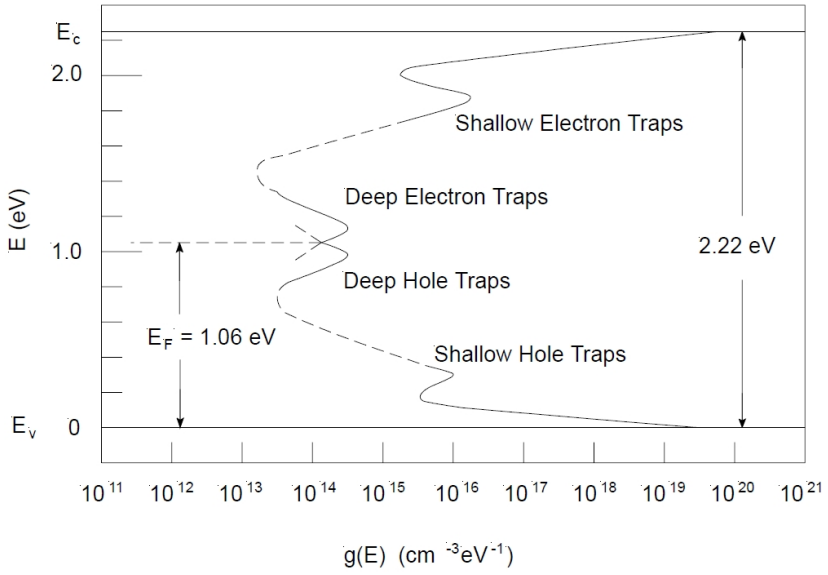

Figure 2.7: DOS function for the Abkowitz model for a-Se. After Abkowitz [9].

The drift mobility for electrons and holes can be measured in a-Se. Experimental observation suggest that the carrier release from shallow traps is thermally activated at low temperatures. It is suggested that the mobility is shallow trap controlled [48]. The presence of shallow traps reduces mobility because trapped carriers lose their velocity. The microscopic mobility $\mu_\circ$ of the extended states is reduced by trapping and release events between extended and localized states as described in Equation (2.2)

$$\mu = \theta\mu_\circ = \frac{p_{\text{free}}}{p_{\text{free}} + p_{\text{trapped}}}\mu_\circ, \tag{2.2}$$

Where θ is the mobility reduction factor [49], p_{free} is the concentration of carriers in the transport band, and p_{trapped} is the concentration of carriers which occupy shallow traps. The

above carrier concentrations are constant once an equilibrium is reached by trapping and release events.

Hole mobility is [4]

$$\mu = \mu_\circ \left[1 + \frac{N_t}{N_v}\exp\left(\frac{E_t}{kT}\right)\right]^{-1} \approx \mu_\circ \frac{N_v}{N_t}\exp\left(-\frac{E_t}{kT}\right), \tag{2.3}$$

for discrete monoenergetic traps. N_t is the shallow trap concentration, N_v is the density of states at E_v, and E_t is the difference in energy between E_v and the shallow trap energy. An Arhenius expression of mobility results when assuming $p_{\text{trapped}} \gg p_{\text{free}}$ which is the case when thermal excitation is sufficiently reduced at low temperature. $\mu_\circ$ approached μ with an increase in the temperature.

The shallow trap energy is determined experimentally. A regression fit is performed using Equation (2.3) on an experimental dataset containing mobility versus temperature. The peak density of shallow electron traps occurs at 0.35 eV below E_c. The peak density of shallow hole traps occurs at 0.29 eV above E_v.

The $\mu_\circ$ of holes is $\sim 0.3 - 0.4$ cm^2/Vs at room temperature [50–52]. The $\mu_\circ$ is inversely proportional to temperature i.e. $\mu_\circ \propto T^{-1}$ exhibiting a diffusive relation.

Deep trap energies are determined by photoinduced discharge measurements and cycled-up xerographic residual voltage measurements. The peak density of deep electron traps occurs at 1.22 eV below E_c. The peak density of deep hole traps occurs at 0.87 eV above E_v. The peak density of deep hole traps is 0.85 eV by cycled time of flight experiments [53].

The localized state densities decay exponentially from the band edge into the band gap. The experimental techniques employed were microwave strip-line techniques employing both carriers. The measurements taken in the experiments were picosecond-resolution transient photoconductivity measurements [54].

a-Se is more suitable than similar amorphous semiconductors in photodetector application because of the low concentration of deep trap states.

Localized states are caused by structural defects [55–57]. These defects are thermodynamically stable at room temperature. They cannot be eliminated by careful preparation

methods or by source material purification [55]. The nature of the defects is not conclusively known however it is currently accepted that they are caused by VAP defects. Important material properties are determined by the defects. These properties are: the carrier lifetime and the trapping time. Photoconductor x-ray sensitivity and device performance are also affected by altering these properties.

Transport properties of a-Se are affected by alloying. Pure a-Se crystallizes over a period of months to years. The crystallization rate is affected by ambient conditions [58]. The crystallization rate is reduced by alloying with arsenic at $0.2\% - 0.5\%$. Arsenic increases viscosity by linking Se chains. Arsenic is a suitable element as it has a valency of III allowing it to be triply bonded when linking a-Se chains. Arsenic has the disadvantage of adding hole traps. This occurs because As increases the VAP defect density responsible for hole traps. This effect can be reduced with the addition of a halogen in the parts per million range such as chlorine.

Thermal stability and carrier transport are improved by alloying a-Se with As and Cl. a-Se alloyed with As and Cl is referred to as *stabalized a-Se*. The notation for stabilized a-Se is given for example as a-Se:0.2%As +10 ppm Cl. Fundamental research is ongoing on the effects of the compensation effect of As and Cl on the charge transport properties of a-Se [50, 59]. The charge transport properties of stabilized a-Se for a typical stabilized a-Se composition is given in Table 2.1.

An alternative DOS for a-Se is determined from post-transit photoconductivity experiments [60]. The peak density of shallow hole traps occurs at 0.40 eV above E_v. The peak density of shallow hole traps is 0.55 eV below E_c.

Carrier mobility is affected by a distribution of localized states. The localized states extend over an energy range ΔE from the band edges. The carrier mobility as a function of ΔE and temperature is given in Equation (2.4)

$$\mu = \mu_\circ \left(\frac{\Delta E}{kT}\right)^n \exp\left(-\frac{\Delta E}{kT}\right). \tag{2.4}$$

The density of states N_v decays to zero from E_v to $E_v + \Delta E$. The model does not account for energies above $E_v + \Delta E$. Deep trapping states are not defined by this model as a result.

Table 2.1: The transport properties of stabilized a-Se (a-Se:0.2-0.5% As + 10-40 ppm Cl) photoconductor films. After Fogal [1].

Property	**Typical Range**	$\mu\tau F$ **@ 5 V/μm**	**Comment**
Hole mobility μ_h **(cm²/Vs)**	0.12 – 0.14		well reproducible, probably shallow trap controlled
Electron mobility μ_e **(cm²/Vs)**	0.003 – 0.006		decreases rapidly with As addition, probably shallow trap controlled.
Hole lifetime τ_h **(μs)**	20 – 200	1.2 - 12 mm	depends on the substrate temperature
Electron lifetime τ_e **(μs)**	200 – 1000	0.3 – 1.5 mm	sensitive to small quantities of impurities
Hole range $\mu_h\tau_h$ **(cm²/V)**	2×10^{-6} to 2×10^{-5}		substantially higher than PbI_2
Electron range $\mu_e\tau_e$ **(cm²/V)**	1×10^{-6} to 6×10^{-6}		somewhat higher than PbI_2

2.5.2 Optical Properties

a-Se is a photoconductor. A valence band electron will absorb an optical photon if incident and of sufficient energy and will be promoted to the conduction band. The optical absorption coefficient α describes the probability that absorption will occur. α is dependant on the energy of the incident photon and the concentration of band edge states. The absorption of incident photons is negligeable at an energy which is less than the band gap. The absorption coefficient is much larger at an incident photon energy which is larger or equal to the band gap than it is below the band gap energy.

An Urbach edge of the form $\alpha(h\nu) = 7.35 \times 10^{-12} \exp(h\nu/0.058)$ eV cm^{-1} has been experimentally observed in a-Se [61]. The Urbach edge indicates absorption by mid-gap localized states. α is given by $\alpha(h\nu) \approx (h\nu - E_\circ)$ for an optical photon of energy equal to the band gap energy ($E_\circ \approx$ 2.05 eV at room temperature) [62]. Absorption at the valence band edge is therefore indicated. A Tauc's law dependence of $\alpha(h\nu) \approx (h\nu - E_\circ)^2$ is observed

when the optical band gap is $E_\circ \approx 1.9$ eV [63].

An electron-hole pair (EHP) refers to an electron and to a vacant valence band state. The vacant valence band state is referred to as a hole. The electron absorbs an optical photon and is promoted from the valence band to the conduction band. A conduction current is created by the application of an electric field. Promoted electrons in the conduction band contribute to the conduction current. Recombination of electrons and holes can occur. The applied field is inversely proportional to the rate of recombination. The probability of recombination is given by the quantum efficiency η. Both α and η are dependent on the optical photon energy as shown in Figure 2.8. α is proportional to the optical photon energy. η is inversely proportional to optical photon energy.

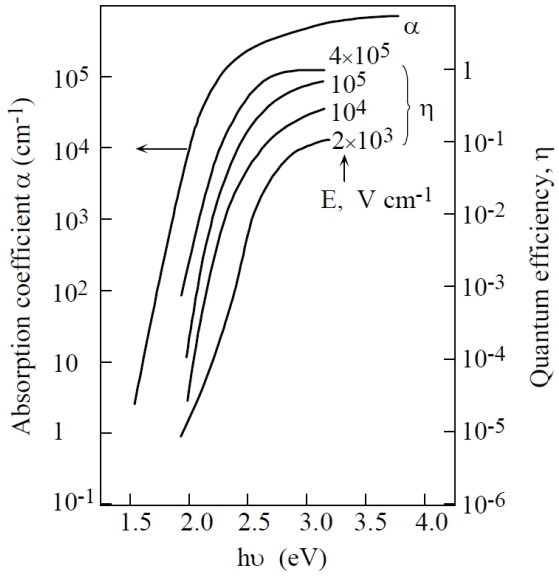

Figure 2.8: The absorption coefficient α and quantum efficiency η in a-Se as a function of incident photon energy hv at various applied fields. After Pai [10].

2.6 Summary

A theoretical framework of the electronic and optical properties of amorphous selenium and its alloys has been reviewed in this chapter. The electronic and optical properties of a-Se are modelled with the modern band theory of solids. The derivation of the band theory involves a quantum mechanics interpretation of electron behaviour when atoms form a solid.

An analytical derivation cannot be performed for amorphous semiconductors due to the lack of long-range periodicity. The development of an amorphous band model results from similarities in the electrical and optical properties with crystalline semiconductors.

A common bonding arrangement exists in a-Se. The dihedral angle phase varies randomly in a-Se. Localized electronic states in the band gap exist as the result. Thermodynamically stable VAP states also exist in the band gap. The electronic and optical properties vary greatly with slight changes to the localized band gap state concentration.

Electronic and optical properties of a-Se relate directly to the DOS function. Experimental research has been performed to develop a generalized shape of the DOS function. There are several proposed DOS functions. The disorder in the structure of a-Se results in localized tail states which encroach into the band gap. VAP type defects introduce additional localized states into the band gap. The carrier mobility is controlled by localized states near the band edge through multiple trapping and release events. The lifetime is controlled by midgap states. There has yet to be universal agreement as to the correct DOS function.

3. Principles and Techniques

3.1 Introduction

Amorphous semiconductors are particularly well suited for large-area solid-state devices due to economic fabrication techniques and acceptable device performance. Device performance is determined by the charge transport properties of the amorphous material. The disordered state of these materials makes the theoretical prediction of charge transport properties difficult. Direct measurement using the time-of-flight (TOF) and interrupted-field time-of-flight (IFTOF) transient photoconductivity techniques is useful in determining the mobility and deep trapping time respectively. This section presents the principles of the TOF and IFTOF techniques. It also presents an interpretation of the photocurrent waveform by relating its shape to transport and trapping conditions.

3.2 The Time-of-Flight Transient Photoconductivity Technique

The time-of-flight technique measures external transient current (the photocurrent) as photoinjected charge carriers drift across a highly resistive medium. A schematic of the TOF technique is shown in Figure 3.1. The photoconducting material is placed in between two electrode plates A and B. Plate A is connected to a voltage source. Plate B is connected to a resistor which is grounded. Sometimes a non-injecting or thin blocking layer is placed between the electrodes and photoconducting material to prevent charge injection. Charge is injected via photoexcitation. The excitation source is attenuated by a factor of 0.37 in the material just beneath the surface at a an absorption depth of $\delta = 1/\alpha$, where α is the wavelength dependent absorption coefficient. A pulse of highly absorbed light photogenerates electrons and holes near the electrode. Electrons are neutralized almost immediately as the

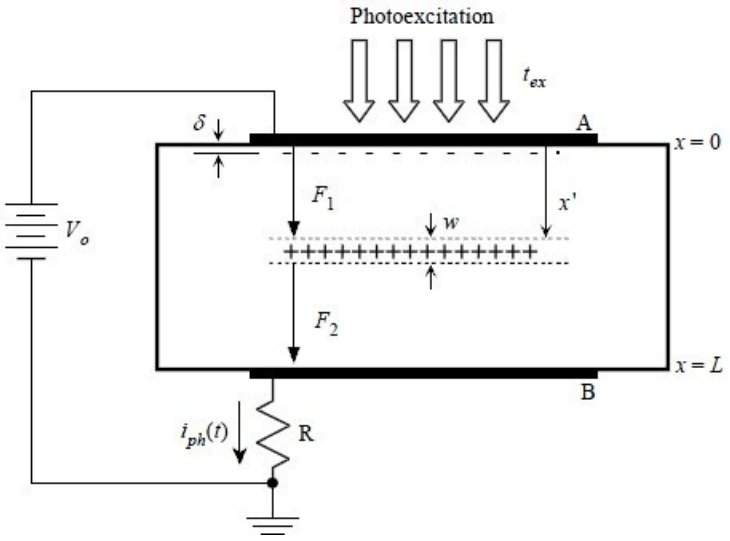

Figure 3.1: Schematic diagram of the TOF measurement technique. After Allen [2].

absorption depth is very narrow (they quickly reach A). Holes, on the other hand, are drifted by the field through the medium. These holes are called photoinjected carriers. Under the applied electric field, holes travel across the sample to form the transient photocurrent in the external circuit. As the charge sheet moves, an induced current is produced across the sampling resistor R. By reversing the bias voltage the transient photocurrent of the opposite carrier type (electrons) can be measured.

Mathematical assumptions are made which simplify the semiconductor characterisation calculations that determine the mobility and lifetime. As a consequence, constraints are imposed on the TOF and IFTOF experiments. First, only one type of transiting carrier must be present which means that the excitation source should be selected to have the shortest absorption depth but not short enough for surface defects to play a role by trapping or recombining with charge carriers. Secondly, the charge sheet should be much more narrow than the thickness of the material which is achieved by minimizing the duration of the excitation pulse provided that $\delta \ll L$. Thirdly, the amount of injected charge should be kept to a minimum by operating the excitation source at low intensities to ensure that the charge sheet doesn't perturb the internal electric field. The small signal condition refers to TOF measurements in which the photoinjected charge perturbs the field by a negligible amount.

The injected charge sheet has the ability to perturb the electric field across A and B should the quantity of injected charge exceed the small signal conditions. The assumption that the charge packet moves at a uniform velocity does not hold if the small signal condition regime is violated. When considering positive charge carriers, Equations (3.1) and (3.2) represent the enhanced field in front of the moving charge packet F_1 and the reduced field behind the moving charge packet F_2 [64]. The fields F_1 and F_2 are given by

$$F_2 = F_0 + \frac{ep_o w}{\epsilon}\frac{x^{'}}{L} \tag{3.1}$$

$$F_1 = F_0 + \frac{ep_o w}{\epsilon}\left[\frac{x^{'}}{L} - 1\right], \tag{3.2}$$

where the unperturbed field between A and B is F_0, the concentration of holes in the charge sheet is p_o, the position of the charge sheet from the surface is given by $x^{'}$, and the width of the sheet is w. The dielectric permittivity of the solid is ϵ. The dielectric permittivity is defined by $\epsilon = \epsilon_\circ \epsilon_r$, where $\epsilon_\circ$ is the absolute permittivity and ϵ_r is the relative permittivity. F_0 is simply given by $V_\circ/L$. The field in front of the charge sheet is enhanced while behind, it is decreased.

For the effect of field enhancement to be much smaller than the unperturbed field F_0, the following expression must be true

$$\frac{ep_o w}{\epsilon} \ll \frac{V_\circ}{L}. \tag{3.3}$$

The above condition is equivalent to requiring the charge on the capacitor plates to be much larger than the injected charge. The charge on the capacitor plates is given by $C_s V_\circ$ where C_s is the sample capacitance. Equation (3.3) represents small signal conditions.

Induced current through the sampling resistor can be explained using the Shockley-Ramo theorem which describes the instantaneous induced current at an electrode. In reference to Figure (3.1), the theorem states that the induced current is caused by the instantaneous change in the electrostatic flux lines (F_2 lines) at the electrode B. In the TOF technique, this implies that a moving charge sheet relatively far away from the electrode B produces an instantaneous change in electrostatic flux at the electrode B. The change in F_1 causes a

change in the negative charge density of B, which is provided by an external current. The total quantity of charge carriers travelling in both the sample and through the resistor must be the same. The induced current is given by the Shockley-Ramo theorem as

$$i_{ph} = Q_o v_d / L, \tag{3.4}$$

where Q_o is total charge in the charge sheet, v_d is the drift velocity, and L is the sample thickness.

Total injected charge Q_o can be expressed as the multiplication of the electron charge e, injected carrier concentration p_o, and the charge sheet volume given by width w and area A. By taking into account the geometry of the charge sheet, the photocurrent is given by

$$i_{ph}(t) = \begin{cases} \dfrac{ep_o wAv_d}{L} = \dfrac{ep_o wA}{t_T} & 0 < t < t_T \\ 0 & t > t_T \end{cases}, \tag{3.5}$$

where t_T is the transit time, which is defined as the duration of time for the charge sheet to travel across the sample.

In small signal AC analysis, the sample acts as a resistor R and a capacitor C_s connected in parallel to a current source outputting i_{ph}. If $V(s)$ is the Laplace transform of the voltage across the parallel resistor and capacitor, and $i_{ph}(s)$ is the Laplace transform of the photocurrent, the following relationship can be shown to hold

$$V(s) = \frac{R}{sRC_s + 1} i_{ph}(s). \tag{3.6}$$

The transient voltage response $v(t)$ can be found by taking the inverse Laplace transform. Two solutions to the transient response exist when the bandwidth arbitrarily set to the inverse of the transit time. The solutions, which depend on the magnitude of R and C_s are for the cases of RC_s being either much greater than (3.8) or much smaller than (3.7) the transit time t_T.

The transient voltage in equation (3.7) is directly proportional to the photocurrent and

is referred to as the I-mode signal

$$V(t) \approx \begin{cases} Ri_{ph}(t) & 0 < t < t_T \\ 0 & t > t_T \end{cases} \text{ for } RC_s \ll t_T. \tag{3.7}$$

Equation (3.8) is for the case $RC_s \gg t_T$ and can be expressed as the V-mode or *charge transient signal* as done in equation (3.9). The V-mode signal increases linearly as the charge sheet travels across the sample and can be used to measure the total injected charge when $t \geq t_T$

$$V(t) \approx \begin{cases} \dfrac{1}{C_s}\dfrac{ep_owA}{t_T}t & 0 < t < t_T \\ 0 & t > t_T \end{cases} \text{ for } RC_s \gg t_T \tag{3.8}$$

$$V(t) \approx \frac{1}{C_s}\int_0^t i_{ph}(t')dt'. \tag{3.9}$$

The above equations are valid for a material which does not contain charge carrier traps. Amorphous materials however are disordered with a large number of charge carrier traps in localised states. As the carriers traverse the sample, the traps act to remove carriers from the transport band for the duration of the experiment causing the measured photocurrent to decay exponentially. The traps can be characterised by a mean trapping time τ_c. The photocurrent resulting from injected charge in equation (3.5) can be modified to account for exponential decay as follows

$$i_{ph}(t) = \frac{ep_owA}{t_T}\exp(-t/\tau_c). \tag{3.10}$$

Therefore, the expression for the I-mode signal becomes

$$V(t) = \begin{cases} R\dfrac{ep_owA}{t_T}\exp(-t/\tau_c) & 0 < t < t_T \\ 0 & t > t_T. \end{cases} . \tag{3.11}$$

The expression for the V-mode signal is determined from the integration of equation (3.11) and is given by

$$V(t) = \begin{cases} \dfrac{ep_owA\tau_c}{C_st_T}\left(1 - \exp\left(-\dfrac{t}{\tau_c}\right)\right) & 0 < t < t_T \\ \dfrac{ep_owA\tau_c}{C_st_T}\left(1 - \exp\left(-\dfrac{t_T}{\tau_c}\right)\right) & t > t_T \end{cases} . \tag{3.12}$$

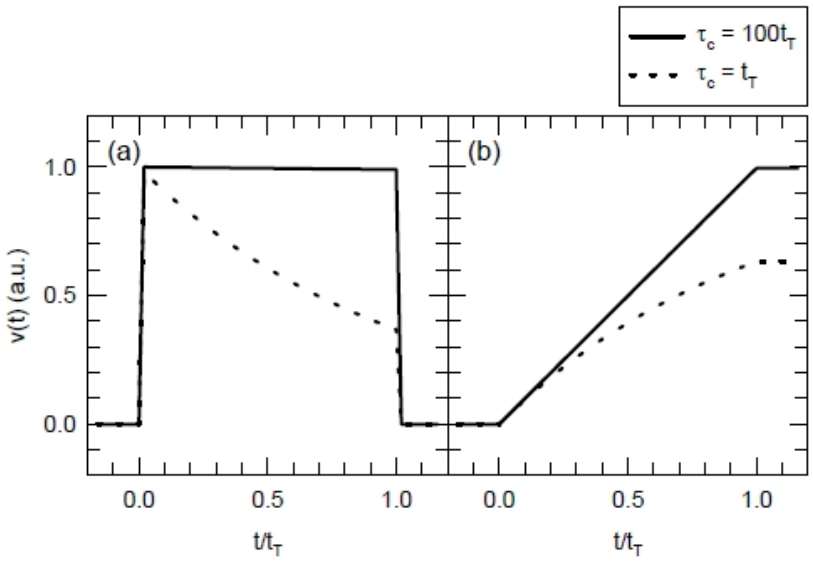

Figure 3.2: Simulated TOF (a) I-mode and (b) V-mode photocurrent signals with no traps (solid) and deep trapping (dashed). After Fogal [1].

Figure 3.2 illustrated the expected TOF waveforms for the case of a trap free solid and for deep trapping in which τ is comparable to the transit time.

3.3 The Interrupted-Field Time-of-Flight Technique

The interrupted-field time-of-flight (IFTOF) experiment is a method used to determine the deep trapping lifetime of high resistivity materials. The IFTOF experiment is performed exactly the same way as the conventional TOF experiment except that the charge sheet is halted for an arbitrary period of time t_i midway in its drift across the sample as shown in Figure 3.4 (b). The charge sheet is interrupted by removing the applied electric field. While halted in the middle of the sample, the charge carriers in the charge sheet interact with deep traps resulting in a reduction in charge carrier concentration in the transport band. The field is reapplied after an arbitrary interruption time and remains applied until the charge sheet exits the sample. The deep trapping lifetime is given in equation (3.13). This expression can be obtained from equation (3.11). The calculation involves the interruption time t_i as well as the ratio of the magnitudes of the photocurrent, which is directly proportional to the carrier concentration, immediately before and after interruption. The fraction $i(t_2)/i(t_1)$ is

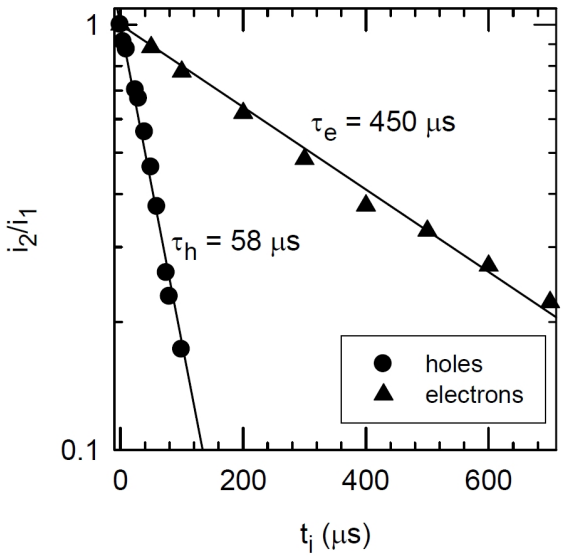

Figure 3.3: A plot of the fractional recovered signal i_2/i_1 versus interruption time for holes and electrons in a 224 μm thick a-Se:0.2% As specimen. After Fogal [1].

referred to as the fractional recovered signal and is given by

$$\frac{i(t_2)}{i(t_1)} = \exp\left(-\frac{t_i}{\tau_c}\right), \tag{3.13}$$

where i is the photocurrent, t_1 is the start of the interruption period, t_2 is the end of the interruption period, t_i is the duration of the interruption period, and τ_c is the deep trapping lifetime.

A typical IFTOF experiment measures the fractional recovered photocurrent as a function of interruption time. In a typical experiment, the deep trapping lifetime is determined from the inverse of the regression line slope of a semi-logarithmic plot of fractional recovered signal versus interruption time. A plot of fractional recovered signal versus interruption time is seen in Figure 3.3.

3.4 Trap-Controlled Transport of Photoinjected Carriers

The previous section introduced the principles of the TOF and IFTOF experiment. Expressions for the I-mode and V-mode signals were also developed. The previous section did not account for the possibility of a distribution of localised states occuring in the bandgap

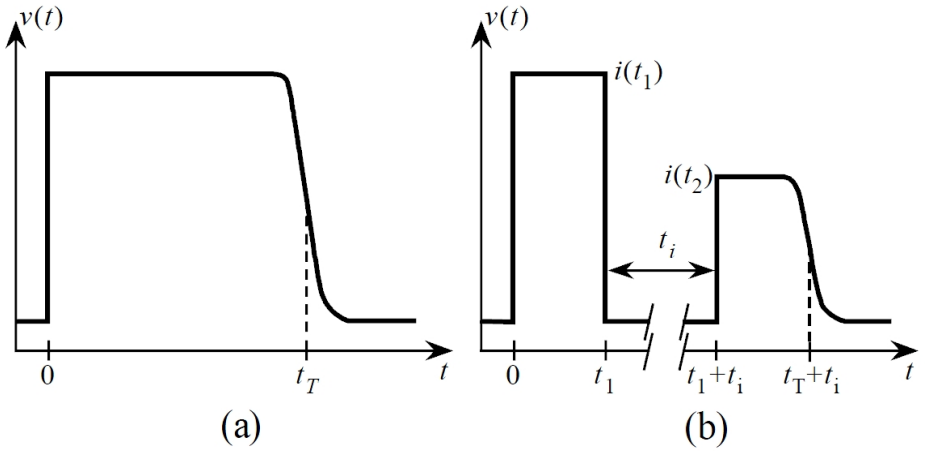

Figure 3.4: (a) Typical TOF waveform. (b) Typical IFTOF waveform. Reduction in carriers from t_1 to t_2 is a result of deep trapping. After Fogal [1].

of the amorphous semiconductor. These states affect carrier kinetics as they act as capture centres (traps) for carriers in the transport band. A transient trap limited theory is developed in this section to explain the transient response that is observed in high resistivity semiconductors for two cases: a discrete monoenergetic trap distribution, and a discrete binary trap distribution.

3.4.1 Monoenergetic Trap Level

Consider first a simple model of a high resistivity semiconductor material with a single well-defined energy state between the conduction and valence band. This state acts to trap and release electrons from the conduction band or holes from the valence band. The following section uses holes as charge carriers as current is defined in terms of positive charge flow in the semiconductor; however holes and electrons in the following expressions are interchangeable.

A rate expression for carriers in a slice dx in time interval dt is shown in the continuity equation (3.14) below. The first term on the right describes the change in the current density flowing through the slice dx. The second term describes the rate of release of trapped carriers

$$\frac{\partial p(x,t)}{\partial t} = -\frac{1}{e}\frac{\partial J(x,t)}{\partial x} - \frac{\partial p_t(x,t)}{\partial t}, \tag{3.14}$$

where p is the concentration of holes, p_t is the concentration of trapped holes, and J is the conduction current density.

The conduction current is made up of charge carriers drifting as a result of the applied electric field and also by charge carriers undergoing diffusion. It is expressed in equation (3.15)

$$J(x,t) = e\mu F p(x,t) - eD\frac{\partial p(x,t)}{\partial x}, \tag{3.15}$$

where D is the diffusion coefficient, μ is the drift mobility, and $F(x,t)$ is the electric field.

Combining equations (3.14) and (3.15) produces the following one dimensional continuity equation for holes

$$\frac{\partial p(x,t)}{\partial t} = -\mu F(x,t)\frac{\partial p(x,t)}{\partial x} - \mu p(x,t)\frac{\partial F(x,t)}{\partial x} + D\frac{\partial^2 p(x,t)}{\partial x^2} - \frac{\partial p_t(x,t)}{\partial t}. \tag{3.16}$$

The one dimensional continuity equation for electrons is written as

$$\frac{\partial n(x,t)}{\partial t} = \mu F(x,t)\frac{\partial n(x,t)}{\partial x} + \mu n(x,t)\frac{\partial F(x,t)}{\partial x} + D\frac{\partial^2 n(x,t)}{\partial x^2} - \frac{\partial n_t(x,t)}{\partial t}. \tag{3.17}$$

Given the capture and release times for the charge carriers, an expression for the rate equation for holes can be written by taking the difference between trapping and release rates

$$\frac{\partial p_t(x,t)}{\partial t} = \frac{p(x,t)}{\tau_c} - \frac{p_t(x,t)}{\tau_r}, \tag{3.18}$$

where τ_c is the average time for a carrier to be trapped, and τ_r is the average time for a trapped carrier to be released.

Simplifying assumptions can be made in order to obtain a closed form solution to equation (3.16). A uniform electric field can be assumed resulting in the term $\partial F(x,t)/\partial x$ being neglected. This assumption results from the fact that the injected charge is much smaller than the charge on the electrodes which allows for any coulombic interactions between injected charge and charge on electrodes to be neglected. This means that applied field is uniform and due to the charges on the electrodes. The diffusion term can also be neglected since the diffusion current is much smaller than the conduction current.

In order to solve equations (3.16) and (3.18) simultaneously, initial conditions must be defined. The charge injected at time and position zero is given by

$$p(x,0) = N_o \delta(x,0), \tag{3.19}$$

where N_o is the injected charge concentration. At time zero, the charge trapping has not occured and as a consequence the trapped carrier concentration is given by

$$p_t(x,0) = 0 \quad \text{for} \quad x > 0 \ . \tag{3.20}$$

Outside of the sample carriers do not exist and therefore the following boundary conditions hold

$$p(x,t) = 0 \quad \text{for} \quad x > L \tag{3.21}$$

$$p_t(x,t) = 0 \quad \text{for} \quad x > L \ , \tag{3.22}$$

where L is the finite sample length.

Simultaneously solving equations (3.16) and (3.18) and applying initial conditions, produces equaiton (3.23) [65].

$$p(x,t) = \frac{P_o}{\mu_o F} \exp\left[-\frac{z}{\tau_c}\right] \delta(t-z) + \frac{P_o}{\mu_o F} \exp\left[-\frac{z}{\tau_c} - \frac{(t-z)}{\tau_r}\right] \frac{\xi}{2} \frac{I_1(\xi)}{(t-z)} U(t-z), \tag{3.23}$$

where $z = x/\mu_o F$, $I_1(\xi)$ is the first order hyperbolic Bessel function, $U(x)$ is the unit step function, and $\xi = 2\sqrt{\tau_c z(t-z)/\tau_r}/\tau_c$. The first term represents charge carriers that have not undergone trapping. The term sees a time dependent exponential decay of $\exp(-t/\tau_c)$ from the time the charge is injected into the sample. The second term represents charges in the conduction band which have undergone at least one trapping event. These charges have a minimum transit time of $t_T = L/\mu_o F$. Integrating equation (3.23) over the sample length gives a time dependent expression for the external current. Under TOF experimental conditions, of low and high fields, assumptions can be made that allow for equation (3.23) to be simplified.

Long Transit Time or Shallow Trap Controlled Drift

A low applied field results in a long transit time. Under low field, the capture time τ_c can be assumed to be considerably shorter than the fastest carrier transit time, given by $t_T = L/\mu_o F$. The release time is comparable with the transit time, giving $\tau_c \ll \tau_r$. The implication is that once trapped, an average charge carrier will not be released for the duration of the TOF experiment. Spreading of the charge carrier packet during transit due to trapping events is neglected in this case since the release time is taken to be much larger than capture time. Shallow trap controlled drift is depicted in Figure 3.5. These restrictions imposed on equations (3.16) and (3.18) cause the time derivative of the total charge in the conduction band to vanish over a long time interval. When in equilibrium and when charge conservation is considered, the free charge in the sample can be shown to be

$$P = P_o \frac{\tau_c}{\tau_c + \tau_r}. \tag{3.24}$$

The injected number of charges is given by

$$P_o = p_o A w, \tag{3.25}$$

where p_o is carrier concentration, A is charge sheet area, and w is charge sheet width.

The hole photocurrent is obtained by substituting equation (3.24) into equation (3.5)

$$i_{ph} = \frac{eP_o\mu_o F}{L}\frac{\tau_c}{\tau_c + \tau_r} = \frac{eP_o\mu F}{L}. \tag{3.26}$$

Inspecting Equation (3.26) reveals that the trap-free photocurrent with mobility μ_o is reduced to μ

$$\mu = \frac{\tau_c}{\tau_c + \tau_r}\mu_o = \theta\mu_o. \tag{3.27}$$

The effective carrier drift mobility is reduced because of trapping and release events. This transport mechanism is referred to as *shallow trap-controlled transport*, and the scalar θ is referred to as the *shallow trap-controlled transport factor*.

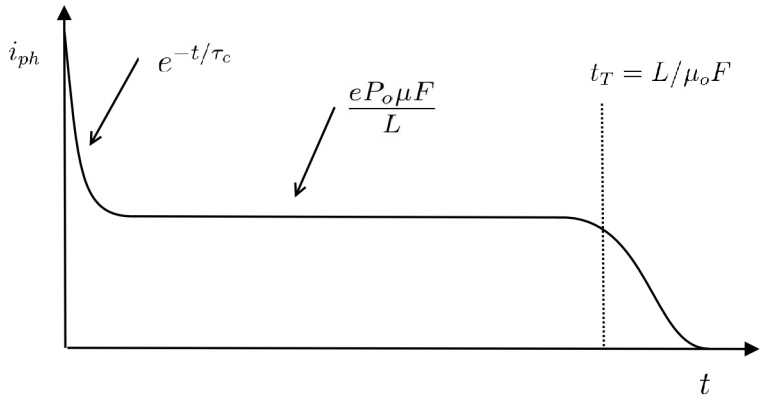

Figure 3.5: TOF waveform depicting shallow trap controlled drift. Deep trapping is ignored resulting in a constant steady state current.

Short Transit Time and Weak Trapping

In the high field case, the carrier transit time is taken to be much smaller than the capture time $t_T \ll \tau_c$. Expressions for the TOF transient signal were developed for two different time ranges [66]. These ranges are $0 < t < t_T$ and $t > t_T$. For the $0 < t < t_T$ time range the transient signal is given by

$$i_{ph}(t) = \frac{eP_o}{t_T}\left[\frac{\tau_c}{\tau_c+\tau_r} + \frac{\tau_r}{\tau_c+\tau_r}\exp\left(-\frac{\tau_c+\tau_r}{\tau_c\tau_r}t\right)\right] \quad \text{for } 0 < t < t_T \ . \tag{3.28}$$

If detrapping is neglected by taking $\tau_r \to \infty$, equation (3.28) reduces to equation (3.10), where only trapping was considered. For the $t > t_T$ time range the transient signal is given by

$$i_{ph}(t) = \frac{eP_o}{2}\frac{t_T}{\tau_c\tau_r}\exp\left(-\frac{t}{\tau_r}\right) \quad \text{for } t > t_T \ . \tag{3.29}$$

Equation (3.29) refers to carriers that have undergone at least one trapping event. In the high field case, most trapped carriers undergo a single trapping event as they have already traversed a portion of the sample before being trapped and are unlikely to be trapped a second time. The two equations together describe two separate photocurrent exponential decay curves. The first occuring from $0 < t < t_T$ to carriers undergoing a trapping event and the second occuring from $t > t_T$ which is a result of release events. This response is shown in Figure 3.6.

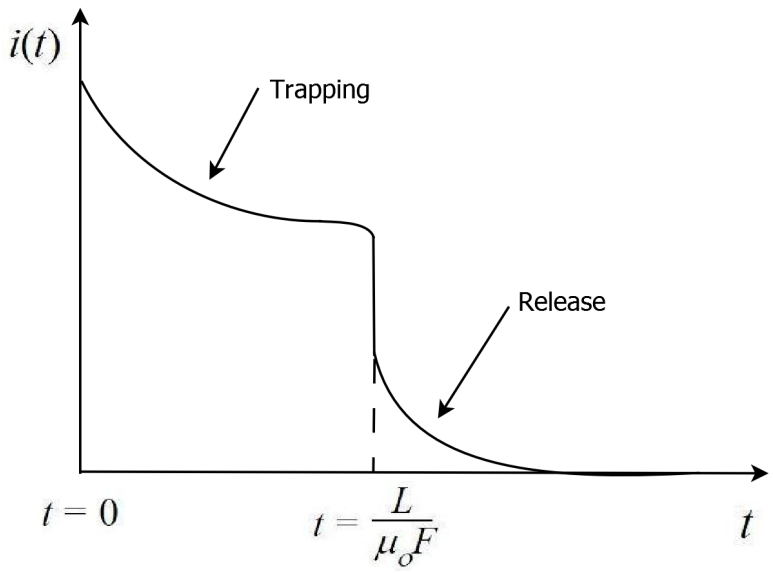

Figure 3.6: Photocurrent waveform in the high fields model. After Allen [2].

3.4.2 Binary Trap Distribution

The argument used in the monoenergetic trap distribution section is extended to two trap levels. As a consequence, two capture times τ_{c1} and τ_{c2} and two release times τ_{r1} and τ_{r2} must be considered. Residual trap-filling, from repeated measurements, can be neglected since the concentration of injected charge is considerably less than the concentration of traps at each level. The following equations hold for trapping of carriers in the conduction band. The trapping rate equation given in equation (3.18) is modified as follows

$$\frac{\partial p_{t1}(x,t)}{\partial t} = \frac{p(x,t)}{\tau_{c1}} - \frac{p_{t1}(x,t)}{\tau_{r1}} \tag{3.30}$$

and

$$\frac{\partial p_{t2}(x,t)}{\partial t} = \frac{p(x,t)}{\tau_{c2}} - \frac{p_{t2}(x,t)}{\tau_{r2}}. \tag{3.31}$$

When the total concentration of trapped charge is expressed as $p_t(x,t) = p_{t1}(x,t) + p_{t2}(x,t)$, equations (3.30),(3.31) and the continuity equation (3.14) can be simultaneously solved as shown in Blankey and Grunwald [67] for the time evolution of the charge carrier packet given by

$$j(t) = A\exp(-\alpha t) + B\exp(-\beta t) + j_\infty, \tag{3.32}$$

where

$$\alpha + \beta = \frac{1+\theta_1}{\tau_{c1}} + \frac{1+\theta_2}{\tau_{c2}} \tag{3.33}$$

$$\alpha\beta = \frac{[\theta_1 + \theta_2(1+\theta_1)]}{\tau_{c1}\tau_{c2}} \tag{3.34}$$

$$\alpha A + \beta B = \frac{j_o}{\tau_{c1}} + \frac{j_o}{\tau_{c2}} \tag{3.35}$$

$$A + B + j_\infty = j_o \tag{3.36}$$

and

$$j_\infty = \frac{j_o\theta_1\theta_2}{[\theta_1 + \theta_2(1+\theta_1)]}, \tag{3.37}$$

where $\theta_1 = \tau_{c1}/\tau_{r1}$ and $\theta_2 = \tau_{c2}/\tau_{r2}$. The term j_∞ represents the steady state current that flows after the injected charge has reached equilibrium with the traps.

When one of the two trap levels is located deep in the bandgap such that the thermal release time $\tau_{r2} \to \infty$, the result is a case where the term $\theta_2 = 0$. Equation (3.32) reduces to

$$j(t) = A\exp\left(-\frac{t}{\tau_{c1}}\right) + B\exp\left(-\frac{\theta_1 t}{\tau_{c2}}\right). \tag{3.38}$$

Equation (3.38) describes current which is *shallow trap controlled with deep trapping*. The first term produces an initial sharp decay as the injected charge equilibrates with shallow traps. The second term describes a shallower decay with characteristic decay rate. This case is depicted in Figure 3.7.

3.5 Summary

In this chapter, the principles of the TOF and IFTOF techniques were introduced. The TOF technique is used in determining the carrier mobility, while the IFTOF technique is used to determine the carrier lifetime. These techniques are useful in the characterization of the electrical properties of semiconductors.

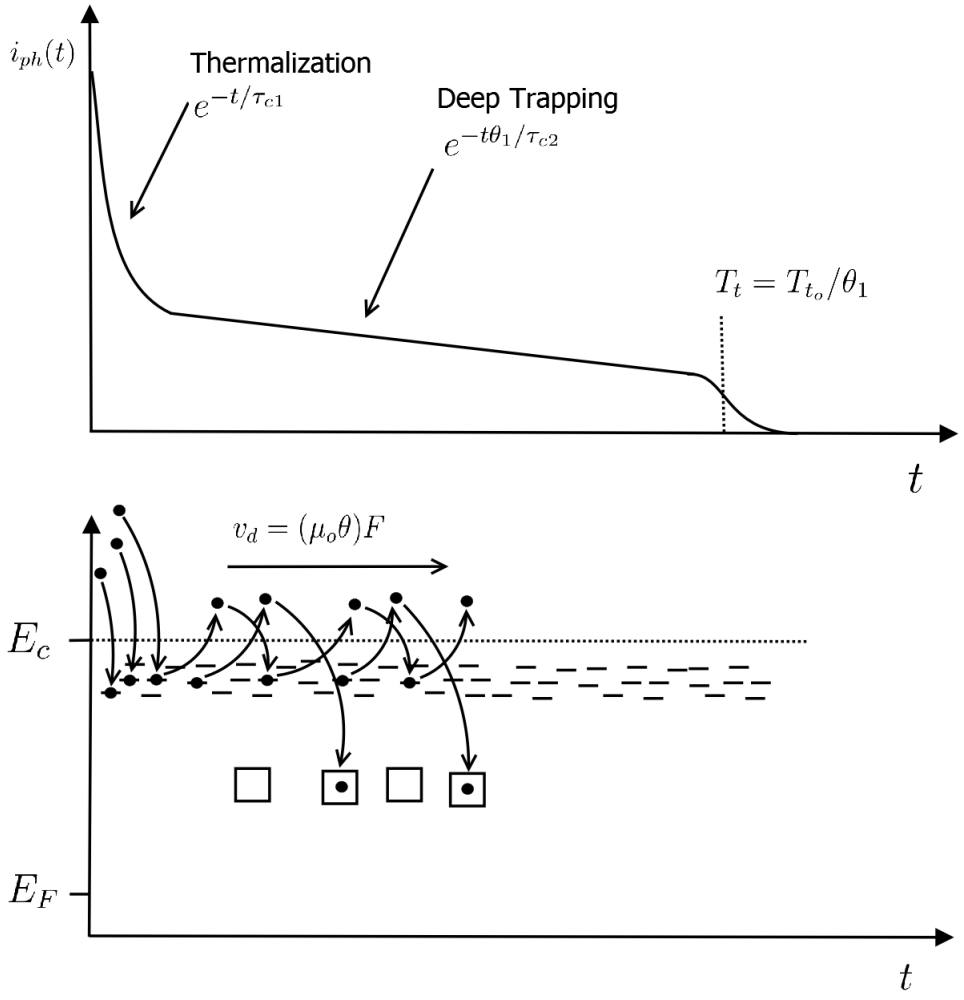

Figure 3.7: Schematic simultaneously depicting both the photocurrent and energy band diagram representation of the TOF experiment with a binary trap distribution. The processes of thermalization and deep trapping are shown with an expression for exponential decay in each. The drift of the charge carrier packet is given by v_d. Shallow trapping occurs in states just below the conduction band (E_c). Deep trapping occurs in lower energy states than shallow trapping but above the fermi level (E_F). Shallow trap states are denoted by long dashed lines. Deep trap states are denoted by squares.

Two cases of trap distributions were examined showing the dependence of transient response (the photocurrent) on the trap distribution. Shallow traps were shown to result in a lower mobility as carriers are trapped and released repeatedly as they travel across the sample. Deep traps result in a decay in photocurrent in accordance with a characteristic trapping time τ_c. Inversely, the transient response can be analysed to probe the distribution of trap states. The TOF and IFTOF techniques are therefore important tools for studying the fundamental charge transport processes of high resistivity semiconductors.

4. Experimental Procedure

4.1 Introduction

The experimental procedure used to measure the electrical properties of amorphous selenium is covered in this chapter. The procedure for the preparation of amorphous selenium is outlined as is the IFTOF system, temperature control system, and the x-ray system. The procedure for determining the lifetime from the IFTOF experiment is also outlined.

4.2 Sample Preperation

This section covers the sample preperation procedure. There are several procedures which must be followed in order to prepare the sample. These procedures include the preparation of the substrate, the deposition of the amorphous semiconductor and the deposition of an electrical contact.

Conventional vacuum evaporation of vitreous selenium pellets was employed. The selenium was evaporated onto an aluminium substrate. The substrate was ultrasonically cleaned in a sequence of acetone, methanol and distilled water baths in order to remove any impurities. The Aluminium layer with oxide coating acts as a bottom electrode. An oxide coating is grown on the aluminium surface by heating the substrate to 300 °C for approximately 5 hours. The oxide coating blocks charge injection from the bottom electrode and acts as an amorphous surface.

A schematic diagram of the NRC 3117 vacuum deposition system is shown in Figure 4.1. In the figure T/C denotes a temperature controlled surface. The NRC3117 stainless steel vacuum coater system is used in vacuum deposition. Inside a vacuum sealed chamber which

is evacuated to a base pressure of approx 10^6 Torr, a substrate is placed above a molybdenum boat. Selenium pellets are placed in the boat and are heated to approximately 250°C by a large $100 - 150$ A AC current to the point of evaporation [68]. Vapour rises and condenses on the substrate to form a layer of a-Se. Approximately $40 - 50$ g of source material is required per sample of 100 μm of film thickness. A mechanical shutter is used until a steady deposition rate of 2 μm/min is achieved. The evaporation rate is digitally monitored using a detector using a quartz crystal. A thermocouple is placed in the boat and on the substrate. Under automated temperature control, the substrate was kept at 55°C which is above the glass transition temperature of selenium which is approximately 40°C [68]. The range of electron charge carriers is not as dependant on the substrate temperature during deposition as is the hole range. The hole range is shown to improve if the substrate temperature is kept above the glass transition temperature [69]. The electron range is most sensitive to impurities [65]. a-Se samples alloyed with arsenic and doped with Cl were pre-alloyed and pre-doped by the supplier of the a-Se pellets (Analogic Corporation). Samples were composed of $0.2 - 0.5\%$ arsenic, 100ppm $CaCl_2$, and $0 - 2$ ppm chlorine. Arsenic is used to retard crystallization while chlorine is added to reduce the hole deep trap concentration. a-Se alloyed with arsenic within the range of $0.2 - 1\%$ is considered thermally stabilized a-Se. All source material was provided by Analogic Corporation of Montreal with stated composition nominal to approximately 30%. After deposition the substrate and boat heater are turned off to cool and eventually the sample is removed in order to deposit electrodes.

The deposited thickness of the thesis samples ranged from $74 - 155$ μm. The thickness was measured using a digital micrometer by taking several readings and averaging. The absolute error in thickness is ± 2 μm.

A circular semi-transparent gold contact of area 0.2 cm^2 acts as a top electrode. The gold contact is prepared using the Hummer 6 sputtering system. The system is flushed several times with argon gas with pressure being pumped down to 50 mTorr. A high voltage ($3000 - 4000$ V) is then applied to create a plasma and ionize the gas. Positively charged argon ions collide with the gold target placed in front of the anode. Dislocated gold atoms impinge on the a-Se surface creating a uniform coating on a portion of the sample which is

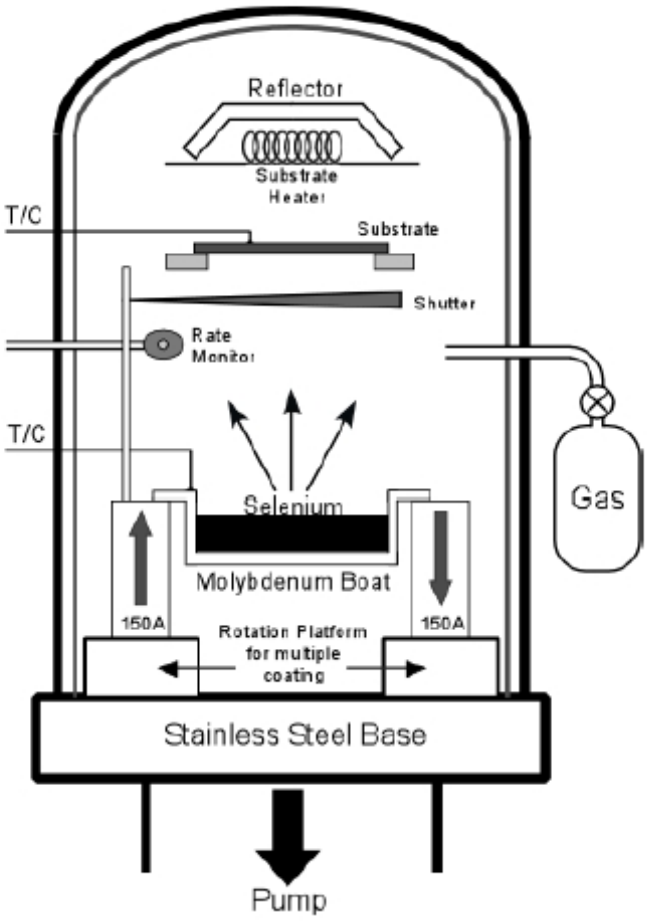

Figure 4.1: A schematic diagram of the NRC 3117 vacuum deposition system used to make the a-Se samples in this study. After Allen [2].

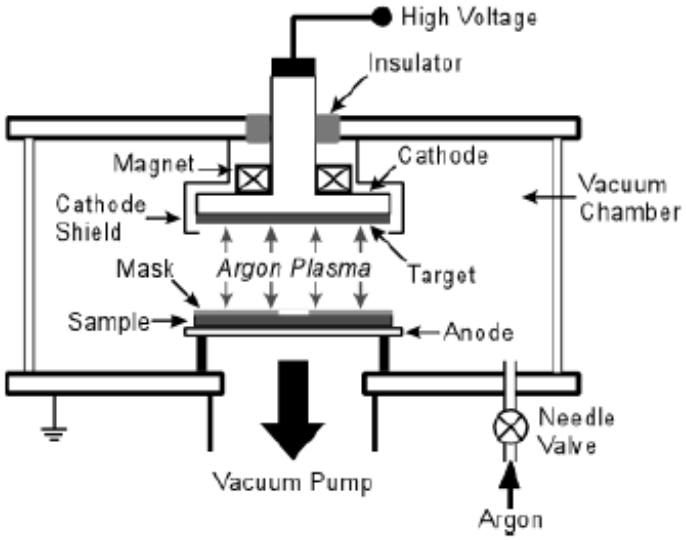

Figure 4.2: A schematic diagram of the Hummer VI sputtering system used to make gold contacts on the a-Se sample. After Allen [2].

exposed by a mask. A schematic diagram of the Hummer VI sputtering system is shown in Figure 4.2.

4.3 Connection of TOF Apparatus

The TOF apparatus is connected to the gold contact by a stainless steel needle. Placed between the needle and the Au contact is a piece of indium in order to avoid the pin piercing through the thin Au coating. Photoexcitation is kept inside the Au electrode by the use of a light blocking non-conducting mask.

A side view image of a sample loaded in a sample holder is shown in Figure 4.3. The fibre optic cable is held in position by a holder consisting of two thin transparent plastic sheets pierced by a hole the size of the fibre. The holder was made by securing the two plastic sheets on either side of the aperture of the stainless steel chamber lid. In orientating the plastic sheets, one hole was placed over the other. The fibre optic cable was threaded through the holes. Not shown in the cross-sectional view is the one inch diameter aperture of the lid above and below of which the plastic sheets are secured. The fibre optic cable and plastic sheets provide negligeable x-ray absorption due to their relatively low mass absorption

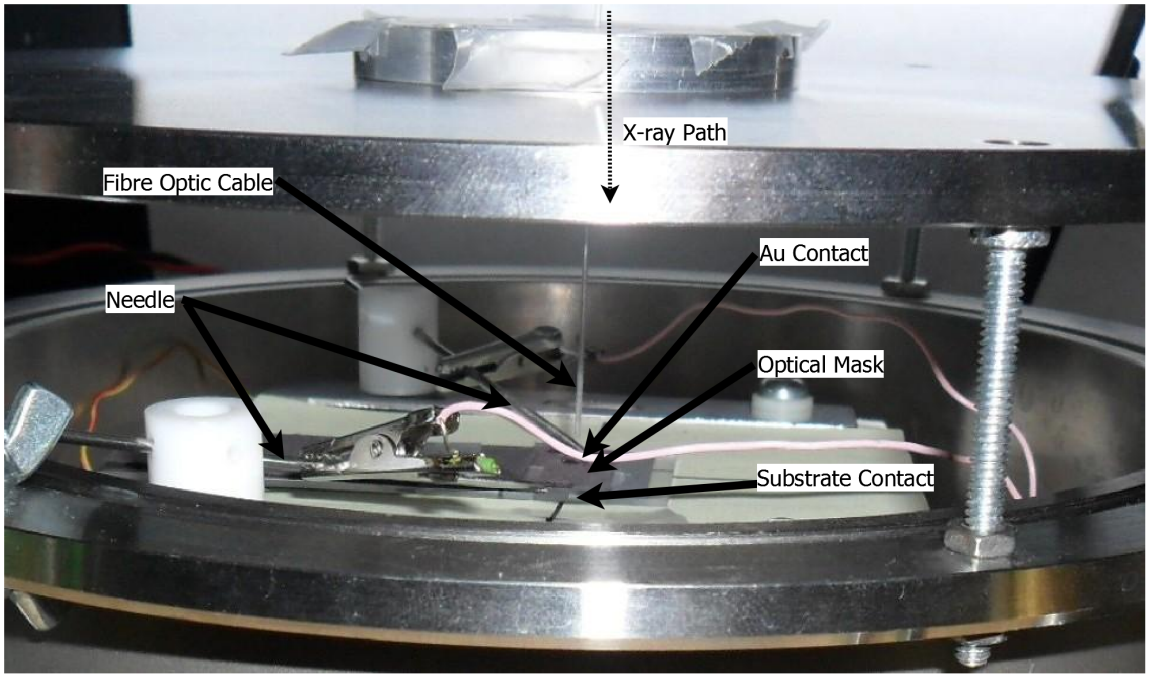

Figure 4.3: A sample loaded in the sample holder. At experiments performed at a sample temperature of 10 °C, the lid was sealed with the air in the chamber evacuated and replaced with nitrogen in order to prevent condensation from forming on the top electrode.

coefficients and thin material thickness. This experimental setup allows for the measurements to be automated as human intervention was not required in transitioning between sample irradiation and IFTOF measurement.

An image of a sample loaded in a sample holder without a cover or a fibre optic cable is shown in Figure 4.4. The gold contact was deposited near the centre of the sample. Surrounding the gold contact is a black optical mask. Touching the gold contact is a stainless steel needle acting as an electrode. Touching the aluminum substrate is another stainless steel needle acting as an electrode. To the left of the sample is a glass slide with a thermocouple attached with an adhesive. The surface on which the sample is placed can be temperature controlled. The chamber can be filled with nitrogen gas via the tube entering through the bottom right of the image (with a round black valve handle). Gas exits the chamber via the tube on the bottom left of the picture (with a green valve handle).

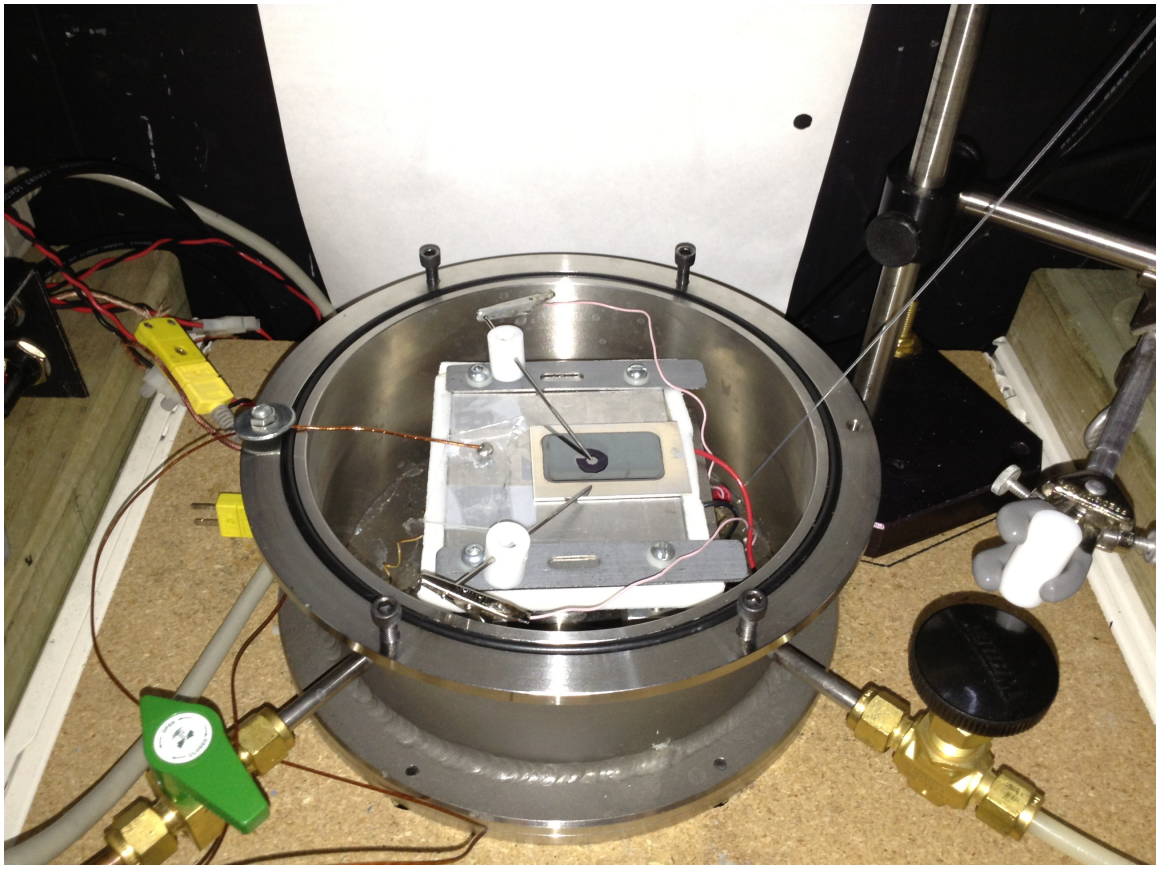

Figure 4.4: A sample loaded in the sample holder. Experiments performed at 10 °C had a closed lid with the chamber filled with nitrogen gas. Experiments performed at 21 °C and 35 °C used the chamber lid which was hovered over the sample by using bolts as height extensions. The fibre optics cable was held in place by the lid which allowed for the fibre optics cable to be centred above the gold electrode. The fibre optics cable was held in place in the middle of an aperture which allowed for x-ray irradiation of the sample.

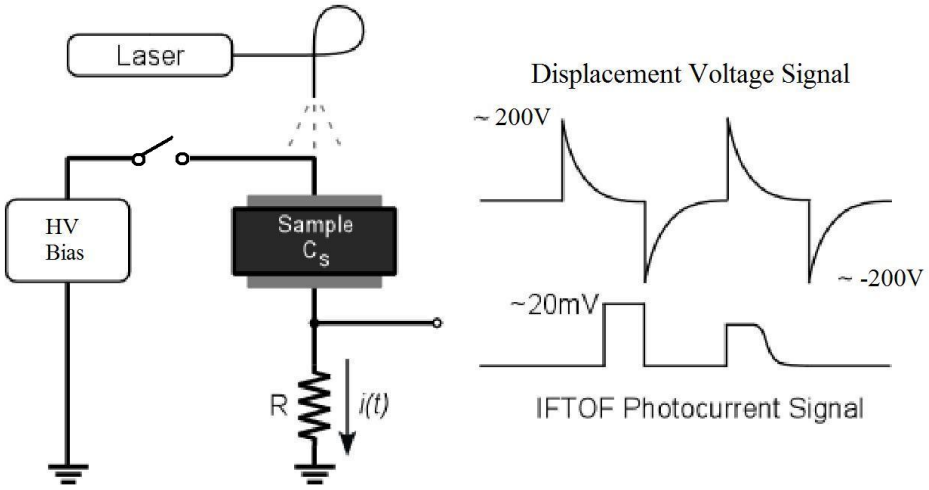

Figure 4.5: A displacement voltage is produced when a HV bias is applied or removed. After Allen [2].

4.4 Charge Transport Measurements

A displacement voltage schematic is shown in Figure 4.5. The displacement voltage results from the near instantaneous change in HV bias. The large amplitude voltage seen across the sampling resistor is a superposition of the photocurrent induced drop in voltage and the voltage drop induced by the HV transient.

Charge transport properties were measured in the experiments. The two techniques employed to measure charge transport were conventional Time-of-Flight (TOF) and Interrupted-Field Time-of-Flight (IFTOF). These techniques involve the measurement of photocurrent. The theory section details the process by which photocurrent is created and by which charge carriers drift across the sample under applied field.

The principle components of an TOF/IFTOF measurement system are shown in the schematic of Figure 4.6. The process by which a measurement is taken involves the sequential triggering of a bias V_A, a short light pulse, an oscilloscope, and an amplifier. Charge is injected into the sample by photoexcitation. Photoexcitation occurs when a short light pulse is absorbed by the sample. In the process electron-hole pairs are created. Photoexitation occurs near the surface of the sample directly below the gold semi-transparent electrode. The gold electrode acts as a neutral density filter to incident ultraviolet light. An electric field is

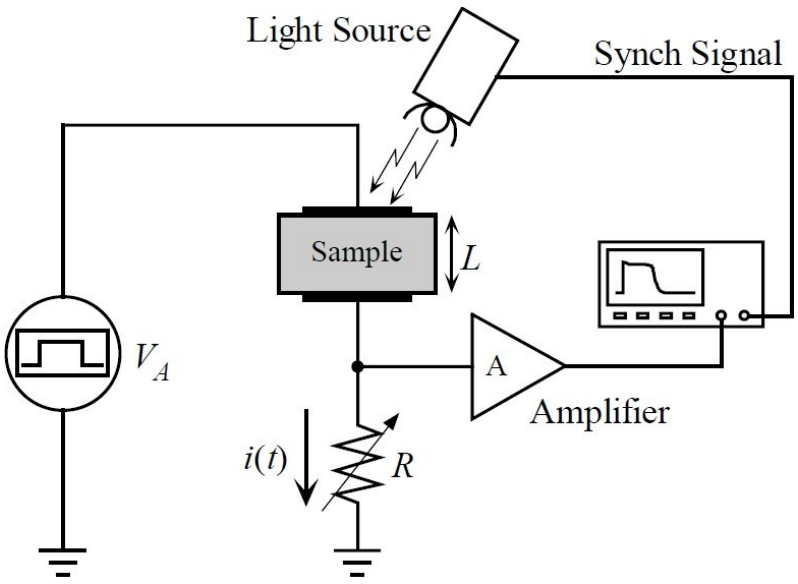

Figure 4.6: TOF and IFTOF measurement system schematic. A bias was applied across the sample via V_A. The operation of the light source, oscilloscope, and amplifier were synchronized. After Allen [2].

applied across two electrodes acting as parallel plate capacitors. Charge carriers of opposite charge to the top electrode are attracted while oppositely charged carriers drift through the sample towards the bottom electrode located on the substrate surface. As the carriers drift across the sample, a photocurrent is induced resulting in a voltage across the sampling resistor $v(t) = Ri(t)$. The induced photocurrent passes through the sampling resistor. A voltage amplifier is connected to the sampling resistor which produces a signal large enough to be read by an oscilloscope.

The process by which the photocurrent is captured first involves the application of an applied bias across the sample. Photoexcitation follows the application of bias. A photocurrent is produced from the drift of charge carriers across the sample. The induced charge across a sampling resistor is captured by an oscilloscope.

The sample behaves like a capacitor producing a photocurrent with an RC rounding effect. Limitations are placed on the applied bias V_A since a short carrier transit time (t_T) results in a reduction in the ability to accurately measure the waveform. Under ideal conditions $RC \ll t_T$.

There are several techniques for removing the displacement voltage. The first technique listed here is the complimentary bias switching technique [70]. This technique can eliminate a maximum displacement voltage of 200 V. This technique has the disadvantage of being impractical for large voltages. This is because there is a difference in transient outputs of the switches. The second technique is the resistance ratio bridge network technique [71]. The arrangement in this technique involved a floating bridge, and a floating voltage power supply. This technique has the disadvantage of applying only half of the output bias to the sample. The third technique is the floating Schering bridge technique [72]. This technique can eliminate a maximum displacement voltage of 1 kV. The disadvantage of this technique is that the bridge is difficult to balance. This is because of the introduction of stray capacitances.

The displacement voltage was removed using a grounded bridge network. Figure 4.7 provides an illustration of a grounded bridge network. The grounded bridge network has the advantage of using a grounded voltage supply. The voltage across the two bridge resistors is identical if a condition is met. The condition is that the sample capacitance C_S matches the variable capacitor C_N. If this condition is met, the differential voltage between both branches is zero. The amplifier outputs the photocurrent signal since it is the only thing that is different between both branches of the bridge network.

In practice the differential measurement scheme has stringent requirements. The two requirements are: a very large CMRR ($\sim$ 100 dB), and the ability to withstand a very large common mode input signal without saturation. CMRR must occur over a wide bandwidth. The two requirements are met by the use of back-to-back rectifiers. The back-to-back rectifiers limit the magnitude of the displacement voltage signal to a nominal value of $\sim$ 0.7 V. The forward voltage drop across a diode is 0.7 V. The requirement on the amplifier can be reduced with the use of back-to-back diodes. This is because of a small remaining common mode signal. In this case, an amplifier with CMRR of $\sim$ 60 dB can be used.

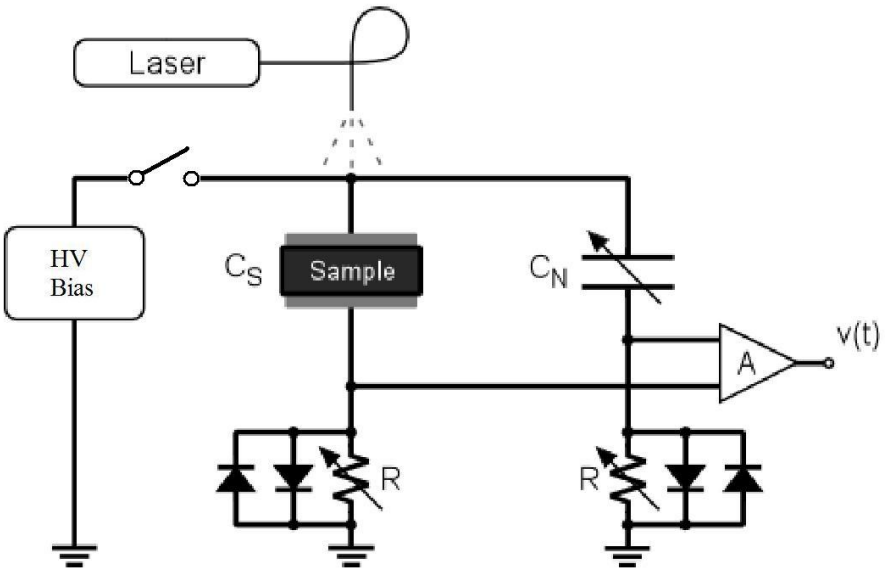

Figure 4.7: A grounded bridge network added to Figure 4.5 in order to eliminate the large displacement voltage caused by switching the high voltage in the IFTOF technique. After Allen [2].

4.4.1 Mobility Measurement with TOF

The TOF technique was first introduced by Spear, Kepler, LeBlanc, and Brown [2]. Variations in photoexcitation source and high voltage bias have been developed by researchers using the TOF technique [2]. Photoexcitation sources in use include Xenon flash, nitrogen laser and pulsed electron gun.

Typical TOF and IFTOF waveforms are shown in figure 4.8. The beginning of the waveform marks photoexcitation. The knee marks the first carriers exiting the sample. Half the charge carriers have exited the sample at the point in time where the TOF waveform reaches the half amplitude of steady state photocurrent. The transit time can be defined either at the knee, at half the steady state current, or at the apex of the TOF tail.

The rate at which charge carriers in the charge packet exit the sample can be determined. This is done by differentiating the transient voltage of the TOF waveform with respect to time. With further calculation and on exiting the sample, the cross sectional spatial distribution, or full-width at half-maximum (FWHM), of the charge packet can be determined.

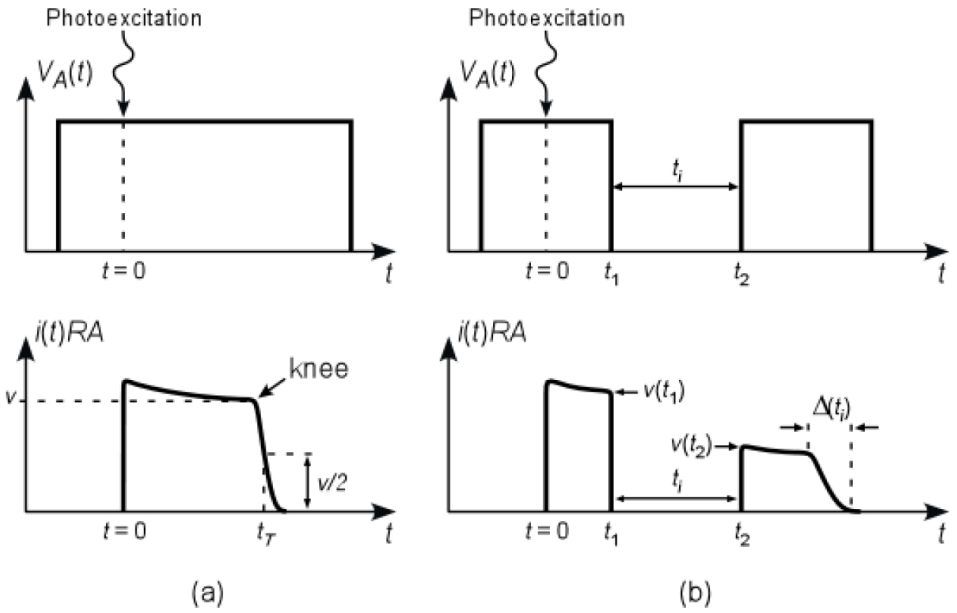

Figure 4.8: Transient voltage response for the a) TOF and b) IFTOF signal. The application of bias is given by $V_A(t)$. After Fogal [1].

The FWHM of the charge packet on exiting the sample can be used to determine if the interruption time was too long. Charge carriers are collected by the grounded electrodes if the interruption time is too long. The apex of the TOF tail marks the point at which the maximum amount of carriers are exiting the sample. Charge carriers are distributed asymmetrically about the charge packet maximum as a result of multiple trapping events with a disproportionately large amount of carriers leaving the sample after the maximum. The spatial distribution of the charge sheet would resemble a delta function at photoexcitation or at $t = 0$, however by the transit time at $t = t_T$, the charge carriers have undergone dispersion due to multiple trapping events as well as lateral spreading by eight mechanisms [6].

The velocity of drifting carriers under an applied field is given by the drift mobility

$$\mu = \frac{v_d}{F} = \frac{L/t_T}{V/L}, \tag{4.1}$$

where v_d is drift velocity, F is electric field, L is sample thickness, t_T is transit time, and V is voltage applied across the sample. The electric field is assumed to be constant under small signal conditions. The measurement of t_T therefore provides the drift mobility of the drifting carriers.

4.4.2 Lifetime Measurement with IFTOF

The IFTOF measurement is taken by interrupting the drift of photoinjected charge carriers as they cross the sample for a time interval t_i. The interruption typically occurs in the middle of the sample and is the result of the removal of bias. The photocurrent before (i_1) and after (i_2) interruption is compared and the fractional recovered signal i_2/i_1 measures the fraction of charge carriers drifting at the end of the interruption. As the photocurrent crosses the sample, current is induced in a variable sampling resistor. The current is measured by reading the voltage across the sampling resistor. The signal is amplified and captured by an oscilloscope. An RC rounding effect is introduced in the waveform measurement due to the nature of the bridge network. The sample and connecting wires have associated capacitances and resistances. The AC equivalent for the sample is a resistor and capacitor connected in parallel.

Charge carrier dispersion occurs during the interruption interval. The processes affecting dispersion are mutual coulombic repulsion and thermal diffusion. Experimental time (from $t = 0$ to t_T) can be related to the position of the charge sheet ($x = 0$ to L) within the sample since a constant drift velocity is assumed. Charge carriers are not collected at the electrodes as a result of dispersion occurring during interruption. The differentiation of the tail gives the charge carrier distribution in time as carriers exit the sample but also gives the maximum dispersion having occurred within the the time frame of the IFTOF experiment.

Lifetime τ is found by $i_2/i_1 = \exp(t_i/\tau)$ and a semi-log plot of i_2/i_1 versus t_i. The reciprocal of the slope of a regression line is used to find the lifetime τ.

4.5 TOF/IFTOF Experimental System

4.5.1 System Overview

The TOF/IFTOF experimental system is shown in Figure 4.9. A central component is the grounded bridge network which eliminates the displacement voltage present when applying a large bias across the sample.

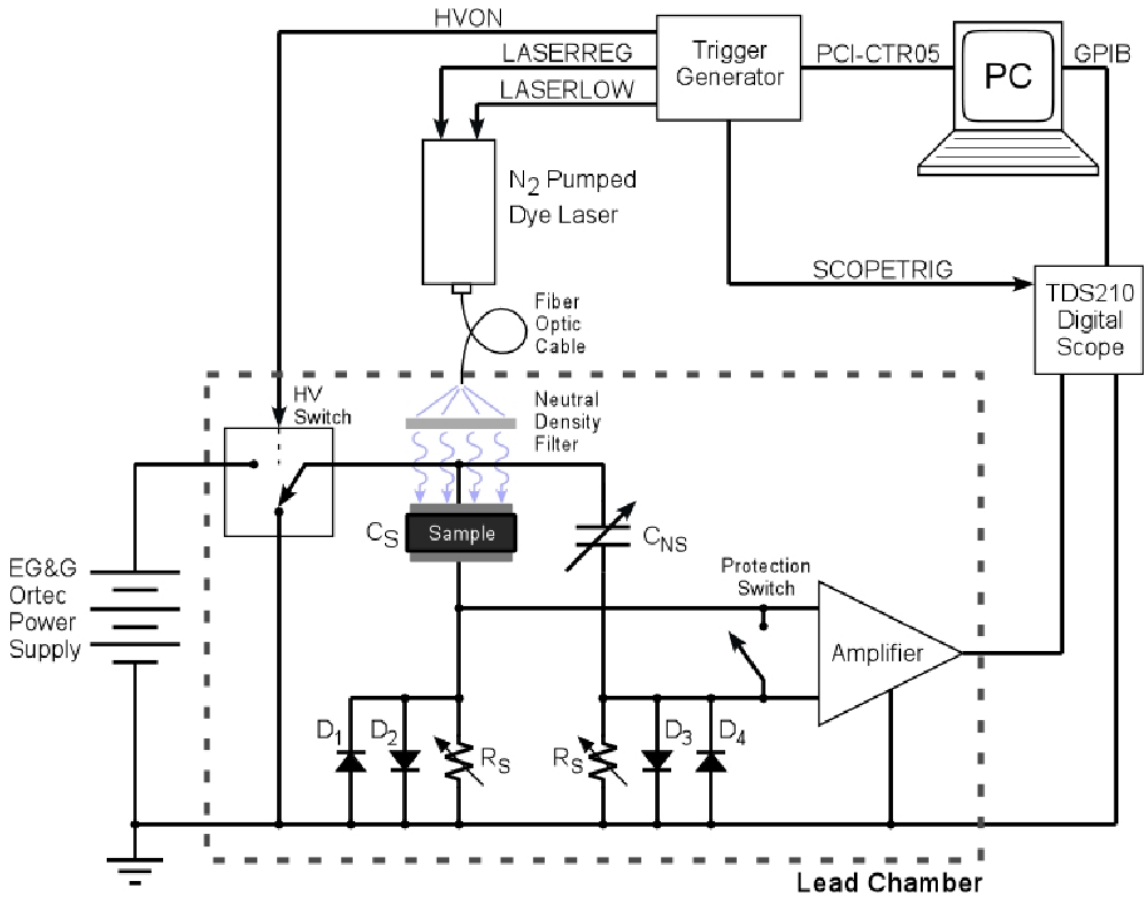

Figure 4.9: The TOF/IFTOF system schematic. The system is controlled via custom software interfacing a PCI-CTR05 counter board with a trigger signal generator. The waveform is collected from a digital oscilloscope via a GPIB interface. After Fogal [1].

The grounded bridge network consists of: ultra-fast switching rectifiers used to limit the displacement voltage, sampling resistors used to convert the photoinjected current into a voltage, a differential amplifier used to reject the common mode displacement voltage and switching transients, and an open air capacitor with a large breakdown voltage used to balance the bridge network.

A large displacement voltage is present during the application of the high voltage. The displacement voltage is limited using two ultra-fast switching rectifiers (MUR120) placed across each of the sampling resistors.

In the IFTOF experiment there is a large common mode switching transient. This common mode transient is rejected with the use of a differential amplifier placed across both bridge network sampling resistors.

Photoinjected charge moves in the electric field that has been set up across the sample by the high voltage source. The drifting charge induces a charge on the gold and aluminum/ITO electrodes. The induced charge flows through the sampling resistor and can be measured as a voltage signal.

A protection circuit is used to protect the amplifier inputs and is placed between the bridge network and amplifier. It is used to short the amplifier inputs during the initial switching transient.

The voltage was supplied by a EG&G Ortec 556H high voltage power supply. An HV HEXFET switch is used to apply voltage. A PCI-CTR05 counter board supplies the trigger signals for the switches, oscilloscope and laser. A Pentium II personal computer running Windows XP houses the counter board. The experiment was performed via a LabView custom GUI designed by George Belev. The oscilloscope used is a Tektronix model TDS210. A schematic providing a system overview is shown in Figure 4.9.

For the irradiation experiments, the sample was irradiated using a Gendex-1000 dental x-ray. Experimental equipment was housed inside of a lead cabinet. An image of the equipment is shown in Figure 4.10. The lead cabinet's purpose was to shield the experimenter from x-ray

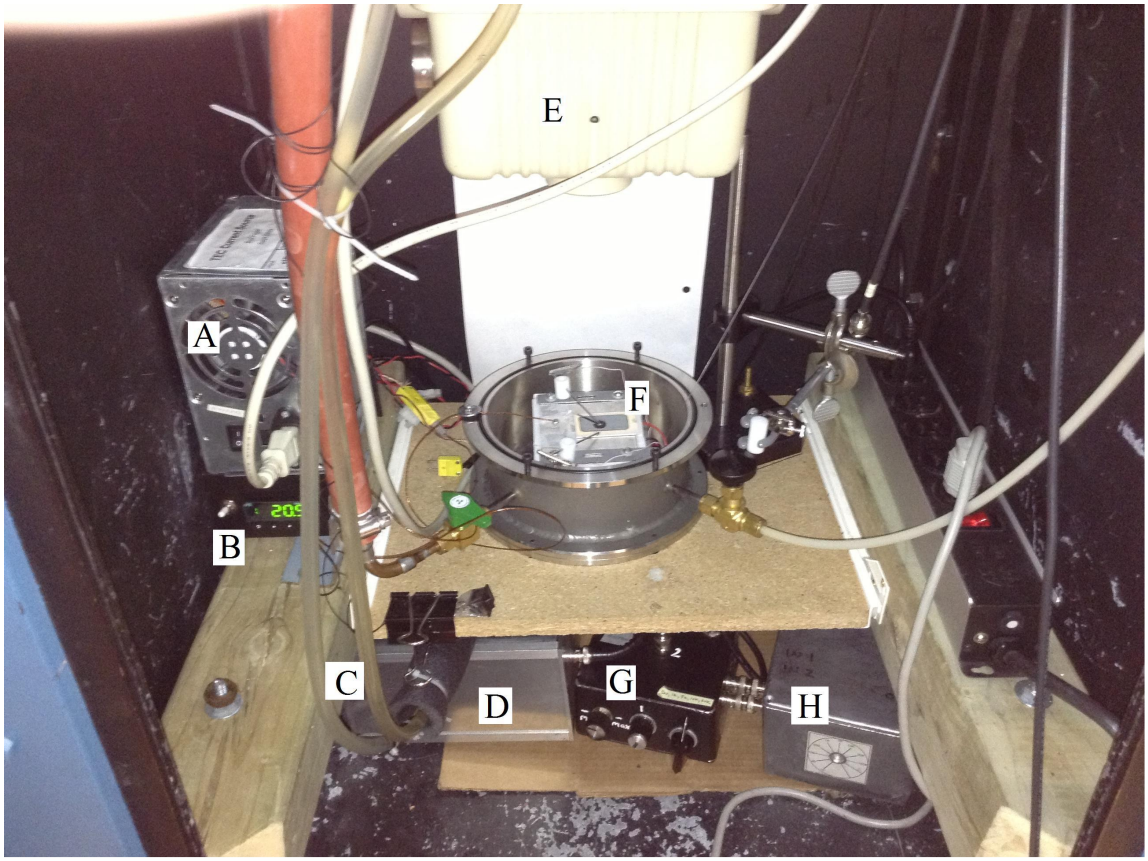

Figure 4.10: The inside of the lead chamber showing (A) the TEC current source, (B) PID temperature controller, (C) coolant circulation tubes, (D) the HV switch, (E) the x-ray tube, (F) the sample holder, (G) the bridge network, and (H) the differential amplifier.

radiation, and to block light. The experimental equipment was only partly stored in the lead cabinet. The lead cabinet had the following pieces of equipment stored in it: the TEC current source, the PID temperature controller, tubes for the circulation of coolant, the HV switch, the x-ray tube, the sample holder, the bridge network, and the differential amplifier. A requirement was placed on the proximity of some pieces of equipment. The requirement was that BNC connections be as short as possible. This was because BNC connections introduce capacitance into the system. An RC rounding effect is introduced when capacitance is added to the system. The equipment that needed to be in close proximity for this reason was the sample holder, the grounded bride network, the differential amplifier, and the HV switch.

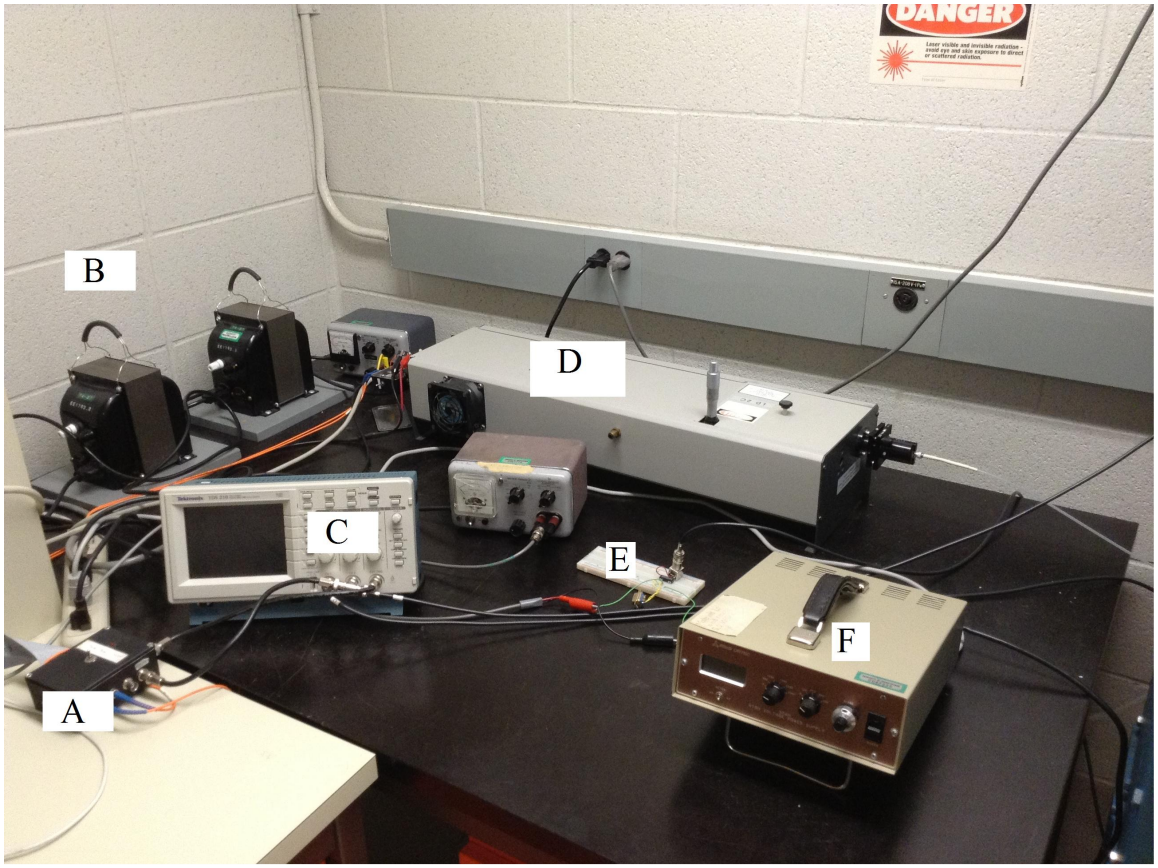

Figure 4.11: Experimental setup showing the (A) trigger generator, (B) ground isolating transformers (C) the TDS210 oscilloscope, (D) the laser, (E) the computer automated x-ray trigger, and (F) the HV power supply.

The experimental setup is shown in Figure 4.11. The experimental equipment shown are the trigger generator, ground isolating transformers, the TDS210 oscilloscope, the laser, the computer automated x-ray trigger, and the HV power supply.

Figure 4.12 shows an IFTOF waveform. The sample is composed of a-Se:As0.2%+2ppm Cl and is 74 μm. Two techniques were employed to eliminate the displacement voltage. A hardware technique and a digital substraction technique were used. This IFTOF experiment was performed under the following conditions: the interruption time was 60 μm, and the delay time was 25 μm. Lifetime was measured to be 148 μm. The protection circuit's operation is observed from $\sim t = 90 - 100$ μs in the figure. The interruption time is perceived from the figure to have been extended but was not. This is because the protection

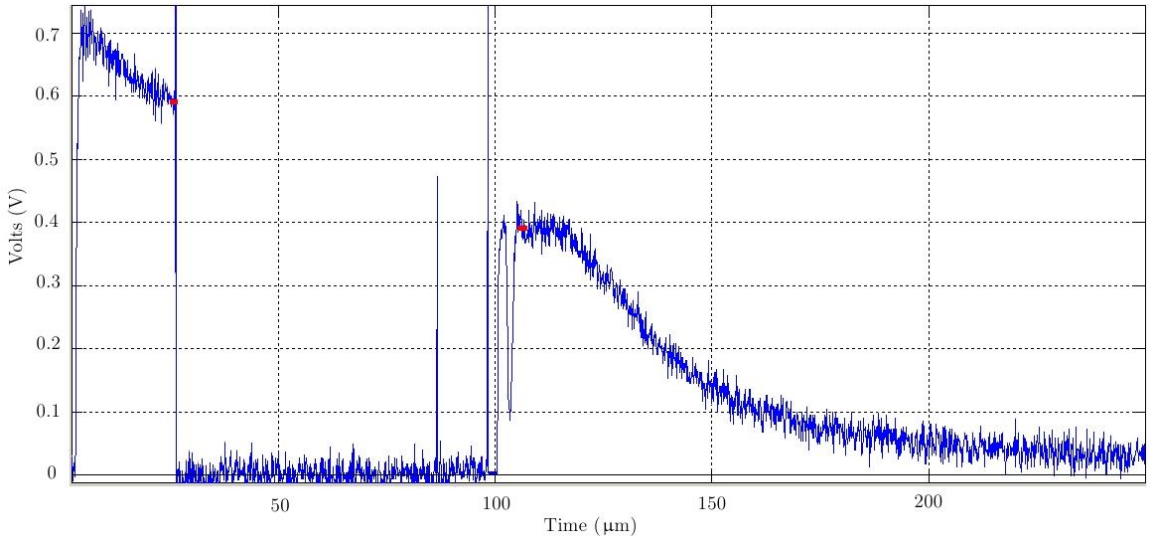

Figure 4.12: A displacement voltage free IFTOF signal for electrons in a 74 μm thick sample of a-Se:As0.2%+2ppm Cl. A 60 μm interruption begins at a time of 25 μm.

circuit nulls the amplifier output. The protection circuit is closed when the HV bias is re-applied. The protection circuit is open after a time interval t_s.

4.5.2 High Voltage Switch and Supply

The high voltage (HV) switch is shown in Figure 4.13. The HV switch has a maximum switching voltage of 1kV. The switch configuration used was a totem pole configuration. The design employs HEXFET switches. When driven into conduction, the HEXFET switch passes current from the high voltage input (HVIN) to the high voltage output (HVOUT). The type of HEXFET switch used was a fast switching n-chanel IRFBG30. The HEXFET has a maximum rated gate-source voltage of ±20 V. The power supplies were used to power the optocoupler and to switch the HEXFET. The power supplies applied a voltage to the HEXFET gate-source. The floating power supply voltage was +18V and was applied at point A in the figure. Optocouplers were used to isolate the control circuitry from the high voltage output of the switch. They were also used in order to provide the gate voltage required to drive the HEXFET into conduction. The upper optocoupler switch is closed when HVON is high. The purpose of the floating power supply was threefold: to provide power to the optocoupler, to provide the HEXFET gate-source with voltage, and to prevent

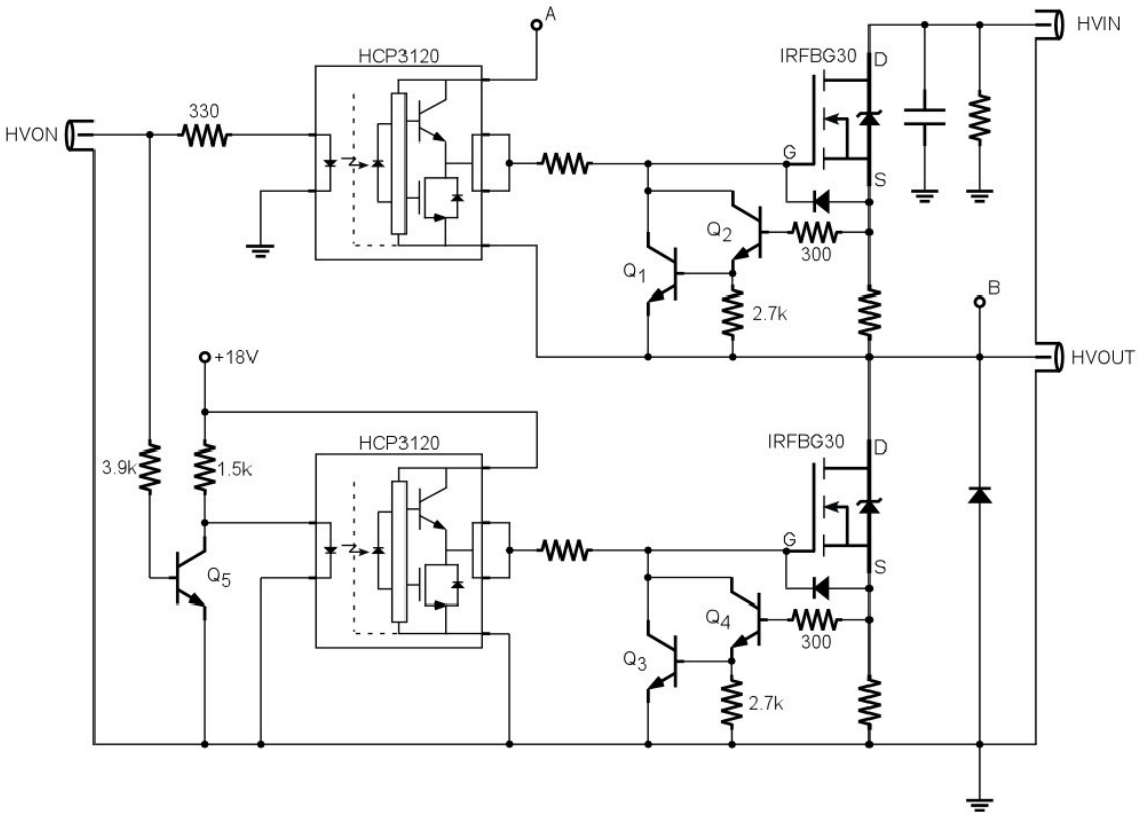

Figure 4.13: A 1kV fast switching high vooltage HEXFET switch. After Fogal [1].

the gate-source voltage of the HEXFET from exceeding its maximum rated value. The floating power supply voltage was +18 V. The design used a grounded power supply. The purpose of the grounded power supply was to supply the lower optocoupler with power and to provide the HEXFET gate-source with voltage. Fault protection is employed in the circuit. Fault protection is employed for the switch output. The design employed is a short circuit path between the gate and source terminals through a BJT follower, i.e. Q_1 and Q_3. Fault protection is achieved with a network of transistors ($Q_1 - Q_4$).

A high voltage switch operating as a single-pole double-throw (SPDT). It was capable of switching up to 1 kV. Fields of up to 10 V/ μm can be attained for samples of 100 μm in thickness. The switching time is 0.1 μs. Typical hole and electron mobility is 0.1 cm^2/Vs and 2×10^{-3} cm^2/Vs, respectively. A typical transit time for a hole TOF experiment is 2 μs requiring a switching time in the re-aplication of field in the IFTOF experiment to be ideally less than 0.1 μs, a tenth of the remaining transit time. Since the HV switch is designed to

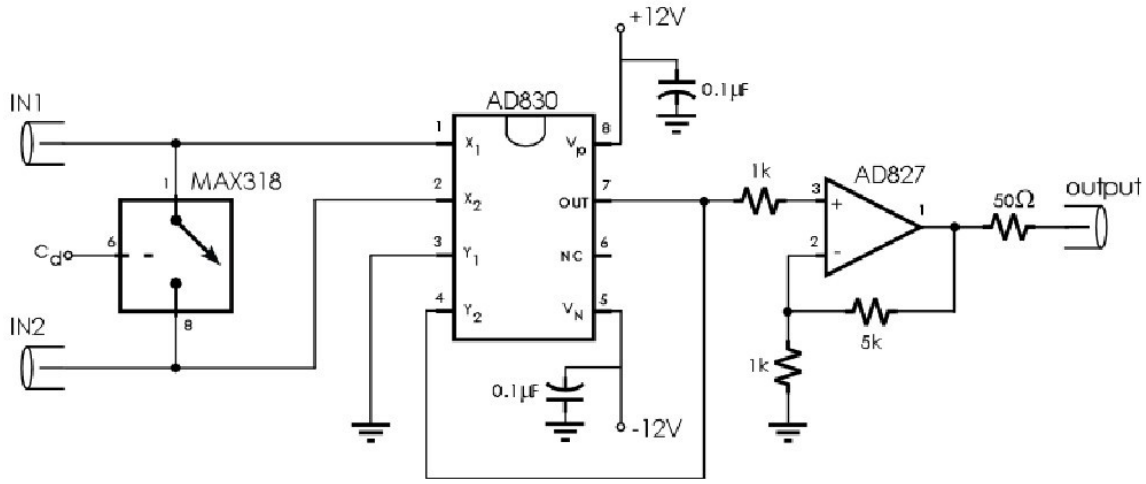

Figure 4.14: A 2-stage wide bandwidth difference amplifier with 16dB of gain. After Fogal [1].

work only with positive voltage input and output, the output connection is crossed when measuring the opposite charge carrier.

4.5.3 Amplifier

The amplifier has two stages. The first stage employs a differential amplifier op-amp. The differential op-amp employed is an Analog Devices AD830 amplifier. The amplifier has unity gain, a bandwidth of 85 MHz, and a CMRR of 60dB at 4MHz. The second stage employs a non-inverting amplifier. The amplifier used is an Analog Devices AD827 amplifier. The amplifier provides 16dB of gain. It is used to raise the signal above the oscilloscope noise floor. The amplifier circuitry is shown in Figure 4.14.

There is an additional stage added to the amplifier. It is added before the first stage. The purpose of the stage is to protect the circuitry. The circuitry needs to be protected from high voltage switching transients. This is accomplished by shorting the amplifier inputs. This stage employs a SPST CMOS analog switch. The switch employed is a Maxim MAX318. The switch is kept closed during the switching of the high voltage and also for a short time afterwards. Timing is controlled by an LS123 monostable multivibrator and an LS74 positive-clocked D flip-flop which are shown in Figure 4.15.

The protection circuitry is shown in Figure 4.15. The circuitry of the protection circuit

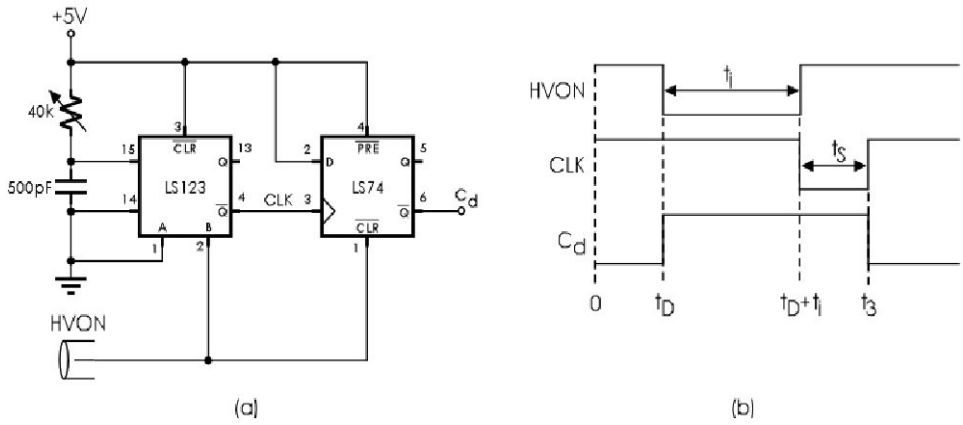

Figure 4.15: A circuit which controls the duration of amplifier protection. The circuit is shown in (A). The timing diagram is shown in (b). The protection interval t_s is adjusted using a 50 kΩ potentiometer. After Fogal [1].

is shown in Figure 4.15 (a). The timing pulse is shown in Figure 4.15 (b). The delay prior to amplifier activation following the application of bias (t_s) is controlled by a variable resistor. Not shown in the figure are two small diodes (1N914) connected in series with the supply pins on the MAX318 to provide overvoltage protection for the circuit.

The amplifier small signal response is shown in Figure 4.16. The square wave input pulse has an amplitude of 100 mV and a high period of $\sim$ 1.2 μs. The small signal gain is 16 dB. The small signal bandwidth is 12MHz. The bandwidth is derived from the output signal's rise time of 48 ns. The amplifier performs acceptably because experimental TOF measurements have a minimum pulse width of $\sim$ 1.0 μs.

4.5.4 Laser

The photoexcitation source used was a Laser Photonics LN103C nitrogen-pumped dye laser. The operating wavelength is 337.1 nm with 0.1 nm spectral spread. The peak power is 250 kW. The output pulse is 300 ps with a ±2 ns jitter.

A Newport optical fibre coupling adapter model number MM-2A is used at the exit aperture of the laser. The optical fibre leads to the sample where it is involved in photoinjection of charge carriers. Neutral density filters are placed in front of the laser exit aperture in

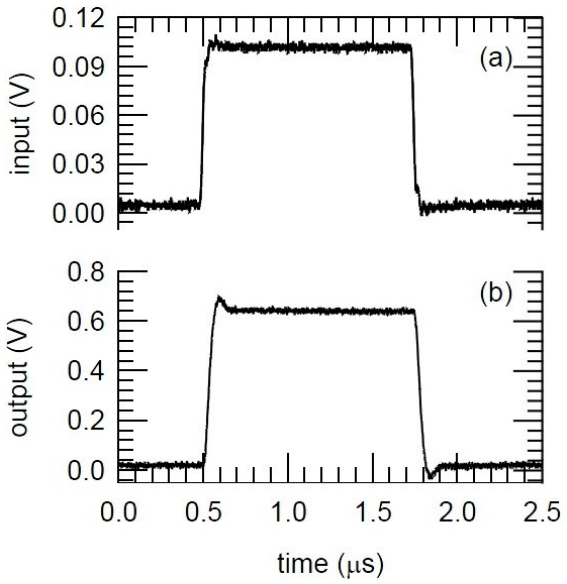

Figure 4.16: (a) A 100 mV pulse is applied to the input of the amplifier. (b) The output pulse. The differential pulse gain of the amplifier was measured to be 16 dB, and the signal bandwidth was estimated from the pulse rise time to be 12 MHz. After Fogal [1].

order to reduce the intensity of the beam. Minimal photoinjection is required in the IFTOF method for small signal conditions to hold.

Triggering is performed by two TTL signals of 100 ns duration. The laser is charged by a signal sent to *Trigger Reg*. The laser is fired by a signal sent to *Trigger Low* (LOW) which must be applied between 30 and 50 μs after *Trigger Reg* (REG) for controlled triggering otherwise the laser self fires 60 μs later with at most 50 ns jitter. Feedback to the trigger inputs as a result of laser discharge was eliminated using an optoisolator. A laser triggering timing diagram is provided in Figure 4.17.

4.5.5 Trigger Generator

Laser triggering is controlled from the computer. Signal timing was provided by a PCI-CTR05 counter board interfaced with the PCI bus. The counterboard utilizes an AMD 9513 timer. The timing chip contains five 16 bit up/down counters. The counter board is controlled at a high level by a library of manufacturer provided C++ functions. The C++ functions were called by a LabView GUI created by George Belev.

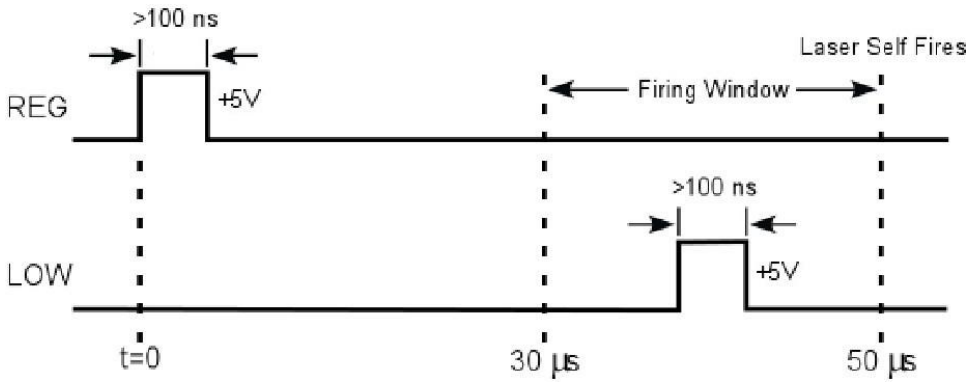

Figure 4.17: Trigger timing requirements of the LN103C nitrogen laser. After Fogal [1].

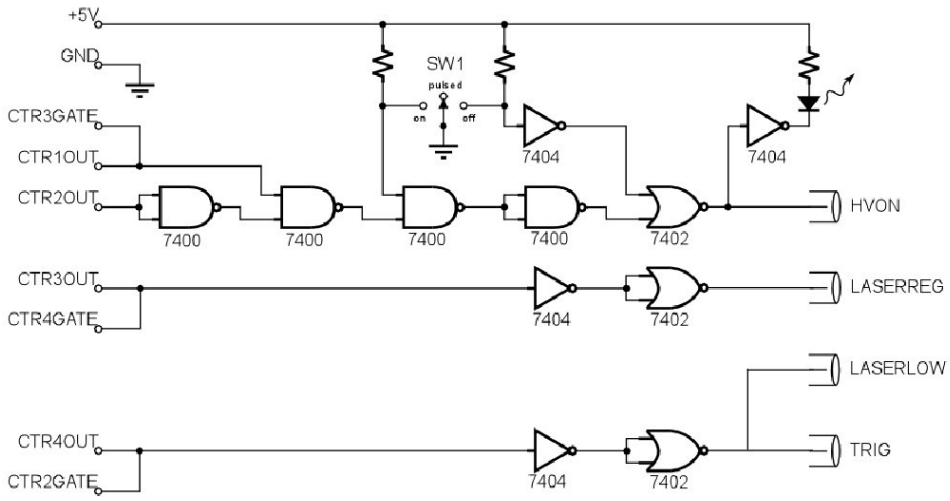

Figure 4.18: The PCI-CTR05 interface circuit for generating the trigger signals for the IFTOF system. After Fogal [1].

The counter board is interfaced with a trigger signal generator circuit shown in Figure 4.18. The interface circuit takes input from the counter board via a ribbon cable. The input is shown in the figure as control signals (CTR). The interface circuit is powered by the PCs power bus. A three setting manual switch allows for manual high voltage control. The switch settings are: on, pulsed, and off. For the IFTOF experiment the high voltage must be computer controlled which requires the switch to be set to pulsed. An LED provides visual feedback for the status of HVON.

A timing diagram is shown in Figure 4.19. The timing diagram shows signals from the counter board and trigger signal generator. Bias is controlled by the HVON trigger signal

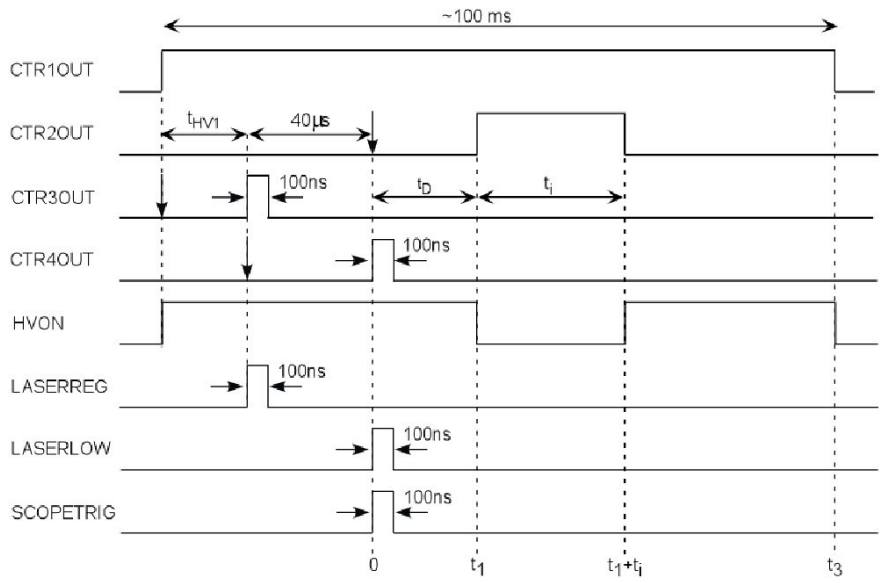

Figure 4.19: Timing signals from the PCI-CTR05 counter board and the interface circuit. After Fogal [1].

which activates the high voltage switch. The displacement voltage decays to a negligible amount during the time interval t_{HV1}. The laser is charged when LASERREG is high for 100 ns . The laser is fired when LASERLOW is high for 100 ns . LASERLOW must occur 40 µs after LASERREG. In order to record the photocurrent the oscilloscope and laser are triggered simultaneously.

In the IFTOF experiment the applied bias is interrupted and is resumed after an arbitrary delay time. The delay time is measured from the start of the IFTOF waveform. The start of the delay time interval is given by t_D. The interruption time is counted at t_D for a time interval t_i. Bias is reapplied after the interruption interval.

4.6 Signal Capture and System Interface

Signal capture was performed by an 8-bit Tektronix TDS210 digital oscilloscope with a sampling rate of 1 GS/s. The oscilloscope was interfaced with a PC using a GPIB connection. The data that was collected from the oscilloscope and transferred to the PC was stored as a floating point number. Noise reduction was performed by limiting the oscilloscope bandwidth to 20 MHz.

A GUI user interface was implemented on the PC. The GUI was developed by George Belev. LabView software was used to implement the GUI. LabView is a development environment with integrated tools which interface with a large number of laboratory instruments.

4.7 Temperature Control System

The temperature control system is comprised of two major components which are the temperature control chamber and the heater data acquisition and control system. The temperature control chamber is the physical construction which includes a sample holder and all the necessary components to ensure temperature control. The heater data acquisition and control system is the control system which regulates the sample temperature at the set point by executing a control loop.

4.7.1 Temperature Control Chamber

Sample temperature was adjusted using a heating and cooling element. A diagram of the temperature control chamber is shown in Figure 4.20. The sample was placed on a top metal block under which was a peltier cooler and $50\,\Omega$ heating resistor. The heating resistor added heat which dissipated into the top metal block while the peltier cooler drew heat away from the top block.

The peltier cooler had an area the size of the top block surface. The peltier cooler drew heat from its surface to its underside thus drawing heat from the top block to a second bottom block. Through the second bottom block was a network of tubing which was intended to circulate a coolant. This acted to dissipate heat drawn from the top metal block into the bottom metal block and out of the system via circulating water. The peltier cooler was 40×40 mm with a 6 A input and was manufactured by CUI Inc. The peltier cooler was controlled by a voltage controlled current source designed by Bud Fogal which takes a $0-10$ V input and outputs $0-4$ A.

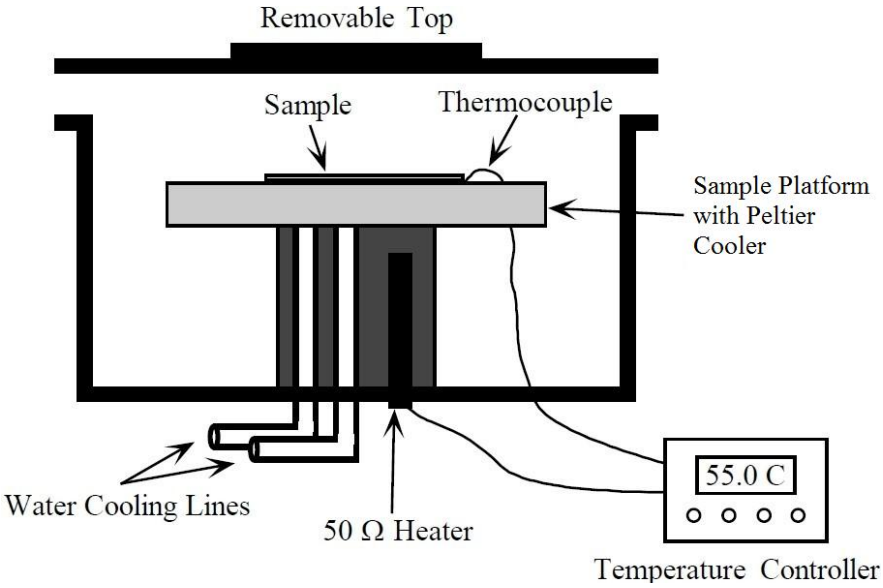

Figure 4.20: Chamber used to achieve sample temperature control. Not shown are copper cooling lines interspersed within a copper sample. The chamber was filled with Nitrogen in order to prevent condensation for 10 °C experiments. After Allen [2].

4.7.2 Heater Data Aquisition and Control System

Sample temperature was controlled using an Omega CNi32 iSeries PID temperature controller. A PID consists of three actions which contribute to the process control. P stands for proportional and is the range in error over which the gain is 100% and under which gain varies linearly. The proportional band is the band within which the controller's proportional action takes place. I stands for integral. The integral action incorporates previous process variable adjustment errors. D stand for derivative. The derivative action adjusts for any sudden changes in the process variable.

The integral component adds a gain which is proportional to the integral of the process variable error over an interval. The error is taken as the difference between the set point and the process value. The reset is taken as the period of the oscillation about the stabilized process value which is present with only the proportional band acting. When at the set point, integrating over the reset period results in an error integral of zero value. With P and I acting, the offset or droop from the setpoint, is compensated. The integral action gives large gain at low frequencies and low gain at high frequencies.

Derivative or rate looks to minimize gain changes when the process value undergoes large rate changes. This value seeks to minimize overshoot or undershoot. Rate is tuned once P and I are determined.

4.8 X-ray System

The x-ray source used in exposing a-Se samples to x-ray radiation was a Gendex GX-1000 dental x-ray system. The system is comprised of an x-ray tube producing wide spectrum x-ray radiation. The system has an aluminium half-value layer (HVL) of 2.5 mm. The HVL is the level of filtration required to half output intensity. The x-ray tube exit aperture is positioned 30 cm above the sample. The system operates with a tube current of 10 or 15 mA while the tube voltage varies from 50 to 100 kVp. The x-ray beam pulses at 1/60 th of a second impulses due to the system's use of a half-wave rectifier and a 60 Hz power supply. The system has a timer which can generate a succession of impulses for a duration from 1/12 th to 5 s. Cables are routed through the top of the cabinet.

The x-ray beam is described by two terms, intensity and quality. Intensity is described by fluence which has units $N[keVcm^2mAs]^{-1}$ @ 1 meter where N is the number of photons. Fluence is controlled by the tube current. Beam quality refers to the penetrating power of the x-ray beam which is a function of photon energy. Beam quality is controlled by the tube voltage which in turn affects the beam profile.

A lead chamber was used to in order to shield the experimenter from radiation. The lead chamber was manufactured by x-ray Products Corp. of Pico Rivera California. The model number of the unit is A9002-16. An image of the lead chamber is shown in Figure 4.21.

There is a limited rate of exposure above which the x-ray tube overheats. The x-ray tube is designed to dissipate heat but can only do so up to a maximum rate. The maximum allowed exposure in a five minute interval is given in Table 4.1. The unit of exposure is seconds.

X-ray radiation is a form of electromagnetic radiation. In the thesis experiments, an x-ray tube is used which produced x-rays via Brahmstrunlung and characteristic radiation

Figure 4.21: Lead chamber housing all experimental equipment mentioned which is not shown in Figure 4.11. The x-ray controls are mounted on the right hand side of the chamber.

Table 4.1: Maximum allowed exposure in a five minute interval. Unit of exposure is seconds. After Fogal [1].

KVp	**Exposure-seconds in 5 minutes (s)**	
	10 mA Setting	**15 mA Setting**
50-70	30	20
80	26	17.5
90	23	15.5
100	21	N/A

processes. In Brahmstrunglung radiation, a charged particle releases energy in the form of x-ray radiation under the law of energy conservation as the charged particle undergoes deceleration. This process occurs in the x-ray tube as an electron decelerates after hitting a target composed of high density and high atomic number atoms e.g. tungsten or molybdenum. In characteristic radiation, x-ray photons are emitted as excited electrons transit down to lower energy levels.

The x-ray tube has a hot cathode on one end releasing electrons and an oppositely charged anode rotating plate on the opposite end all of which is in a vacuum. Electrons are accelerated across the evacuated chamber and undergo a deceleration as they hit and enter the anode target. The target is composed of Tungsten. The energy conversion from kinetic energy to photon energy of the x-rays is approximately one percent with all other energy dissipated in the anode as heat.

Brahmstrunglung radiation is produced when accelerated electrons are deflected from an atom. The maximum energy emitted by this type of radiation is equal to the kintetic energy of the accelerating electron. The energy range of brahmstrunglung radiation is from the kinetic energy of the electron to close to the lowest end of the x-ray spectrum.

Characteristic radiation is produced as a displaced inner shell electron is replaced with an electron from a higher energy level. The displacement occurs from an interaction of an accelerated electron with an electron inside the atom.

X-ray attenuation occurs by: Rayleigh scattering, Compton attenuation, the photoelectric effect, pair production attenuation, and triplet attenuation. Rayleigh scattering involves the elastic scattering of a photon when it interacts with atomic electrons. Compton attenuation involves the inelastic scattering of an x-ray photon, producing an ejected electron and an ionized atom. The photoelectric effect occurs when all of an x-ray photon's energy is passed to an ejected electron. Pair production attenuation occurs when an x-ray interacts with the electric field of a nucleus producing a positron and a neutron. Triplet attenuation occurs when an x-ray interacts with the electric field surrounding an orbital electron producing an ejected electron and a negatron/positron pair. Of these, in the case of a-Se, over the range

of x-rays used in this work, the photoelectric effect is the most dominant [73].

4.9 Summary

In this chapter, the experimental procedures used throughout the course of this work were outlined. The samples used in the experiments were prepared by conventional vacuum deposition techniques. A top electrode was placed by gold sputtering. Electron lifetime was measured using the IFTOF technique. The technique interrupts the drift of charge carriers by halting the applied bias. Baseline subtraction and a grounded bridge network are employed to remove the effects of the displacement voltage. Lifetime is calculated from the fractional recovered photocurrent. The sample temperature was controlled by a PID feedback loop. The sample was irradiated by an x-ray tube. Described were the IFTOF system, temperature control system, and x-ray system.

5. Results and Discussion

5.1 Introduction

Lifetime is an important device performance indicator as it is a key charge transport property. A change in lifetime therefore leads to a change in device performance.

The recovery and irradiation experiments were performed under low and high field at different temperatures. The temperatures were 21 °C or 35 °C and in some cases 10 °C. The field was either 0 V/µm or 5 V/µm.

A change in lifetime with respect to dose was observed in the irradiation experiment. A decrease in lifetime was observed immediately following an absorbed dose. The lifetime recovered to its equilibrium value following the cessation of irradiation.

A method for calculating the change in lifetime per unit dose, the structural relaxation time, and the thermal activation energy of the recovery process are provided.

5.2 Lifetime

This section covers the interrupted-field time-of-flight (IFTOF) measurement method and a method for calculating lifetime. The IFTOF technique is the sole measurement technique used in this thesis.

5.2.1 IFTOF Background

Lifetime is calculated from the fractional recovered signal (FRS) and from the corresponding interruption time (IT) as taken from a TOF waveform. A typical IFTOF waveform is shown in Figure 5.1. The FRS at various ITs is measured. A regression line fit of the dataset

is used to calculate the lifetime. The slope of a best fit line to a logarithmic plot is used to find the lifetime. A typical FRS vs. IT plot is shown in Figure 5.2.

The IFTOF measurement method begins with the photogeneration of charge carriers as a result of strongly absorbed optical radiation. Charge carriers drift across the sample by the application of an electric field and are interrupted half-way through the sample. Deep trapping is allowed to occur during the arbitrarily chosen interruption time. Drift is resumed upon the reapplication of field and the signal drops as carriers leave the sample.

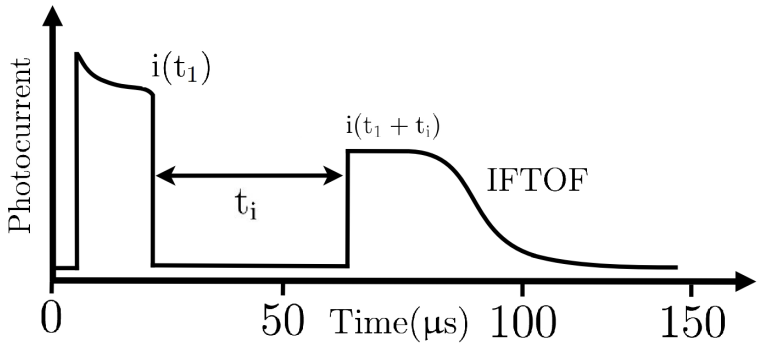

Figure 5.1: Schematic of an IFTOF waveform showing photocurrent versus time. Drift is interrupted at t_1 and resumed at $t_1 + t_i$. The interruption time is t_i.

The IFTOF technique is practically limited by a high voltage switching transient which has the potential to damage sensitive differential operational amplifiers. This makes the recovered photocurrent difficult to measure. A protection circuit operating for the duration of the transient is employed which shorts the inputs for 10 μs.

Lifetime is calculated using equation 5.1,

$$\frac{i_2}{i_1} = \exp\left(-\frac{t_i}{\tau}\right) \tag{5.1}$$

where i_2 is photocurrent after interruption, i_1 is photocurrent before interruption, t_i is interruption time, and τ is the deep trapping time or lifetime. This lifetime represents the average value within the period t_i.

Normalized lifetime values were calculated as follows

$$\tau_{i_{\text{normalized}}} = \tau_i / \tau_{\text{rested}}, \tag{5.2}$$

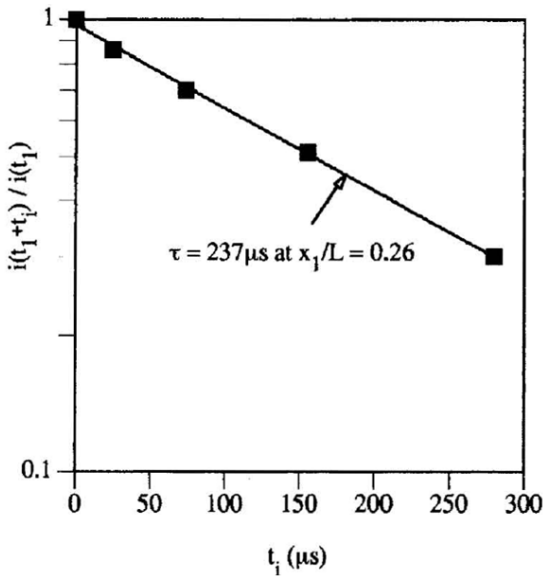

Figure 5.2: The linear regression straight line fit of IFTOF data. Plotted on the semi-logarithmic axis is th FRS. The IT is given by t_i. After Haugen [11].

where $\tau_{i_{\text{normalized}}}$ is the normalized lifetime, τ_i is lifetime with a measurement index number i, and τ_{rested} is the lifetime of the rested sample.

5.2.2 Measurement Technique

The Error in the Lifetime Measurement

It is important to evaluate the error involved in the lifetime measurement in order to determine the level of confidence that should be placed in any dependent calculations. The standard deviation of lifetime is found by using the propagation of error equation. Assuming no covariance between variables x and y of the function f, the standard deviation of the function is given by the propagation of error equation (5.3) [74]

$$\sigma_f = \sqrt{\left(\frac{\partial f}{\partial x}\right)^2 \sigma_x^2 + \left(\frac{\partial f}{\partial y}\right)^2 \sigma_y^2} \tag{5.3}$$

In the IFTOF experiment, the fractional recovered signal is given by equation (5.1).

Solving for the lifetime, gives

$$\tau(t_i, i_2, i_1) = -\frac{t_i}{\ln(i_2/i_1)}. \tag{5.4}$$

Applying the propogation of errors equation to equation (5.1) gives the expression for the standard deviation of lifetime (σ_τ). It was assumed that the lifetime is normally distributed. This assumption was shown to be valid in section 5.2.2.

$$\sigma_\tau = \sqrt{\left(\frac{\partial\tau(t_i, i_2, i_1)}{\partial t_i}\right)^2 \sigma_{t_i}^2 + \left(\frac{\partial\tau(t_i, i_2, i_1)}{\partial i_2}\right)^2 \sigma_{i_2}^2 + \left(\frac{\partial\tau(t_i, i_2, i_1)}{\partial i_1}\right)^2 \sigma_{i_1}^2} \tag{5.5}$$

Lifetime Parent Distribution

The standard deviation of lifetime is calculated with the propagation of errors equation. It assumes that the lifetime is normally distributed. The probability that the lifetime is normally distributed is given by the p-value.

In order to determine the parent distribution, a sample of lifetime measurements was taken. The measurements were repeated every 5 or 10 minutes. Forty three measurements were taken at 5 minute intervals and 14 measurements were taken at 10 minute intervals.

When measurements were taken every 5 or 10 minutes, the mean lifetime values were 175.9 μs and 169.5 μs respectively with a standard deviation of 11 μs and 7.28 μs respectively. A reduction in the standard deviation is therefore observed with a longer rest interval between measurements.

A Chi-squared test was performed in order to determine if the repeated measurements follow a normal distribution. The p-value determined from the test indicates the probability that the data were randomly generated. For the 5 and 10 minute experiments, the p-values were 0.32 and 0.76, respectively. The 5 minute experiment is likely to have a normal parent distribution having only a 32% chance of coming from a random distribution, while the lack of likelihood in the 10 minute experiment may result from a low sample number (14 measurements taken at a 10 minute interval as compared to 43 at a 5 minute interval). The

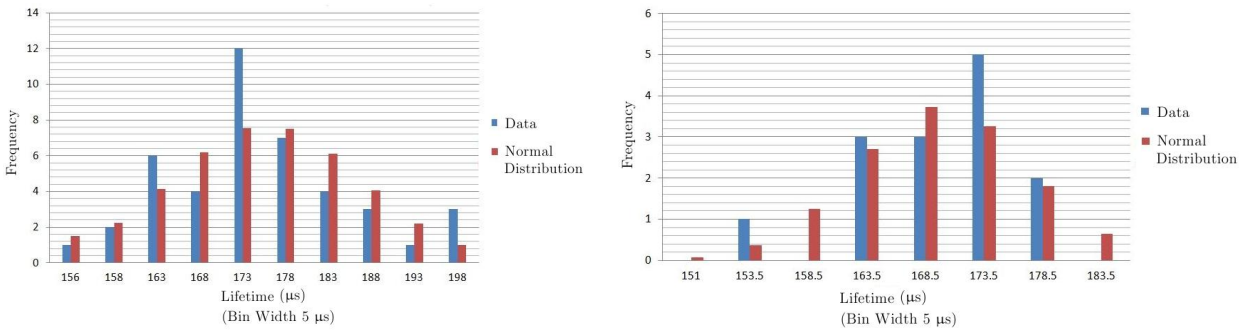

Figure 5.3: Frequency plots of measured lifetime at five (left) and ten (right) minute intervals. A normal parent distribution is provided (red) for comparison.

distribution of measured lifetimes is shown in Figure 5.3 for the two cases.

5.2.3 Sample Temperature

In order to measure the sample temperature, the sample was placed adjacent to a blank glass slide on the sample holder. Attached to the slide was a thermocouple. The sample temperature was assumed to be the same as the slide. The slide was identical to the ones used in deposition. In a control experiment, it was observed that the temperature did not vary significantly across the holder. PID temperature conrol was used to reach a temperature stability of ± 1 °C and was not used at room temperature. Although 21 °C has been indicated for the room temperature, the actual experiments were performed at $20 - 22$ °C due to seasonal changes.

A control experiment was performed measuring the change in the lifetime as a function of temperature for sample B2 (a-Se:0.2% As) as shown in Figure 5.4. The experiment was performed from 10 °C to 35 °C over which the lifetime changed by $\sim 63\%$. It was therefore inferred that a 1 °C change would cause a change of $\sim 2.5\%$ in the lifetime. Consequently, room temperature lifetime measurements can show a fluctualtion of 2.5% due to a temperature fluctuation of 1 °C. If a thermally activated process is assumed as shown in the drawn line of Figure 5.4 and given by $\tau \sim \exp(\varepsilon/kT)$, the hopping activation energy is given by $\varepsilon = 0.224$ eV.

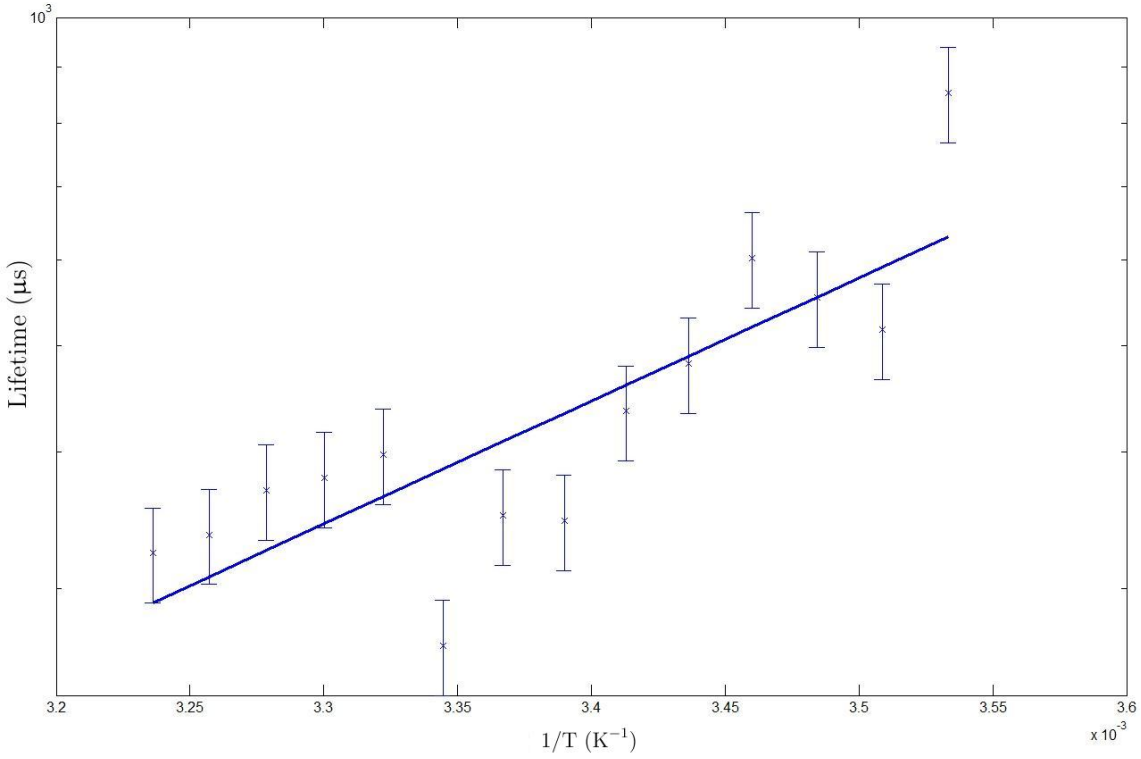

Figure 5.4: Temperature versus lifetime plot for sample B2 (a-Se:0.2% As).

5.2 Normalized Lifetime Change Rate

A decrease in lifetime is observed with a deposited x-ray dose. The rate of decrease in lifetime upon an absorbed dose is designated in this thesis as a normalized lifetime change rate (NLCR) which refers to the change in normalized lifetime with absorbed x-ray dose. In the irradiation experiments, the temperature and the field were varied and changes in NCLR were observed. A method of calculating NLCR was derived which incorporates lifetime recovery between measurements.

5.2.1 Background

X-ray irradiation induces metastable deep trap centres in selenium which result in a change in the carrier lifetime. The created trap centres are either neutral or charged centres [75]. Photoinduced structural change has been observed in other amorphous semiconductor materials of different structure. As an example, the structural change in hydrogenated amorphous silicon (a-Si:H) is associated with the creation of metastable dangling bond defects [76]. Photoinduced effects are well known in the case of chalcogenide glass semiconductors [13]. It is therefore not completely unexpected that the observations in this work seems to show that x-ray irradiation induces deep traps.

It was observed that structural change generally increased with temperature. A similar increase in structural change is observed in polymers. In polymers, radiation of sufficient energy causes molecular chain scission with a weakening bond and embrittlement of the material. The change is increased under exposure to both elevated temperatures and radiation [77]. Selenium is composed of polymer-like chains and may experience a similar increase in structural changes under exposure to both elevated temperatures and radiation.

Photodarkening is a photoinduced increase in absorption, which reduces α^{-1}, and which tends to limit the photodarkened layer to the penetration depth of light. The photodarkening phenomenon is inherent to, or substantially prominent in, amorphous chalcogenides and is universally observed in covalent chalcogenide glasses including amorphous selenium (a-Se). It is well established that bandgap or sub-bandgap illumination of a-Se causes photodarkening. There is the appearance of well-separated metastable coordination defects associated with

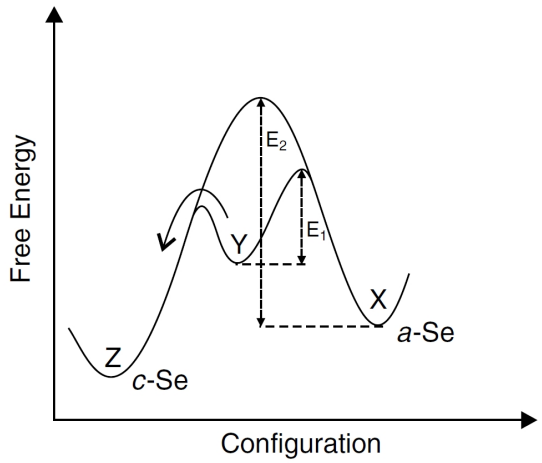

Figure 5.5: An a-Se energy diagram of the creation of crystallization defects at low temperatures via transition states associated with light-induced metastable bond distortion. X is the amorphous state, Z is the crystalline state, and Y is a light-induced transition state. A potential barrier of height E_1 prevents the $Y \rightarrow X$ transition at low temperature. In the absence of light-induced defects, the barrier of height E_2 prevents the $X \rightarrow Z$ crystallization transition of a-Se. After Reznik [12].

valence-alternation pairs (VAP) with illumination [78, 79]. a-Se develops a double-well state in which the ground state and the metastable state of the coordination defect is separated by a potential barrier (E_1) that prevents the immediate restoration of the virgin a-Se structure at low temperatures [80]. The double-well state is shown in Figure 5.5. Heating a-Se increases the probability of the transformation of distorted bonds back to perfect amorphous bonding [12]. The optical effect of photodarkening is transient and decays rapidly on cessation of the illumination leaving only the normally observed metastable effect.

Many experiments have been performed on As_2S_3 however the effects of (ultra-)super-gap light, i.e., soft x-ray, which can excite core electrons and/or bonding electrons, remain to be studied [13]. It is not surprising then that such a study has not been performed for a-Se which is relatively less studied for its photodarkening properties.

Photodarkening may have occurred in the entire bulk of the sample with all thesis samples as the penetration depth in a-Se of the most energetic x-rays emanating from a 75 kVp x-

ray tube is 930 μm while the thesis samples had a maximum thickness of 155 μm. Three photodarkening strucutral models in a-Se have been suggested: bond-twisting, structural changes through defect creation, and coulomb layer movements. Structural changes through defect creation are of three types: defects in which the initial bonds are restored, defects in which new bonds are formed between atoms belonging to different chains, and defects that result in the formation of pairs of threefold and onefold coordinated sites. The three photodarkening strucutral models are shown in Figure 5.7.

A configuration coordinate model has been used by several researchers [81–83], to delineate more detailed features for the atomic structural changes. For example, a model has been proposed for chalcogenide glasses by Tanaka [81] which quantitatively explains the variation in photodarkening with laser intensity, temperature, and exposure time. The model proposes a stable ground state X and quasi-stable state Y. Photodarkening arises from a band gap excitation in which the energy configuration changes from $X \rightarrow Z' \rightarrow Z \rightarrow Y$. Annealing assists the thermal relaxation process $Y \rightarrow X$. In g-As_2Se_3 the thermal activation energy of the annealing process is estimated to be $0.5 - 1.5$ eV. The mechanisms of the thermal relaxation process cannot be made clearer because of subtle structural changes which cannot be experimentally identified [13]. The dynamics of the transformation is therefore more speculative. The average thermal activation energy in the a-Se alloy thesis samples was approximately 1.4 ± 0.4 eV which is in the aforementioned range of g-As_2Se_3. Photodarkening of the samples in this work may be suggested. The configuration coordinate model may therefore be useful in explaining the thermally activated relaxation in the samples of this work.

In the electron IFTOF experiment, the electron charge carriers in the drifting charge sheet can recombine with trapped holes in the bulk resulting in a lower lifetime measurement. In the irradiation experiment, x-ray induced deep hole traps may have trapped holes from x-ray photo-induced electron-hole pairs (EHP). A similar effect has been suggested in a-Se in the x-ray induction of deep electron traps in which a decrease in hole lifetime was accompanied with an increase in residual charge potential across the sample (an increase in trapped electrons in the bulk) [84]. During the recovery experiments, this defect induction and EHP

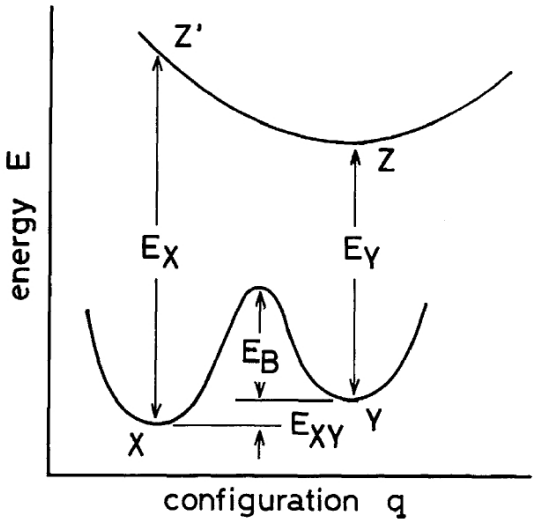

Figure 5.6: An energy configuration model for photodarkening. After Tanaka [13].

trapping would have occurred during exposure times of as much as 20 s. Fewer holes would be trapped when exposing under an applied field as x-ray induced holes would spend less time in the bulk of the material. If this were the case, a decrease in NLCR would be observed with an increase in field. The experimental results do not agree with this prediction which may imply that x-ray induced deep hole traps do not play a dominant role in determining NLCR.

Dose Calculation

The mechanisms of gamma and x-ray matter interactions are: photoelectric absorption, Compton scattering, and pair production. The absorbed dose is a function of photon energy. Fluence is the distribution of photon intensity vs. energy in an x-ray beam. Fluence-to-dose conversion factors are used to estimate the absorbed dose. Dose can alternatively be calculated by local fluence in an absorber. Dose is measured in Grays (Gy) and has SI units of absorbed energy in Joules (J) per unit mass (Kg).

A method for calculating dose as well as a cross sectional energy deposition profile are provided in this section. A brief description of the method is as follows: an ideal x-ray tube fluence is obtained from a simulation running a theoretical model. This fluence is then

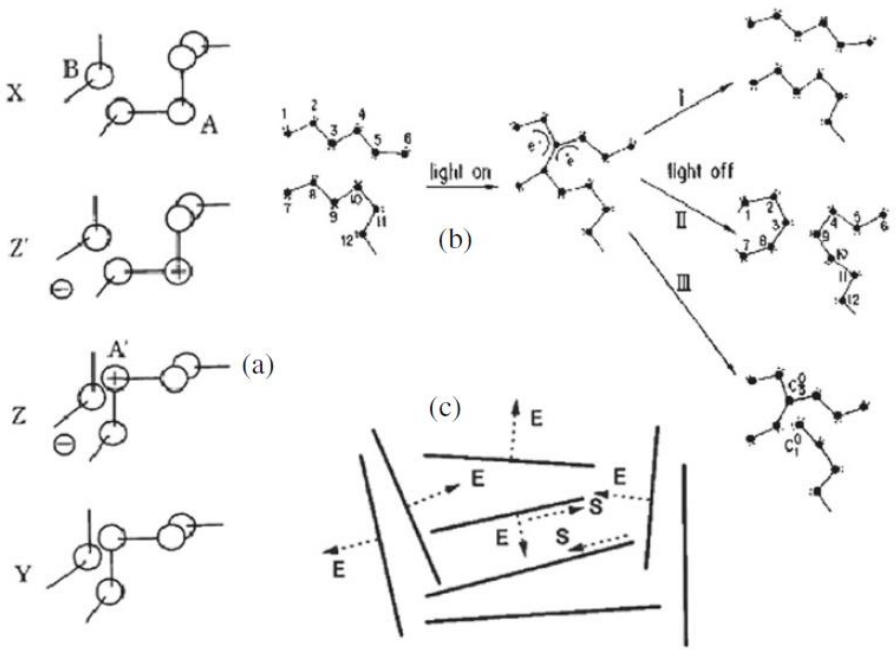

Figure 5.7: Structural models for photodarkening assuming (a) bond-twisting, (b) structural changes through defects, and (c) Coulombic layer movements. After Tanaka [13].

adjusted to fit the experimental conditions. Dose is then calculated with known material properties and parameters.

Experimental x-ray tube fluence is found by multiplying the ideal fluence by a factor of actual to expected ion chamber charge. The expected charge is found from the number of generated ions and the elementary charge. The number of ions are found with the ionization energy of air and the fluence. The measured charge is found with an exposure measurement and the definition of a unit of exposure (Roentgen).

The dose calculation is performed using parameters derived from the exposure conditions and sample parameters. The sample parameters include: area, thickness, density, and absorption coefficient.

It is assumed x-ray travel is parallel. The density of air is taken at room temperature and at sea level. Ionization chamber partial volume effects are minimized by the exposure of the whole active area which would otherwise result in unusable measurements.

The NIST value for density of air at sea level and at room temperature is $\rho_{air} = 1.205 \times 10^{-3}$ g/cm^3. X-ray attenuation coefficients are taken from the NIST web site [14]. The air and selenium attenuation coefficient profiles are given in Figure 5.8. The NIST web site provides the mass attenuation coefficient and energy absorption coefficient in units cm^2/g. Energy of the listed data is in units keV.

An ideal W anode spectrum at 75 kVp was downloaded from the Siemens website [85]. Energy and fluence are listed in units keV and cm^{-2} respectively.

The average ion pair formation energy for air is given by $W_{air} = 34.4$ eV. The Keithley 96035 ion chamber itself has the following parameters: Volume of $V = 15$ cm^3, thickness of $D = 1.2$ cm, and area given by $V/D = 12.5$ cm^2.

The attenuation coefficients were interpolated which was performed by taking the logarithm of the photon energy and the attenuation coefficient, linearly interpolating the values, and then applying the inverse transformation.

The density of a-Se is required in the calculation and has a value of $\rho_{\mathrm{Se}} = 4.3$ g/cm^3, as

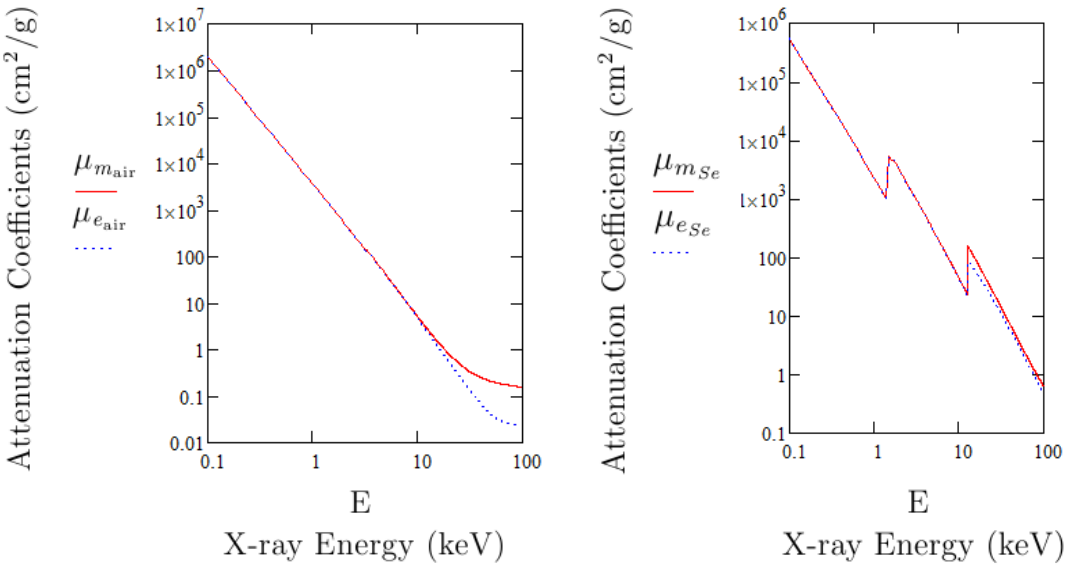

.

Figure 5.8: Attenuation coefficient of air (left) and selenium (right) versus x-ray energy. Shown is the mass attenuation coefficient (red) and the energy attenuation coefficient (blue). X-ray attenuation coefficients are taken from the NIST web site [14]

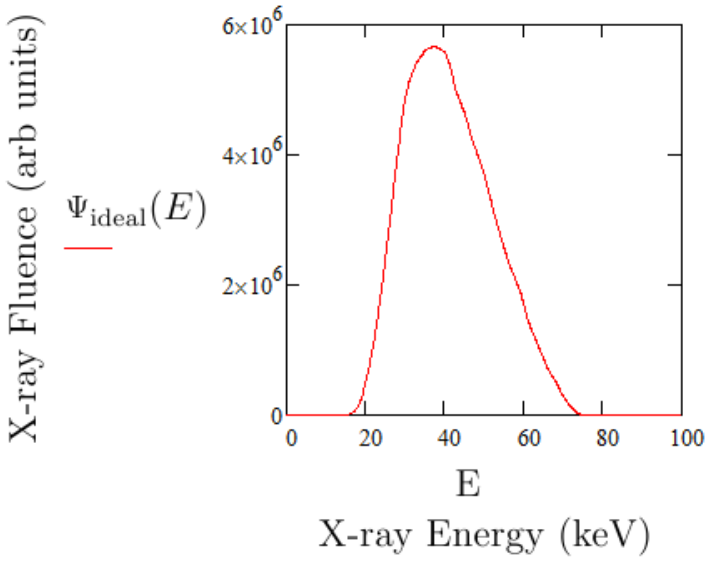

Figure 5.9: Idealized x-ray spectrum of a W anode x-ray tube operating at 75 kVp.

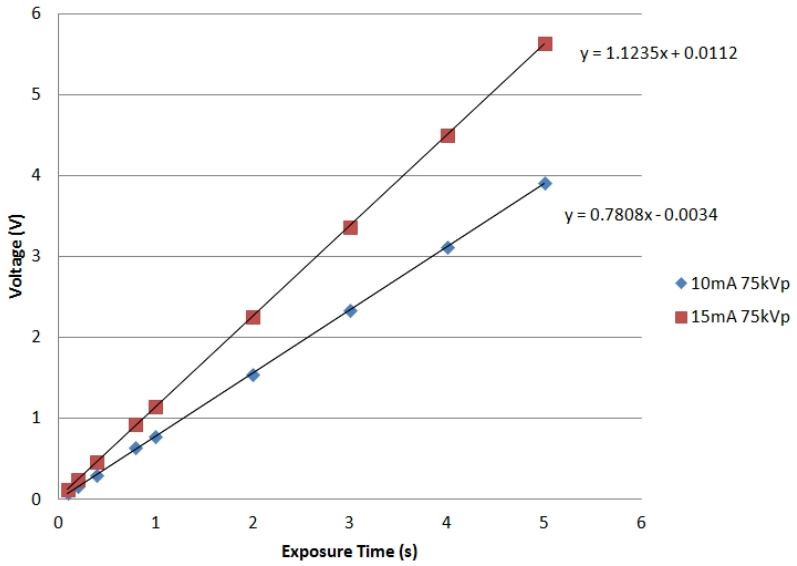

Figure 5.10: Ion chamber integrated voltage versus x-ray exposure time under experimental conditions of a W anode at peak voltage of 75 kVp and tube currents of 10 mA and 15 mA.

opposed to c-Se which has a higher density (~ 4.8).

The experimental fluence is required to find NLCR. It is calculated from the multiplication of an ideal fluence and a correction factor found by ion chamber exposure measurements. The collected ion chamber charge is converted to an integrated voltage. Figure 5.10 shows integrated voltage vs. exposure time at a peak voltage of 75 kVp and a tube currents of 10 mA and 15 mA. Also plotted for comparison is integrator voltage vs. exposure time at a tube current of 10 mA. The ion chamber used to collect ionized charge is connected to a voltage integrator which outputs a voltage with a calibrated conversion factor of 0.743 Roentgen/Volt. From the trendline plotted on the figure, one second of exposure results in an integrator voltage of 1.124 V and corresponds to an exposure of 0.835 R.

The dose calculation is shown in the next section. Table 5.1 summarizes the dose after one second of exposure. Variation in the density of alloys was not factored into the calculation as dopants comprised a maximum of 0.3 % of the composition. X-ray absorption in all alloys is assumed to be equivalent to pure a-Se.

An assumption has been made that the dose is uniformly distributed across the sample.

Table 5.1: Absorbed dose in one exposure second for listed samples. The W anode x-ray tube setting is 75 kVp peak voltage and 15 mA tube current.

Sample	Thickness (μm)	Dose (Gy)
pure a-Se (Sample A)	155	0.478
a-Se:0.2% As (Sample B1)	140	0.492
a-Se:0.2% As (Sample B2)	155	0.478
a-Se:0.2% As + 2 ppm Cl (Sample C1)	74	0.567
a-Se:0.3% As + 100 ppm $CaCl_2$ (Sample C2)	131	0.501

Exponential decay however is seen in the deposition profile of Figure 5.14. The dose calculation can be made more accurate by accounting for the position of the charge sheet in the sample at the time of interruption. The delay time would be used in such a calculation.

5.2.2 Irradiation Effects on the Lifetime

Experimental Sequence

The irradiation experiment sequence is shown in Figure 5.11. The sample temperature is maintained the same throughout the sequence. The lifetime is measured which is followed by irradiation under an applied field. The sequence is repeated every five minutes. Dose is increased until x-ray induced change in the lifetime is negligible upon which dose is increased. Dose is increased until the lifetime measurements produce repeatable lifetime values. The shortest lifetime observed is a function of the x-ray tube peak voltage and may not be the shortest achievable lifetime.

A typical irradiation experiment plot is shown in Figure 5.12. The figure shows an estimated initial drop in the lifetime upon irradiation (solid gray line) and a recovery leading up to a subsequent measurement (dotted gray line). The recovery characteristics were examined in a separate experiment. Least squares regression is used to fit the normalized lifetime change rate (NLCR) to the data.

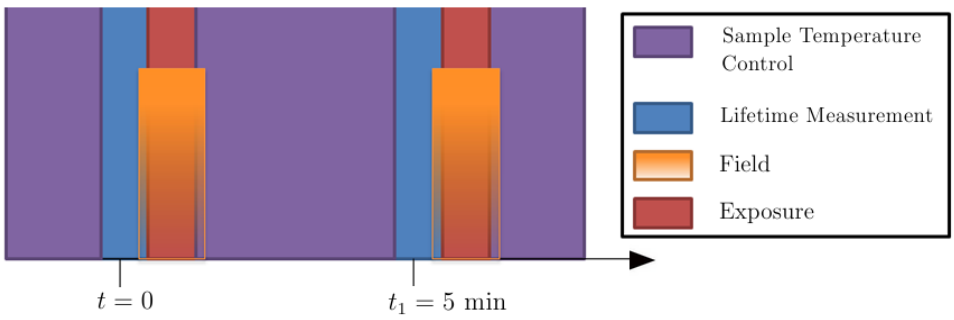

Figure 5.11: Irradiation experiment sequence diagram detailing temperature control, exposure, lifetime measurement and sample exposure.

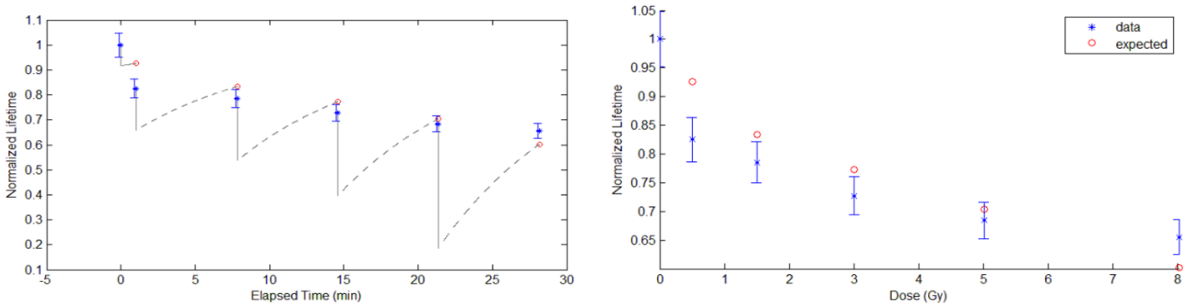

Figure 5.12: Typical irradiation experiment plots showing changes in lifetime with respect to elapsed time (left) and absorbed dose (right). Right hand plot does not take into account the elapsed time.

Calculation: NLCR

NLCR is calculated using a lifetime, elapsed time, and dose dataset. The recovery curve was observed to follow an exponential recovery, that is

$$\tau_t = 1 - (1 - \tau_o)e^{-\frac{t_r}{\tau_{sr}}}, \tag{5.6}$$

where τ_t is the lifetime at t, $\tau_\circ$ is the resting lifetime, t_r is the recovery time since the last dose, τ_{sr} is the structural relaxation time (a time constant that is characteristic of the structure).

The lifetime immediately after irradiation is given by

$$\tau_{i_{\text{expected}}} = \tau_{i_{data}} + \xi D, \tag{5.7}$$

where $\tau_{i_{\text{expected}}}$ is the expected lifetime upon an absorbed dose, $\tau_{i_{\text{data}}}$ is the lifetime prior to

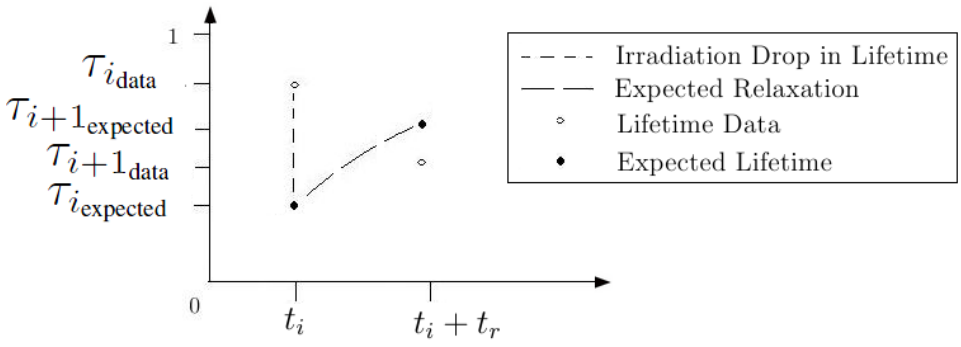

Figure 5.13: Variables used in the calculation of NLCR. Data is collected at time t_i and after a resting period t_r. Some recovery between measurements is expected as was observed in the relaxation experiments.

irradiation, ξ is NLCR ($\Delta\tau/D$, where τ is normalized lifetime), and D is dose.

The lifetime recovery between measurements and following dose is given by

$$\tau_{i+1_{\text{expected}}} = 1 - (1 - \tau_{i_{\text{expected}}})e^{-\frac{t_r}{\tau_{sr}}}. \tag{5.8}$$

where $\tau_{i+1_{\text{expected}}}$ is the lifetime after t_r, and t_r is the elapsed time between $\tau_{i+1_{\text{expected}}}$ and $\tau_{i_{\text{data}}}$. Substituting $\tau_{i_{\text{expected}}}$ from equation (5.7) into equation (5.8) gives

$$\tau_{i+1_{\text{expected}}} = 1 - (1 - (\tau_{i_{\text{data}}} + \xi D))e^{-\frac{t_r}{\tau_{sr}}}. \tag{5.9}$$

ξ is determined by finding the value of ξ which minimizes the least squares fit of the data.

Dose Sample Calculation

The total absorbed energy is calculated by first considering linear mass attenuation. The infinitesimal loss in intensity in crossing a small section of width dx is given by

$$dI(x) = -I(x)\rho\mu_m dx, \tag{5.10}$$

where x is the distance into the material as measured from the surface, $dI(x)$ is the infinitesimal change in intensity at x, $I(x)$ is the intensity at x, ρ is the material density, μ_m is the mass attenuation coefficient, and dx is an infinitesimal change in x.

By integrating from the surface, the intensity at x is given by

$$I(x) = I_\circ e^{-\rho\mu_m x}, \tag{5.11}$$

where $I_\circ$ is incident intensity.

The energy available for energy attenuation at x for photon energy E_p is given by

$$E(E_p, x) = E_p \frac{I(x)}{I_\circ} A\Psi(E_p) \tag{5.12}$$

where the product $A\Psi(E_p)$ gives the number of incident photons at an energy of E_p for a surface area A, and $I(x)/I_\circ$ is the fraction of non-mass attenuated photons at x which are available for energy attenuation.

Energy attenuation is linear and given by

$$\mathrm{d}E = E(E_p, x)\rho\mu_e \mathrm{d}x, \tag{5.13}$$

where μ_e is the energy attenuation coefficient.

By combining equations (5.11) to (5.13), the ideal amount of absorbed energy in the ion chamber is given by the expression

$$\Delta E = \int_0^D \int_0^\infty \rho_{\text{air}}\mu_{e_{\text{air}}} E\, A\Psi\,(E)\ \mathrm{e}^{-\mu_{m_{\text{air}}}\rho_{\text{air}}x}\, dEdx = 9.68 \times 10^6 \text{ keV}. \tag{5.14}$$

where ΔE is the absorbed energy in the ion chamber, E is the photon energy, $\mu_{m_{\text{air}}}$ is the mass attenuation coefficient of air, and $\mu_{e_{\text{air}}}$ is the energy absorption coefficient of air. D is the width of the ion chamber. The range of energy integration is for the full spectrum of a W anode operating at 75 kVp.

Energy is absorbed within the chamber and charge Q_{ideal} is generated. Q_{ideal} represents the expected generated charge. The charge that is generated is given by

$$Q_{\text{ideal}} = \frac{10^3 \Delta E_\circ e}{W_{\text{air}}}, \tag{5.15}$$

where e is the elementary charge and W_{air} is the ion pair formation energy for air.

The measured charge, Q_{measured}, as a function of exposure $R_\circ$ follows directly from the definition of the unit Roentgen

$$Q_{\text{measured}}(R_o) = R_\circ V \rho_{\text{air}} 2.58 \times 10^{-7} \text{ C/g}, \tag{5.16}$$

where V is the volume of the ion chamber.

The x-ray fluence calibration factor Norm($R_\circ$) is

$$\mathrm{Norm}(R_o) = \frac{Q_{\mathrm{measured}}(R_\circ)}{Q_{\mathrm{ideal}}}. \tag{5.17}$$

The measured fluence is

$$\Psi_{\mathrm{measured}} = \mathrm{Norm}(Ro)\Psi_{\mathrm{ideal}} \tag{5.18}$$

Attenuation in air occurs between the ion chamber and the sample. The fluence incident upon the sample is given by

$$\Psi_{\mathrm{sample}} = \Psi_{\mathrm{measured}} e^{-\mu_{\mathrm{air}}\rho_{\mathrm{air}}L_1}, \tag{5.19}$$

where L_1 is the distance between the ion chamber and the selenium sample, and L_1 is in units of cm.

The absorbed energy (J) for a selenium sample with the sample area taken to be the gold contact area makes $A_{\mathrm{Se}} = 0.2$ cm^2, and at an arbitrary thickness of $L_{\mathrm{Se}} = 150$ μm for the purposes of this sample calculation is give by

$$\Delta E_{\mathrm{Se}} = 10^3 e \int_0^{L_{\mathrm{Se}}} \int_0^{\infty} A_{\mathrm{Se}}\rho_{Se}\mu_{e_{Se}} E\Psi_{sample}(E)\, \mathrm{e}^{-\mu_{m_{\mathrm{Se}}}\rho_{\mathrm{Se}}x}\, dEdx. \tag{5.20}$$

The distribution of the absorbed energy accross the sample thicknes is given by

$$\Delta E_{1_{\mathrm{Se}}} = 10^3 e \int_0^{\infty} A_{\mathrm{Se}}\rho_{\mathrm{Se}}\mu_{e\ \mathrm{Se}} E\Psi_{sample}(E)\, \mathrm{e}^{-\mu_{m_{Se}}\rho_{\mathrm{Se}}x}\, dx. \tag{5.21}$$

The deposited dose in the selenium sample (D_{Se}) in units of Gy is given by

$$D_{\mathrm{Se}}(Ro) = \frac{\Delta E_{\mathrm{Se}}(R_\circ)}{10^{-3} A_{\mathrm{Se}} D_{\mathrm{Se}}\rho_{\mathrm{Se}}}. \tag{5.22}$$

An energy deposition profile is provided in Figure 5.14 for an exposure ($R_\circ$) of 1 Roentgen. The energy deposited into the selenium is $\Delta E_{\mathrm{Se}} = 31.12$ μJ and the absorbed dose is $D_{\mathrm{Se}}(R_\circ) = 483$ mGy.

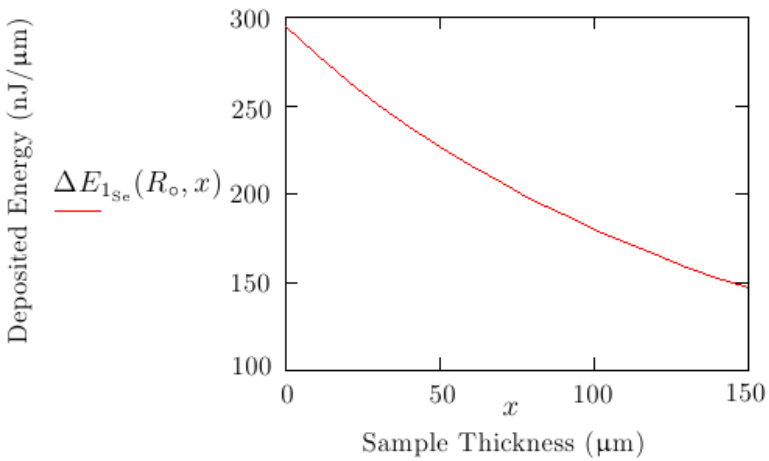

Figure 5.14: Cross sectional energy deposition profile for a 150 µm thick selenium sample exposed to 1 Roentgen from an x-ray beam operating at 75 kVp and 15 mA.

5.2.3 Results

Upon exposure to x-rays, the electron lifetime decreases. The decrease in normalized lifetime is almost linearly proportional to the absorbed dose as seen in Figure 5.15 for a typical sample.

The NLCR experimental results at room temperature are provided in Table 5.2. The NLCR experimental results at 35 °C are provided in Table 5.3. Bar graphs for NLCR experimental results at room temperature and at 35 °C are provided in Figures 5.16 and 5.17 respectively. The irradiation and recovery experiment plots are provided in Appendix A for individual samples.

Figure 5.16 is a bar graph representation of NLCR data at 21 °C. NLCR is reported for each sample and at both fields. The standard deviation is shown in an error bar representation. NLCR is observed to increase with field. The trend is observed in four of five alloys with no error bar overlap in two of the four alloys. The average increase in NLCR due to the application of a field is 105.9%. An exception is observed containing an error bar overlap for the sample C1 in which case there is a decrease of 28%.

Measurements were also carried out at 35 °C. NLCR was observed to increase with field at high temperature. This occurred in three of five alloys in which there was no error bar

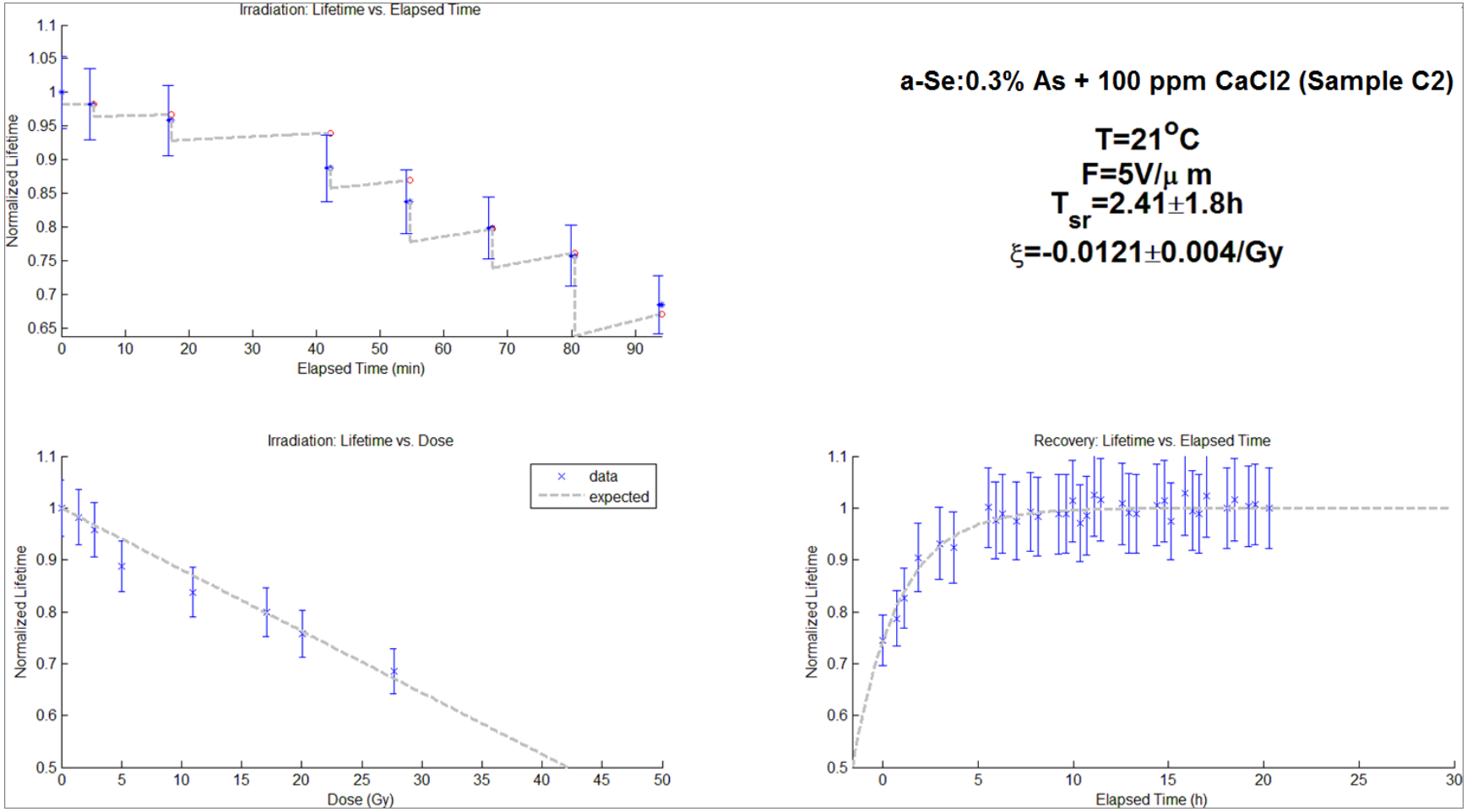

Figure 5.15: Plots of the irradiation and recovery experiment for run C2 at a temperature of 21 °C and at a field of 5 V/μm .

Table 5.2: The normalized lifetime change rate (NLCR) and the structural relaxation time (τ_{sr}) of the thesis samples at room temperature and at a field of 0 V/μm and 5 V/μm .

Sample	Field F (V/μm)	Normalized Lifetime Change Rate NLCR (%/Gy)	Standard Deviation σ_{NLCR} (%/Gy)	Structural Relaxation Time τ_{sr} (h)	Standard Deviation $\sigma_{\tau_{sr}}$ (h)
pure a-Se (Sample A)	0	0.72	0.22	2.95	0.6
	5	1.02	0.38	3.08	1
a-Se:0.2% As (Sample B1)	0	0.57	0.17	3.88	0.6
	5	1.42	0.68	4.48	4
a-Se:0.2% As (Sample B2)	0	1.17	0.17	3.36	1.8
	5	1.7	0.26	4.62	1.4
a-Se:0.2% As + 2 ppm Cl (Sample C1)	0	1.82	0.57	1.50	0.6
	5	1.31	0.24	2.03	0.4
a-Se:0.3% As + 100 ppm $CaCl_2$ (Sample C2)	0	0.42	0.12	1.17	0.6
	5	1.21	0.4	2.41	1.8

Table 5.3: The normalized lifetime change rate (NLCR) and the structural relaxation time (τ_{sr}) of the thesis samples at a temperature of 35 °C and at a field of 0 V/μm and 5 V/μm .

Sample	Field F (V/μm)	Normalized Lifetime Change Rate NLCR (%/Gy)	Standard Deviation σ_{NLCR} (%/Gy)	Structural Relaxation Time τ_{sr} (min)	Standard Deviation $\sigma_{\tau_{sr}}$ (min)
pure a-Se (Sample A)	0	30.1	4.23	7.09	2.6
	5	11.3	3.43	6.05	3.2
a-Se:0.2% As (Sample B1)	0	7.79	0.96	7.14	3.4
	5	31.6	5.2	5.59	5.1
a-Se:0.2% As (Sample B2)	0	20.1	0.37	5.92	1.4
	5	14.8	0.05	10.30	1.4
a-Se:0.2% As + 2 ppm Cl (Sample C1)	0	13.2	1.75	8.20	3.7
	5	35.4	0.41	6.70	2.3
a-Se:0.3% As + 100 ppm $CaCl_2$ (Sample C2)	0	16.6	1.9	9.51	3.7
	5	38.5	1.03	6.24	4.7

overlap. The average increase was 201.2%. An exception was observed for samples B2 and A where there was an average decrease of 26%. Experimental error may likely be the cause of the discrepancy as there was no error bar overlap indicating the error in the IFTOF measurement technique itself did not account for the discrepancy.

In the least squares fitting algorithm which calculated NLCR, any expected normalized lifetime value which was negative, that was reached in the fitting procedure, was given the value of zero because a negative lifetime value does not make physical sense. Negative lifetime values were typically reached for the the value of the expected lifetime upon an absorbed dose. These negative lifetime values would typically occur for expected lifetimes occurring nearing the end of the irradiation experiment in which case the absorbed dose was at a relative maximum and the measured lifetime prior to irradiation was at a relative minimum. By reaching an expected lifetime value which is negative, it may suggested that there is a maximum number of induced deep traps which can occur at a given sample temperature.

Upon an absorbed dose and prior to any lifetime recovery, a negative expected lifetime value was reached while performing the NLCR fitting algorithm for sample B2 at $0\,\mathrm{V/\mu m}$ and $5\,\mathrm{V/\mu m}$ at room temperature, for sample C1 at $5\,\mathrm{V/\mu m}$ at room temperature, and for sample C2 at $5\,\mathrm{V/\mu m}$ at room temperature. This may suggest that the calculated NLCR value at room temperature and high field for samples B2, C1, and C2 is larger than the actual value.

A greater field effect was observed at $35\,^{\circ}\mathrm{C}$. At this temperature, the change was 201% whereas at room temperature, the change was 106%.

The average minimum normalized lifetime ($\tau_{i_{\mathrm{expected}}}$ in equation 5.9) varied with temperature but not with the field. At room temperature, the normalized minimum lifetime values were 0.50 and 0.56 at low and high fields respectively. At high temperature the values were 0.19 and 0.15. When the average minimum lifetime was placed in ascending order with respect to alloy composition, the order did not change with the temperature or the field. These trends may suggest consistency in the applied experimental method.

Two samples of equal nominal compositions, B2 and B1, displayed vastly different min-

imum lifetime. For example, at room temperature and $5\,\mathrm{V/\mu m}$, the normalized minimum lifetime values were 0.2 and 0.6. In the discussion, the two samples may need to be considered as two separate alloys as it is well known that the properties of a-Se can depend on the fabrication method and on the source of a-Se.

It is clear from Figures 5.16 - 5.18 that the lifetime decrease is more significant at higher temperatures. The change of electron lifetime per unit of absorbed dose is less than 2 %/Gy at room temperature. At 35 °C it is less than 30 %/Gy. The average values of NLCR at room temperature and 35 °C were 1.14 ± 0.1 %/Gy and 24.0 ± 0.8 %/Gy respectively.

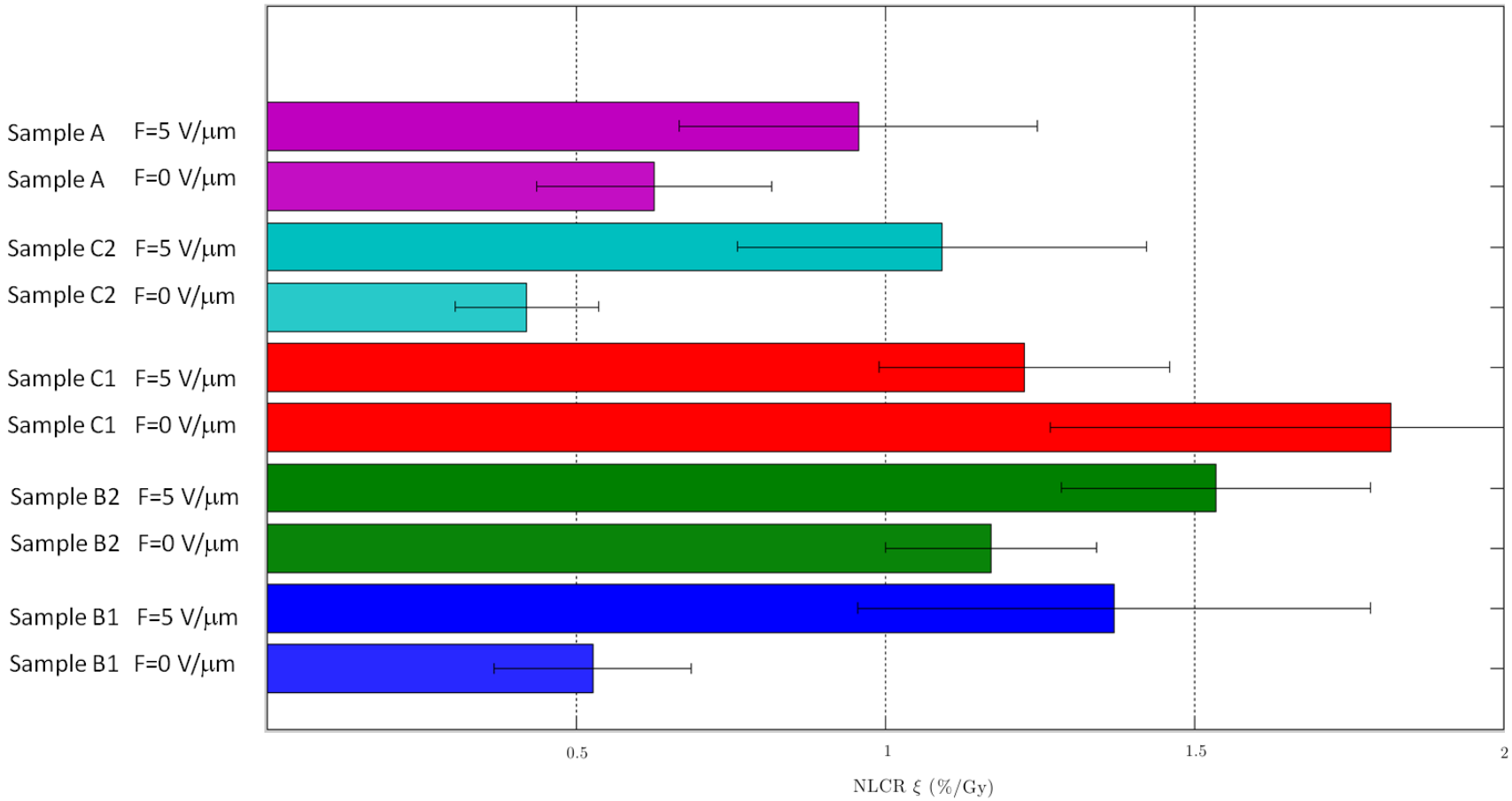

Figure 5.16: Bar graph of NLCR at room temperature for various alloys. NLCR is indicated for a field of 0 V/μm and 5 V/μm .

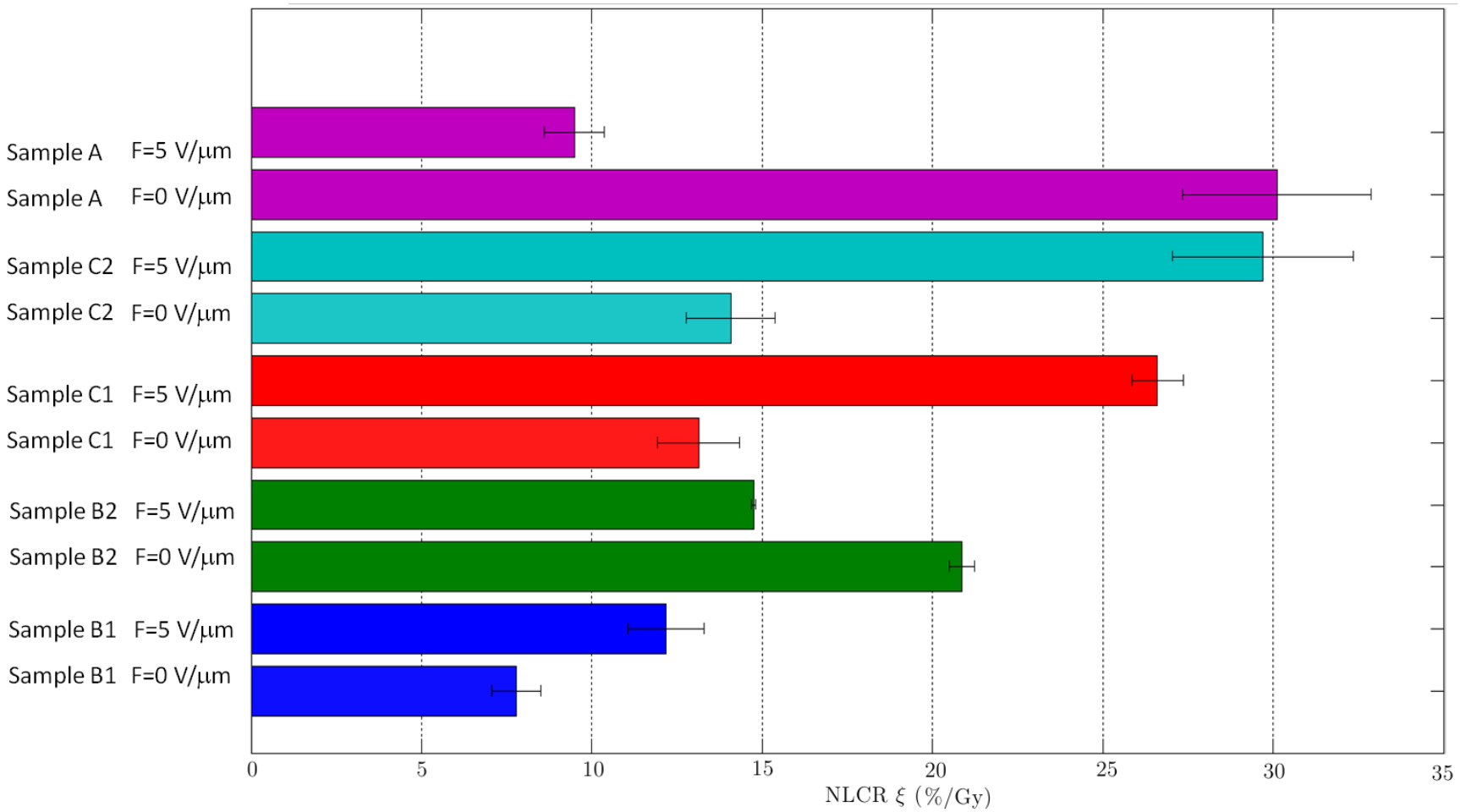

Figure 5.17: Bar graph of NLCR at 35°C for various alloys. NLCR is indicated for a field of 0 V/µm and 5 V/µm .

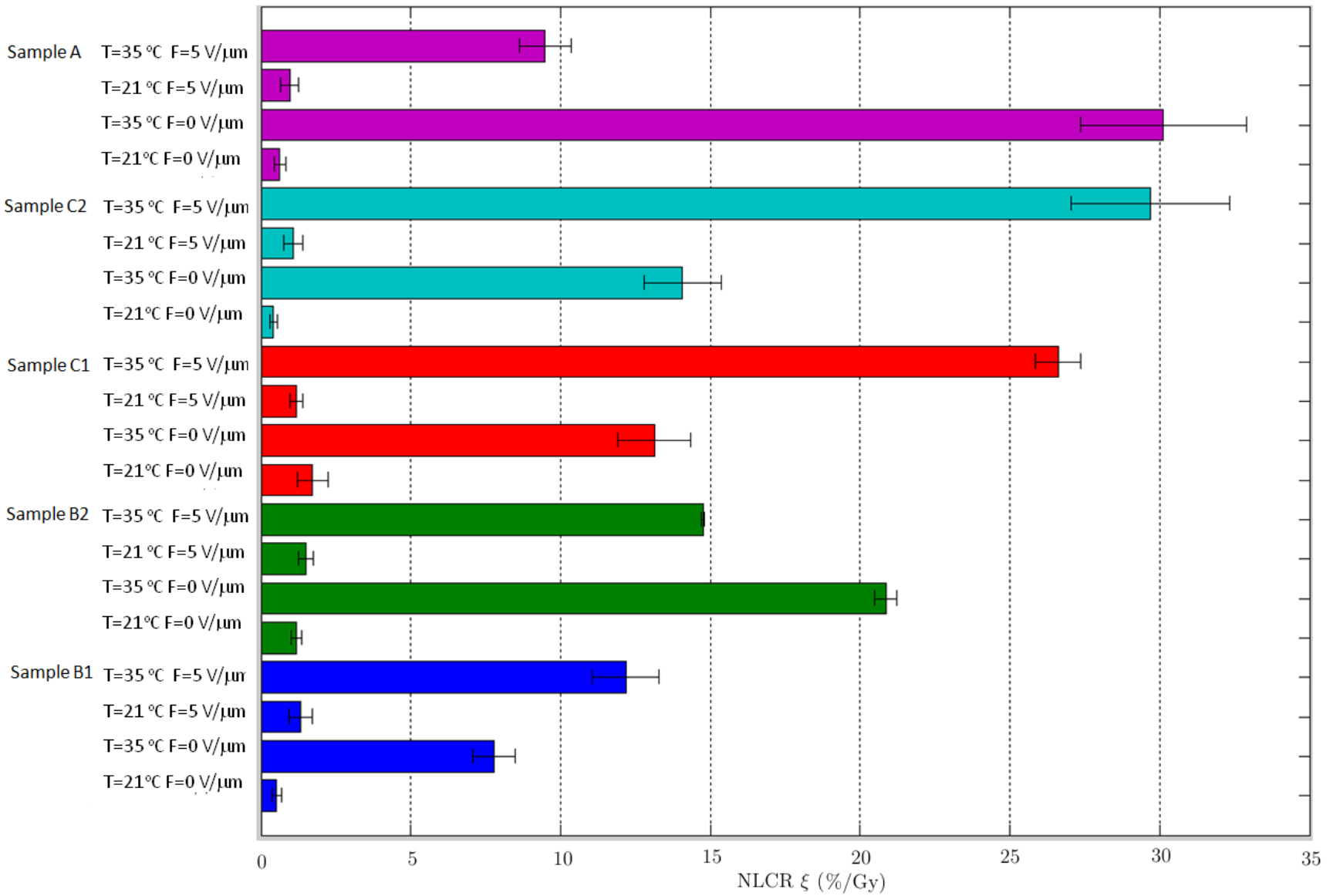

Figure 5.18: Bar graph of NLCR at 21 °C and 35 °C for various alloys. NLCR is indicated for a field of 0 V/µm and 5 V/µm. For each alloy, a sample temperature of 21 °C is indicated by NLCR < 0.05 with a sample temperature 35 °C indicated by NLCR > 0.05.

5.3 Structural Relaxation Time

5.3.1 Background

In the relaxation experiment, the lifetime was observed to relax in an Arrhenius fashion which suggests a thermally activated process. The definition of lifetime is given by $\tau = 1/(CN)$, where τ is the lifetime, C is the capture coefficient, and N is the total electron deep trap density. A change in deep trap density is therefore clearly related to a change in lifetime. If the relaxation was linearly activated, an exponential recovery of lifetime to its equilibrium value following x-ray irradiation would be suggested by

$$-d\tau(t) = \frac{1}{\tau_{sr}}\tau(t)dt, \tag{5.23}$$

where $\tau(t)$ is the lifetime and τ_{sr} is the structural relaxation time. Trapping rate or probability is given by

$$\frac{1}{\tau} = \frac{1}{\tau_\circ} + \frac{1}{\tau_x} = C_{t_\circ}N_{t_\circ} + C_{t_x}N_{t_x}, \tag{5.24}$$

where $\tau_\circ$ is the resting lifetime, τ_x is the x-ray induced lifetime. By multiplying both sides by $\tau_\circ$ and by letting $\tau_n = \tau/\tau_\circ$ be the normalized lifetime gives

$$(\tau_n^{-1} - 1) = m(N_{t_x})^n, \tag{5.25}$$

where m is a constant. The relation $D \propto N_{tx}$ can be tested by fitting to experimental data

$$(\tau_n^{-1} - 1) = m_2 D^n, \tag{5.26}$$

where D is dose, and m_2 incorporates the constant of proportionality. Using linear regression n can be found using experimental data using

$$log(\tau_n^{-1} - 1) = nlog(D) + log(m). \tag{5.27}$$

If linear then $n = 1$. A linear relation was observed using data from sample C2 at room temperature and field of $5\,\mathrm{V/\mu m}$ where $n = 1.1$.

It is however possible that the process is not linearly activated. A decrease in the lifetime measurement could result from the recombination of charge carriers from the photocurrent with trapped charge in the bulk and not from a change in the deep trap concentration itself.

The thesis experiments do not seem to suggest that the lifetime decreases from charge recombination between the photocurrent and trapped charge in the bulk. X-ray irradiation increases the concentrations of C_1^0. An increase in this concentration would reduce an electron photocurrent via charge recombination. The C term refers to the concentration of the IVAP defect state. An increase in this concentration is achieved with x-ray irradiation by $C_1^- + h_x^+ \rightarrow C_1^0$ [86]. The subscript x refers to an x-ray induced term. During the IFTOF lifetime measurement, electron charge carriers in the charge packet are reduced by $C_1^0 + e_i^- \rightarrow C_1^-$ where e_i^- is a photocurrent charge carrier. In the recovery experiment, the initial drop in lifetime could be achieved by the above process as a typical sample was exposed to x-ray irradiation for at least 20 s. This possibility does not explain the long recovery time. Hole detrapping time in a rested a-Se sample is on the order of several minutes [87] while structural relaxation was observed at room temperature to occur on the order of several hours. This possibility is therefore unlikely. The formation of x-ray induced traps (N_{t_x}) is therefore a possibility.

5.3.2 Measurement Technique

Experimental Sequence

In the relaxation experiment, an immediate decrease in lifetime was observed upon irradiation. The decreased lifetime corresponds to an increase in the number of deep traps which relax over time to their equilibrium value.

Constant PID temperature control to within ± 1 °C was maintained during the experimental sequence shown in Figure 5.19. A large dose was delivered under an applied field which was followed by a lifetime measurement five minutes later. A lifetime measurement was taken every five minutes until the sample was fully recovered. Prior to the experiment, the resting lifetime was measured following 48 h of relaxation.

A rest interval was observed between IFTOF measurements in order to reduce the effects of carrier trapping. Measurements were taken every five minutes. During the five minute interval some detrapping occurred. A shorter rest interval in the relaxation experiment would

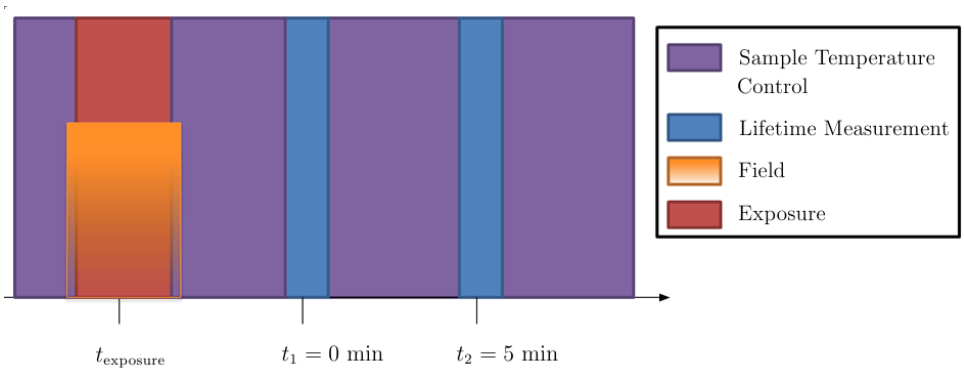

Figure 5.19: Recovery experiment sequence diagram detailing temperature control, exposure, measurement and sample exposure.

result in an increase in the trapped photoinjected carriers. A longer rest interval may not adequately capture the recovery.

A dataset of lifetime vs. elapsed time is recorded in the recovery experiment. Elapsed time refers to the time elapsed following the first lifetime measurement. A dose large enough for a significant enough change in normalized lifetime was delivered at the start of the experiment. This was done to be able to record as many datapoints as possible and to provide the best measure of relaxation. It allowed for recovery behaviour to be observed at low lifetime values. A plot of a typical recovery experiment is shown in Figure 5.20. Lifetime is plotted on the vertical axis while elapsed time is plotted on the horizontal axis. Figure 5.20 shows that lifetime recovery is exponential within experimental error as is indicated by the error bars.

Calculation Method of the Structural Recovery Time

It was observed that recovery followed a first order rate equation, which implies an exponential recovery. The structural relaxation time is determined by performing a non-linear least squares fit

$$\tau_t = 1 - (1 - \tau_o)e^{-\frac{t}{\tau_{sr}}}, \tag{5.28}$$

where τ_t is normalized lifetime at time t, τ_o is normalized lifetime at $t = 0$, t is elapsed time, and τ_{sr} is structural relaxation time.

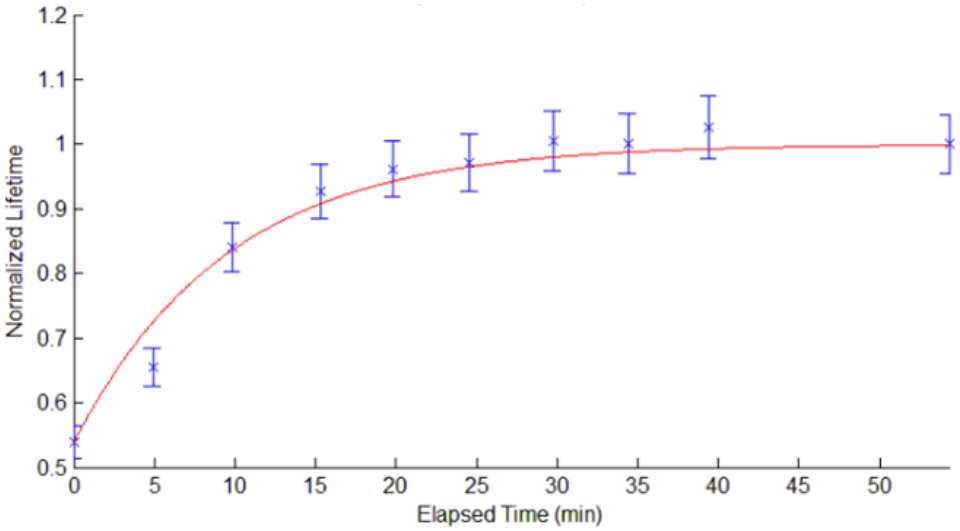

Figure 5.20: A sample of a lifetime recovery experiment with lifetime relaxing to its equilibrium value.

The calculation of the fit parameter error has two parts. The first part fits N datapoints to m parameters with $M - m - 1$ degrees of freedom. The second part is a variation of $\Delta\chi^2$ with one of the m parameters, for example β in Equation (5.29), about the minimum of χ^2, with 1 degree of freedom.

The exponential recovery fit equation with two fit parameters τ_{sr} and β is shown in Equation (5.29)

$$\tau_{\text{fit}} = \tau_\infty - (\tau_o - \tau_\infty)e^{(t/\tau_{sr})^\beta} \tag{5.29}$$

where τ_{sr} is the structural relaxation time, β is a stretched exponential parameter, τ_∞ resting lifetime, $\tau_\circ$ lifetime at the start of the experiment, and τ_{fit} is the fitted lifetime as a result of a chosen relaxation parameter determined from the experimental fit.

Equation (5.30) integrates the χ^2 probability distribution function, having υ degrees of freedom, and describes the probability that a random set of datapoints drawn from the parent distribution would yield a value of χ^2 equal or greater than the fitted value.

$$P_\chi(\chi^2;\upsilon) = \int_{\chi^2}^{\infty} \frac{(x^2)^{1/2(\upsilon-2)}e^{-x^2/2}}{2^{\upsilon/2}\Gamma(\upsilon/2)}\,\mathrm{d}x^2. \tag{5.30}$$

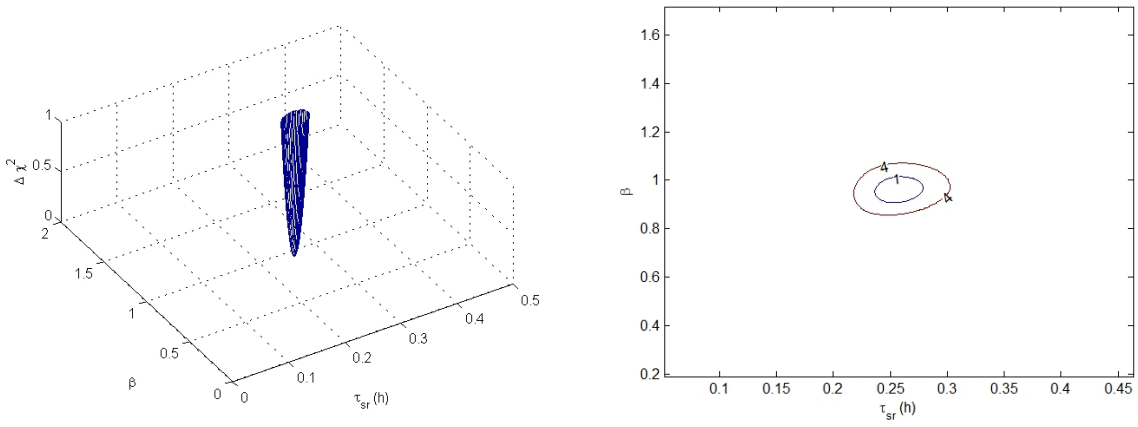

Figure 5.21: Curved surface (left) and contour (right) of $\Delta\chi^2$ with standard deviation of fit parameters β and τ_{sr} given by $\Delta\chi^2 = 1$ for a typical sample.

The outer limits of τ_{sr} indicate the one standard deviation limits of τ_{sr} that includes 68.3% of the probability. The outer limits of β indicate the one standard deviation limits of β. The outer limits of the $\Delta\chi^2 = 4$ contour indicate the two standard deviation limits.

Figure 5.21 is a curved surface and contour plot of $\Delta\chi^2 = 1$ about the χ^2 minimum. The standard deviation of a fit parameter is given by the largest absolute value difference of the parameter between the maximum or minimum value of the parameter at $\Delta\chi^2 = 1$ and at the local χ^2 minimum. Figure 5.22 shows a sample plot of $\Delta\chi^2$ versus variation of the parameter m about the minimum. m is NLCR in this case. It can be seen from Figure 5.22 that by allowing both β and τ_{sr} to vary, a local χ^2 minimum is obtained for a typical thesis sample for a β value very close to $\beta = 1$. β has therefore been set to $\beta = 1$ for all τ_{sr} calculations.

5.3.3 Results

Structural relaxation, also known as short-range ordering, was observed in the recovery experiment. The relaxation occurs following x-ray dose. Upon exposure, the lifetime is observed to recover to its resting value. The lifetime was observed to follow an exponential recovery, with the recovery parameter given as the structural relaxation time (SRT) or τ_{sr}. The sample recovery rate is determined from τ_{sr}. The rate is expected to decreases with temperature in an Arrhenius fashion. SRT at room and high temperature and at both fields

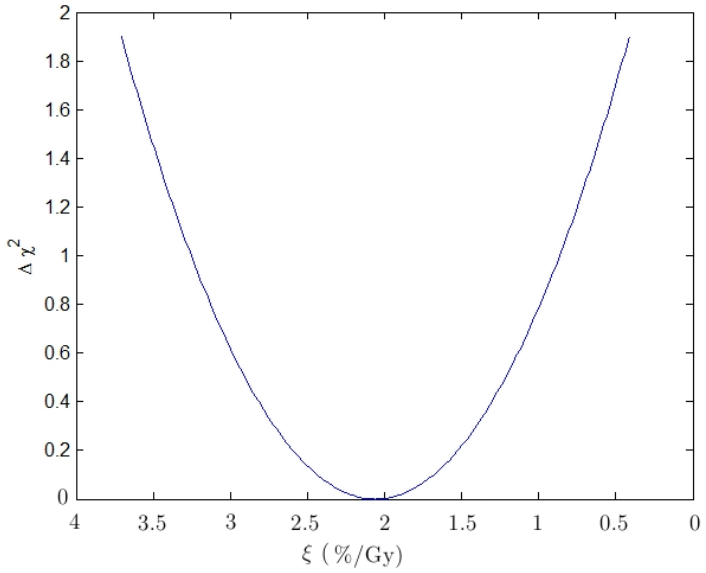

Figure 5.22: $\Delta\chi^2$ versus NLCR (ξ) about the minimum.

is shown in figure and bar graph form for all samples. The listed figures and tables are: Figures 5.23 and 5.26, and Tables 5.2 and 5.3.

Temperature Dependence

SRT at room temperature is shown in Figure 5.23. The standard deviation is shown using error bars. SRT was observed to increase with field in all alloys with error bar overlap occuring for all but two alloys. The average increase in SRT with field was 40% at room temperature.

SRT at 35 °C is shown in Figure 5.26. No average change in SRT was observed with field. An increase was observed in only two alloys. Error bars overlapped in all but one sample in which case an increase was observed. The average increase was −3.0%. The high field discrepancy may be a result of a limited number of data points resulting in a larger error.

Temperature increases the internal energy and therefore the rate of recovery. The average τ_{sr} decreased from 2.95 ± 0.5 h to 7.27 ± 0.9 min as the temperature was varied from room temperature to 35 °C. The ranges in τ_{sr} at room temperature and 35 °C were 2 - 4 hrs and 6 - 10 mins respectively. Much longer recovery was observed at low temperature as shown in Figure 5.27.

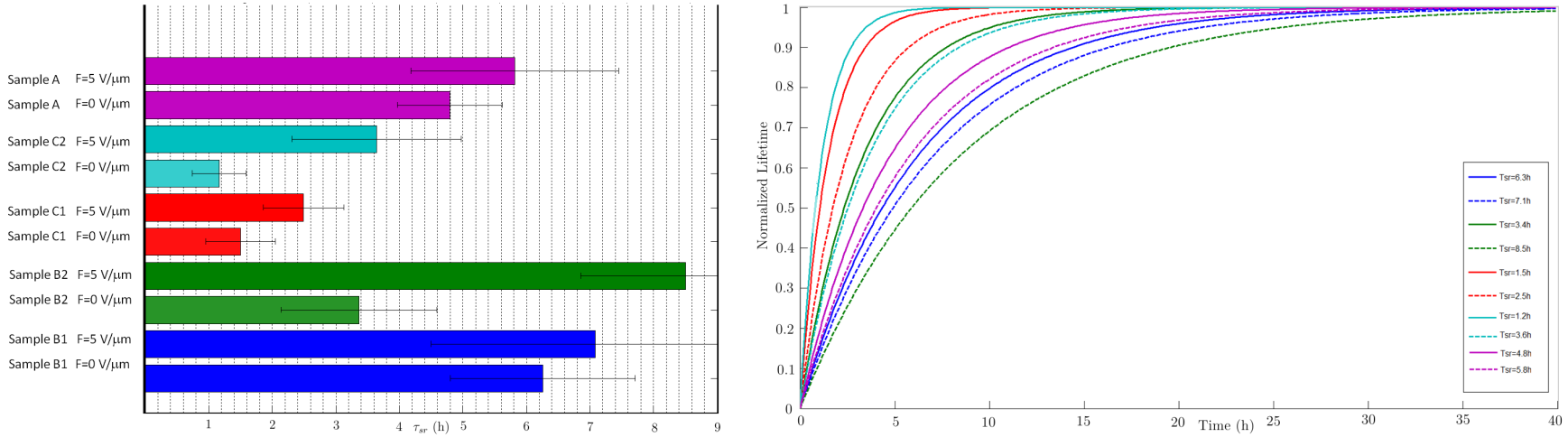

Figure 5.23: Structural recovery time at 21°C for various samples and for fields of 0 V/µm and 5 V/µm. The same experimental data is represented in both bar graph (left) and plot (right). Figure to right is a plot of normalized lifetime versus time elapsed after irradiation. Figure to left is a bar graph showing for various samples the strucutral recovery time.

The average τ_{sr} increased by 40% with field, an increase from 0 V/µm to 5 V/µm , at room temperature. There was however no change (−3.0%) with field at 35 °C.

The average τ_{sr} is compared to typical values seen in annealing [2] in Table 5.5. Recovery from irradiation seems to be significantly faster than for those samples that have been subject to a thermal history i.e. heated to a temperature above T_g and brought down to room temperature.

Figure 5.24 shows a semi-logarithmic plot of τ_{sr} vs. the reciprocal of temperature. The activation energy was roughly 1.4 eV, which increased by 32% with the field. Activation energies were calculated for all alloys and at both fields as shown in Figures 5.24 and 5.25. A list of activation energies is provided in Table 5.4.

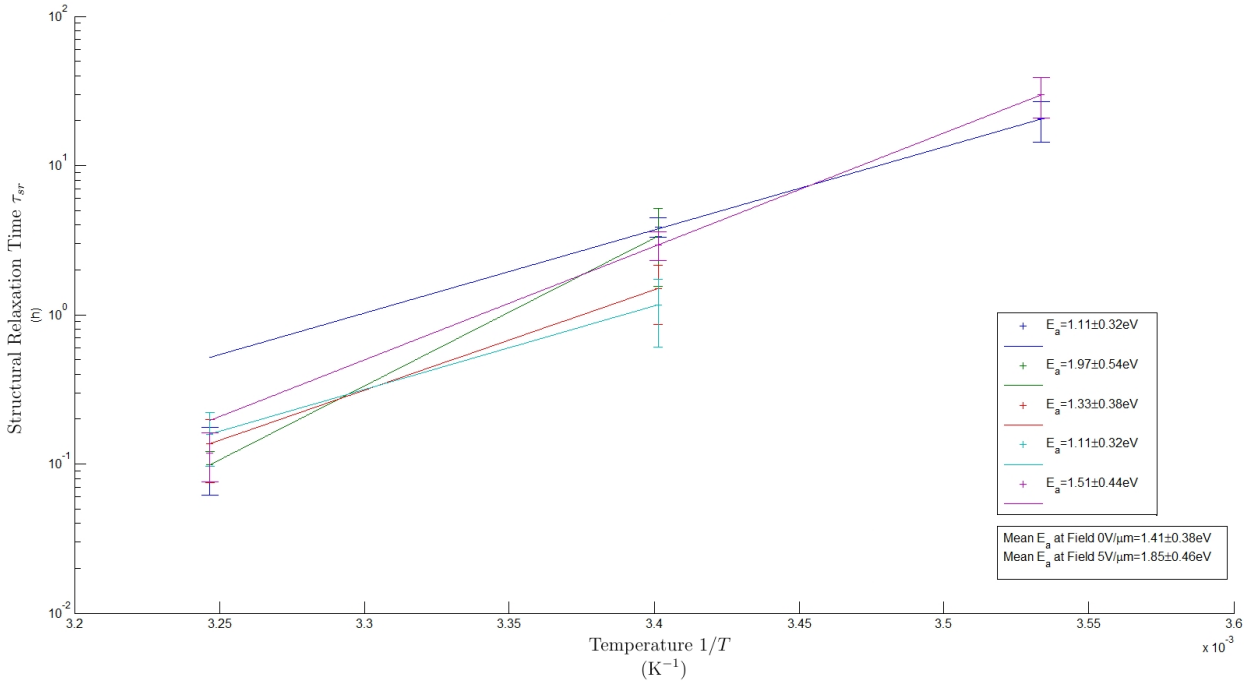

Figure 5.24: Semi-logarithmic plot of SRT vs. the reciprocal of temperature ($1/T$) at a field of 0 V/µm for a-Se and its alloys. The corresponding thermal activation energy E_a for each alloy is reported in the legend.

Those a-Se films with a higher activation energy where observed to recover more slowly. The average activation energy at a field of 0 V/µm was roughly 1.4 eV which increased by 32% at 5 V/µm.

Table 5.4: Thermal activation energy E_a in eV for fields of 0 V/μm and 5 V/μm and for various sample compositions. For all but a-Se E_a was derived from τ_{sr} at 21°C and 35°C . For a-Se, E_a was derived from τ_{sr} at 10 °C , 21 °C, and 35 °C.

Activation Energy at F=0 V/μm (eV)	Sample	Activation Energy at F=5 V/μm (eV)	Sample
1.11 ± 0.32	B1	1.62 ± 0.45	C1
1.11 ± 0.31	C2	1.75 ± 0.51	C2
1.33 ± 0.38	C1	1.83 ± 0.54	B2
1.41 ± 0.38	A	1.85 ± 0.46	A
1.97 ± 0.54	B2	2.16 ± 0.63	B1

Table 5.5: Average structural relaxation times for a-Se at 10 °C, 21 °C and 35 °C and a-Se:0.2 % As at 21 °C. The reported values are averaged across all alloys. The comparable annealing time is from Allen [2].

Temperature T (°C)	Average Structural Relaxation Time τ_{sr}	Alloy	Comment
10	25 h	all	
21	2.5 h	a-Se	7.7 h annealing [2]
	3.5 h	a-Se:0.2 % As	16.9 h annealing [2]
35	7.3 min	all	

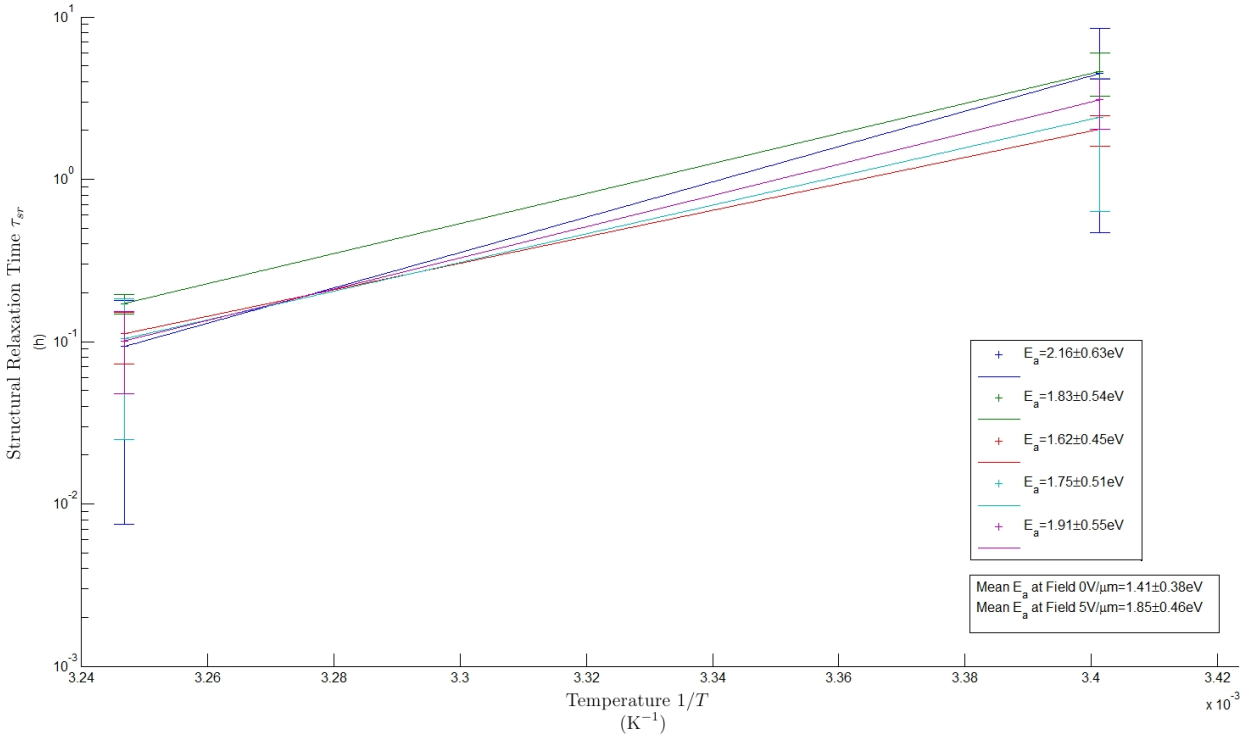

Figure 5.25: Semilogarithmic plot of SRT vs. the reciprocal of temperature ($1/T$) at a field of $5\,\mathrm{V/\mu m}$ for a-Se and its alloys. The corresponding thermal activation energy E_a for each alloy is indicated in the legend.

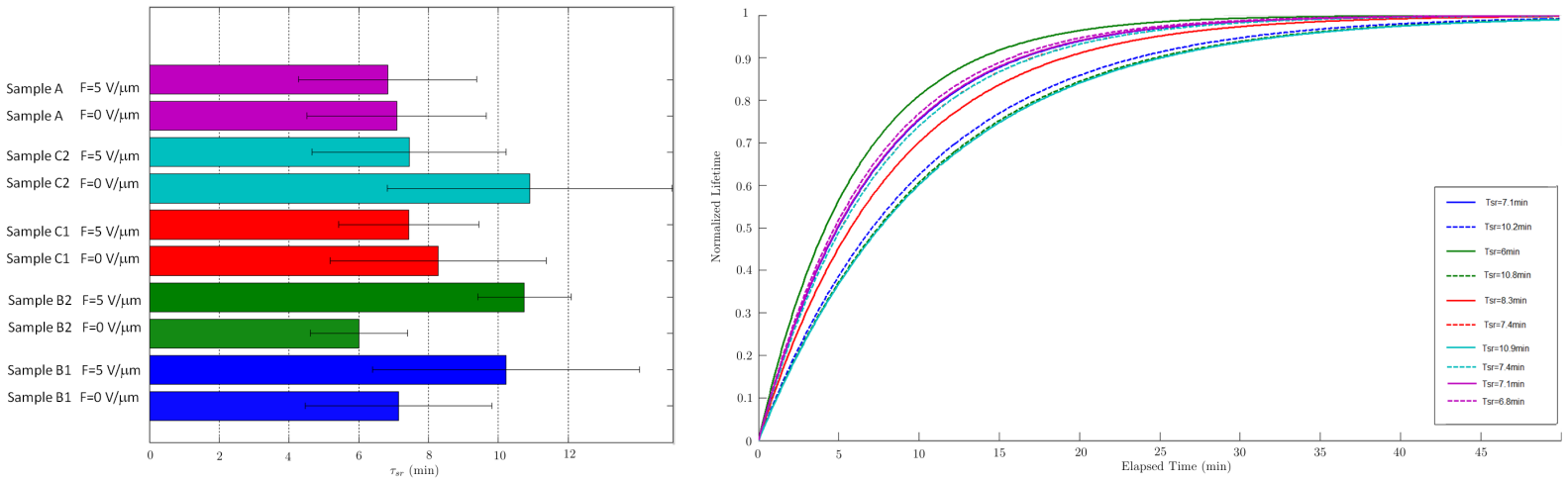

Figure 5.26: Structural recovery time at 35 °C for various samples and for fields of 0 V/μm and 5 V/μm. The same data is represented in both bar graph and plot. The figure to the right is a plot of normalized lifetime versus time elapsed after irradiation. The figure to left is a bar graph showing for various samples the structural recovery time.

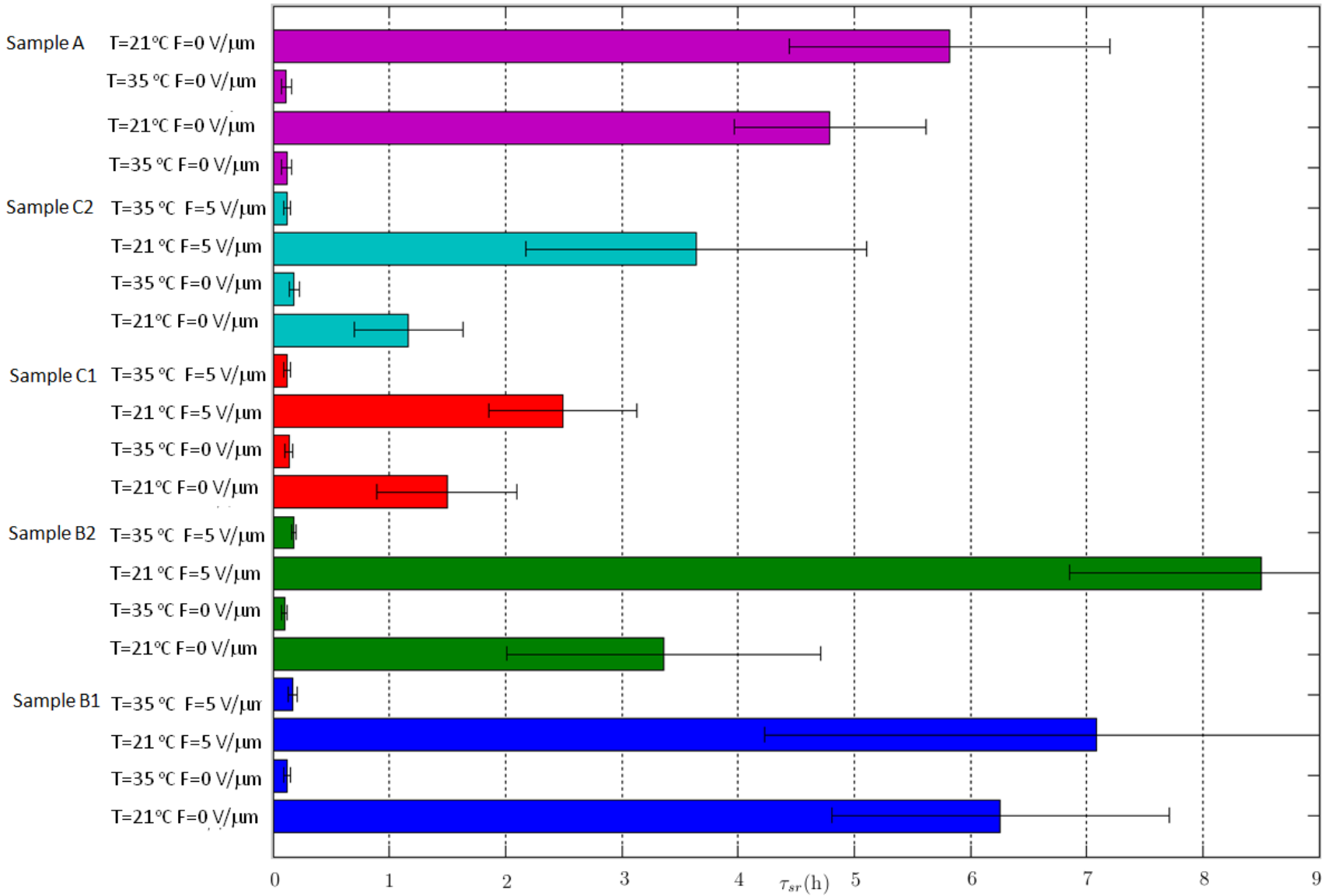

Figure 5.27: The structural relaxation time for various samples at both 21 °C and 35 °C and at fields of 0 V/µm and 5 V/µm. For a given sample the largest two structural relaxation times refer to the 21 °C experiment.

5.4 Summary

This chapter covered the IFTOF technique and a method for calculating the electron lifetime. It also covered a method of measuring and calculating the NLCR, and the SRT. In the IFTOF discussion section, the IFTOF measurement sequence was outlined. Equations used in calculating the electron lifetime were derived, and the calculation procedure described. In the NLCR discussion section, the irradiation experimental sequence was outlined. A sample calculation was performed for a given deposited dose. A sample energy deposition profile was also plotted. NLCR calculations were described using the SRT obtained from the recovery experiments. In the SRT discussion section, the recovery experiment was outlined. An experimental sequence was described and equations used in calculating SRT were derived.

An almost linear relation was observed between lifetime and absorbed dose. The two are related by the NLCR term. The temperature and field dependence of NLCR was measured for various samples. Theory which is based on a light-induced phenomena and which is related to a decrease in lifetime was presented. The results were extended to an imaging application in digital mammography and a comment on the impact on device performance was made.

In the recovery experiment, the nature of the recovery was suggested based on the best fit mathematical expression to the recovery data. The recovery was measured at various fields and temperatures for various samples. The field and temperature dependence were determined and reasons given for any discrepancies. The average recovery values were reported. The limitations of the experimental method on determining the exact mechanism of the structural changes involved in relaxation was mentioned. The possibility of photocurrent charge recombination with trapped charges in the bulk was investigated. A simple and general thermodynamic explanation for the temperature dependence of thermal relaxation was given.

6. Summary and Conclusion

The dependence of electron transport in a-Se x-ray photoconductors on absorbed dose and temperature was examined in this work. Electron transport in vacuum deposited a-Se films has been investigated by Interrupted-Field Time-of-Flight (IFTOF) transient photoconductivity experiments to examine the effect of sample temperature (T) and applied electric field (F) on x-ray induced changes in the electron lifetime, τ_e. These measurements are important in characterizing the charge collection efficiency of a-Se based x-ray detectors, and its dependence on x-ray exposure and temperature.

Electron transport dependence with alloying was not considered. One pure a-Se and four a-Se alloys doped with either As, Cl, or $CaCl_2$ were prepared by conventional vacuum deposition. The sample temperature was increased from 21 °C (room temperature) to 35 °C (high temperature) and the field was varied from 0 V/μm (low field) to 5 V/μm (high field).

The IFTOF technique was used to probe the change in carrier concentration in the conduction band and as a result to determine the average time between trapping events. The lifetime is a measure of the deep trap concentrations in the bandgap. A single lifetime measurement using the IFTOF technique cannot be used to determine the deep trap density of states function. This means that the deep trap density of states cannot be directly determined. It should also be noted that the IFTOF technique measures the average lifetime during the interruption time. Change in the total number of deep trap states can however be inferred from a change observed in the measured lifetime. IFTOF measurements indicate that x-ray exposure induces an increase in the density of deep trap states. In the relaxation experiment, it was observed that there is a reduction in the density of deep trap states as a result of thermally activated structural relaxation.

6.1 X-ray Induced Change in Lifetime

It has been observed that the lifetime decreases upon irradiation, which implies the total deep trap density of states increases. The increase in the total number of deep traps was larger when the temperature is elevated or when the irradiation occurs under an applied field.

Upon exposure to x-rays, the electron lifetime decreases. The decrease in normalized lifetime is almost linearly proportional to the absorbed dose. The rate of change is expressed as the normalized lifetime change rate (NLCR). The NLCR is less than 2 %/Gy at room temperature. At 35 °C it is less than 30 %/Gy. The average values were 1.1 ± 0.1 %/Gy and 24.0 ± 0.8 %/Gy respectively. The lifetime decrease is more significant at higher temperatures and field. The NLCR increased with field by 79% on average. At high temperature the increase was 108% on average. The field effect calculation has a large error associated with the value of NLCR which makes the effect unlikely.

Photodarkening, a known photoinduced effect resulting in deep trap creation was noted. X-ray radiation induces structural changes in a-Se. A photodarkening model which suggests structural changes by defect creation [81–83]. The creation of defects which act as deep traps would result in the observed reduction in lifetime upon x-ray irradiation. In this model, pairs of threefold (Se_3^+) and onefold (Se_1^-) coordinated sites are induced.

An increase in temperature or applied field resulted may imply that the potential energy barrier to deep trap creation by x-ray induced mechanisms is lowered. Lattice vibrations may behave similarly to an applied field in shifting the lattice and therefore lowering the potential energy barrier which must be overcome in deep trap formation.

6.2 Lifetime Recovery Upon Cessation of X-ray Irradiation

Upon the cessation of x-ray irradiation, the lifetime recovers towards its equilibrium value through a structural relaxation process, and is characterized by a structural relaxation time (SRT). The SRT decreases with temperature in an Arrhenius fashion.

Temperature increases the internal energy and therefore the rate of recovery. The average

τ_{sr} decreased from 3.0 ± 0.5 h at room temperature to 7.3 ± 0.9 min at 35 °C. The ranges in τ_{sr} were 2 - 4 hrs at room temperature and 6 - 10 mins at 35 °C.

The average SRT increased by 40% with an increase in field with no change (-0.3%) at high temperature. The high temperature discrepancy may be a result of a less accurate fit due to a limited number of high temperature data points. The limited number of data points were the result of a faster recovery and a five minute sample rest period between lifetime measurements.

The average thermal activation energy of the recovery process was roughly 1.4 ± 0.4 eV which increased by 32% with field. The average NLCR at low and high fields had overlapping error bars making a field effect unlikely.

Thermally activated relaxation may be explained using a proposed configuration coordinate model [81] which is a result of the aforementioned photodarkening structural model. The mechanisms of the thermal relaxation process which follows photodarkening cannot be made clearer because of subtle structural changes which cannot be experimentally identified [13].

In the relaxation experiment, lifetime was observed to relax in an Arrhenius fashion which suggests a thermally activated process. If the relaxation was linearly or thermally activated, an exponential recovery of lifetime to its equilibrium value following x-ray irradiation would be suggested by $d\tau/dt = \tau/\tau_{sr}$, where τ is lifetime, and τ_{sr} is the structural relaxation time. τ_{sr} is linearly activated. It seems likely that N_d is also linearly activated because a decrease in the measured lifetime is not likely to result from charge carrier recombination between the photocurrent and trapped charge in the bulk.

The thermal activation energy of the recovery process had a higher average value when exposure occurred at a higher applied field. Confidence cannot be placed in this result as there is error bar overlap. Also, an increase in temperature was seen to increase the rate of recovery as the vibrational mean energy at a given vibrational frequency increases with temperature thus increasing the rate of recovery.

A. Experimental Results

Plots of irradiation and recovery experiments at a temperatures of 21°C and 35°C and at fields of 0 V/μm and 5 V/μm are included in this section. Structural relaxation time (T_{sr}) and the normalized lifetime change rate NLCR (ξ) are shown in the figures. T_{sr} has units hours for 21 °C experiments and minutes for 35 °C experiments. T_{sr} is a parameter in exponential relaxation. ξ has units Gy^{-1}. ξ represents the change in normalized lifetime per unit dose where the maximum normalized lifetime has a value of unity. The sample composition is indicated in the top right quadrant of the figures. The data points (blue) and the expected trend lines (gray dashed) are indicated in the plots.

Two plots exist for the irradiation experiment. A normalized lifetime versus elapsed time plot indicates measurement timing. A normalized lifetime versus absorbed dose plot indicates the change in the lifetime with total absorbed dose.

ξ is the slope of the linear regression fit of normalized lifetime versus dose data. The calculation of ξ accounts for the structural recovery between measurements.

A.1 Experiments Performed at a Sample Temperature of 21 °C

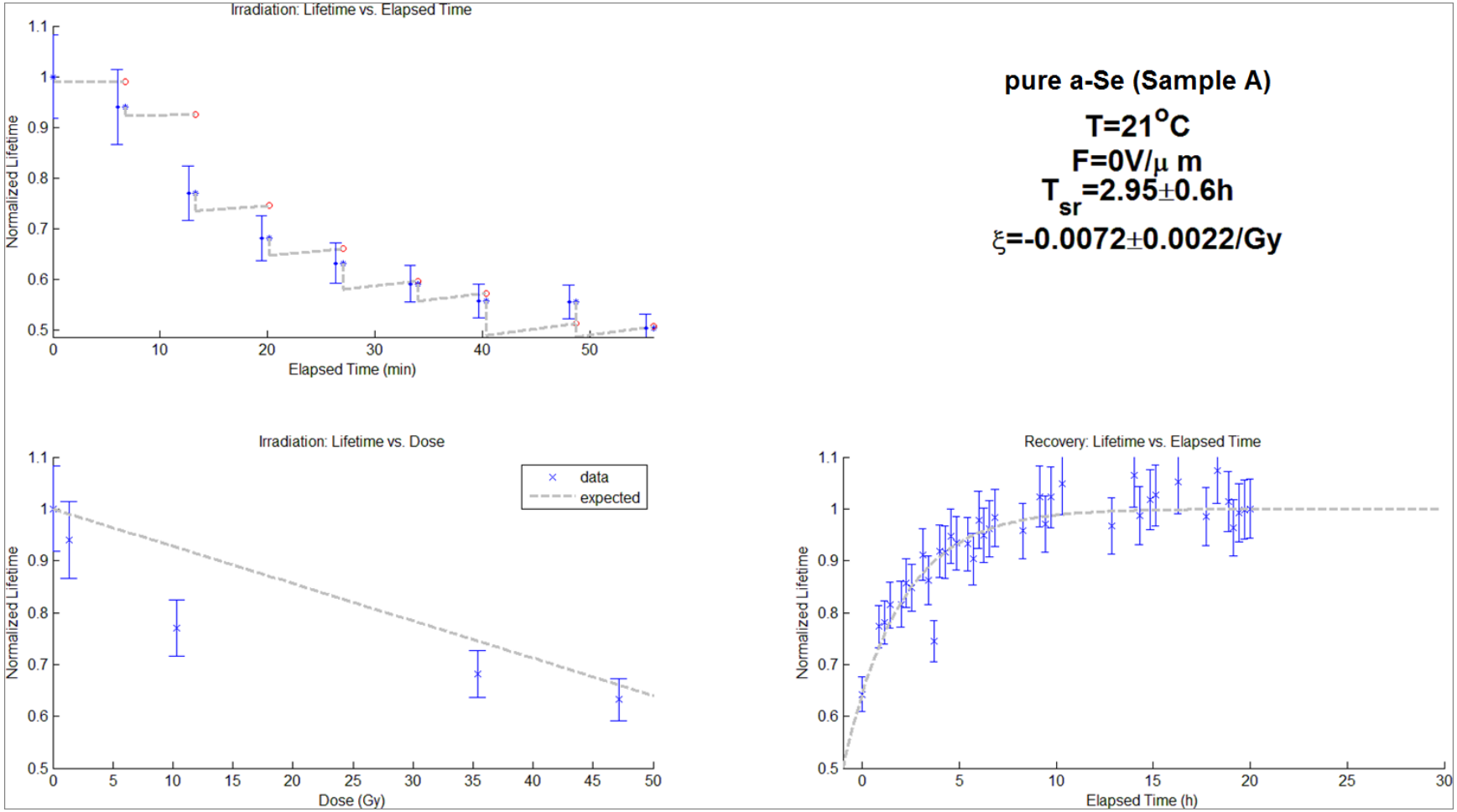

Figure A.1: Plots of the irradiation and recovery experiment for sample A at a temperature of 21°C and a field of 0 V/μm .

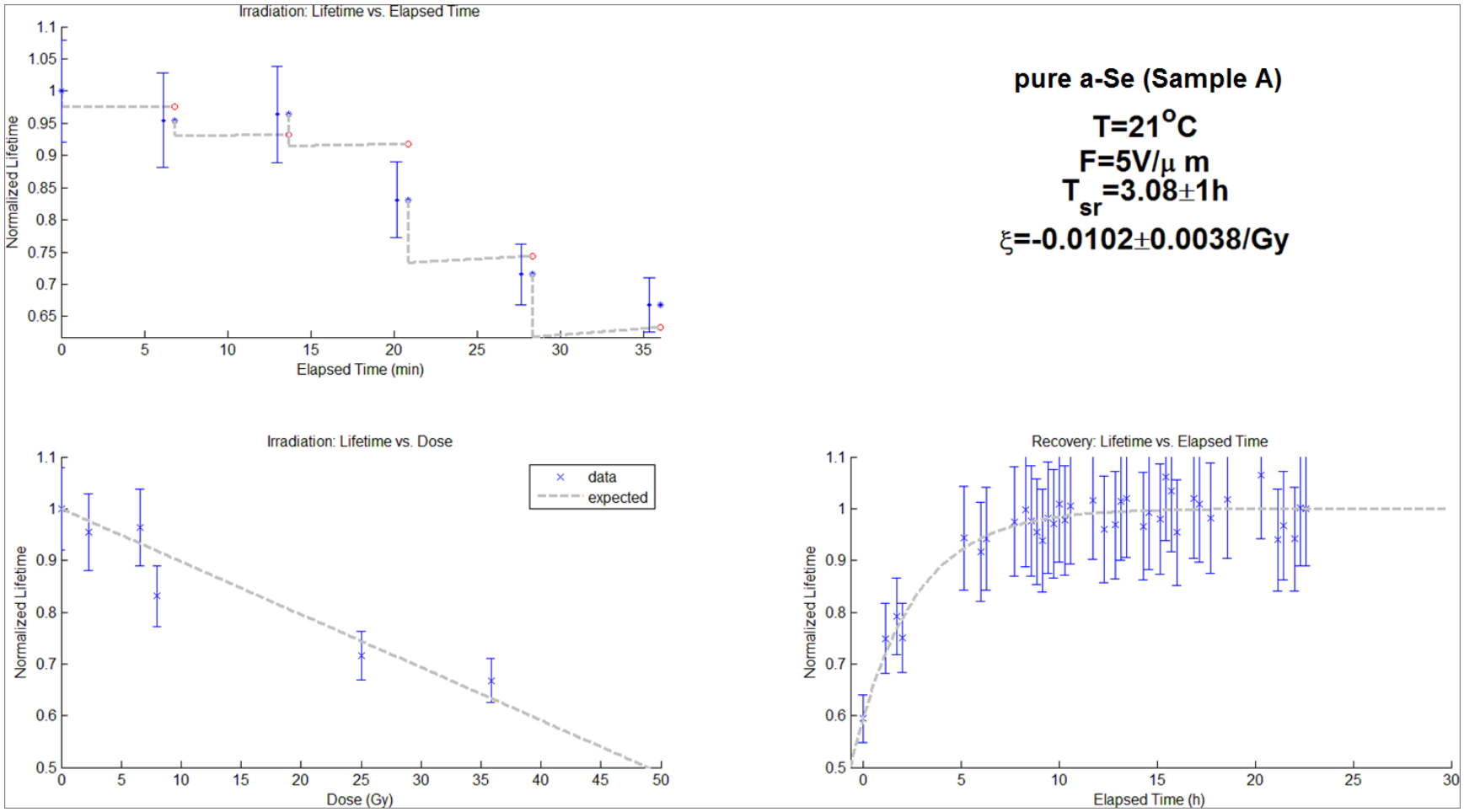

Figure A.2: Plots of the irradiation and recovery experiment for sample A at a temperature of 21°C and a field of 5 V/μm .

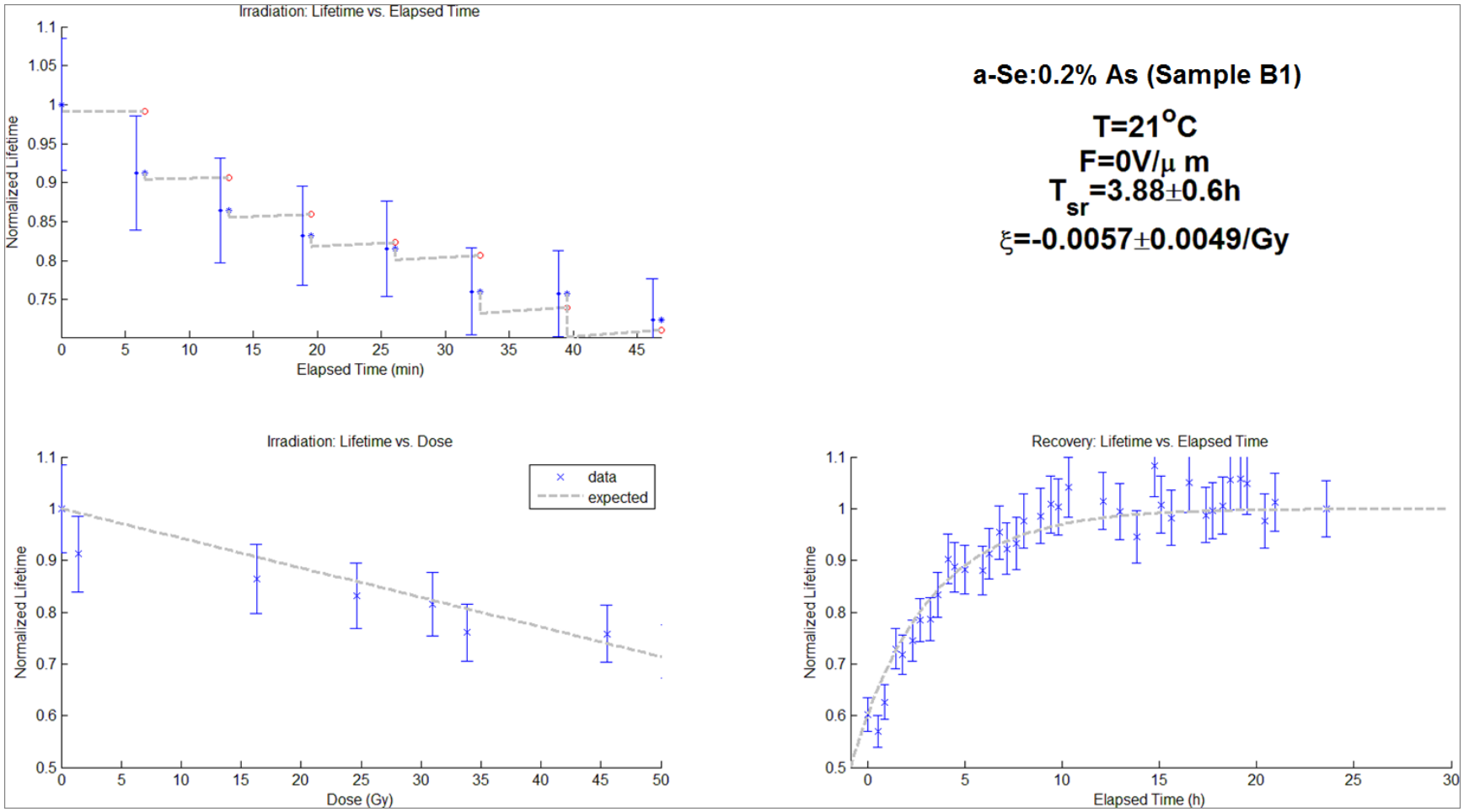

Figure A.3: Plots of the irradiation and recovery experiment for sample B1 at a temperature of 21°C and a field of 0 V/μm .

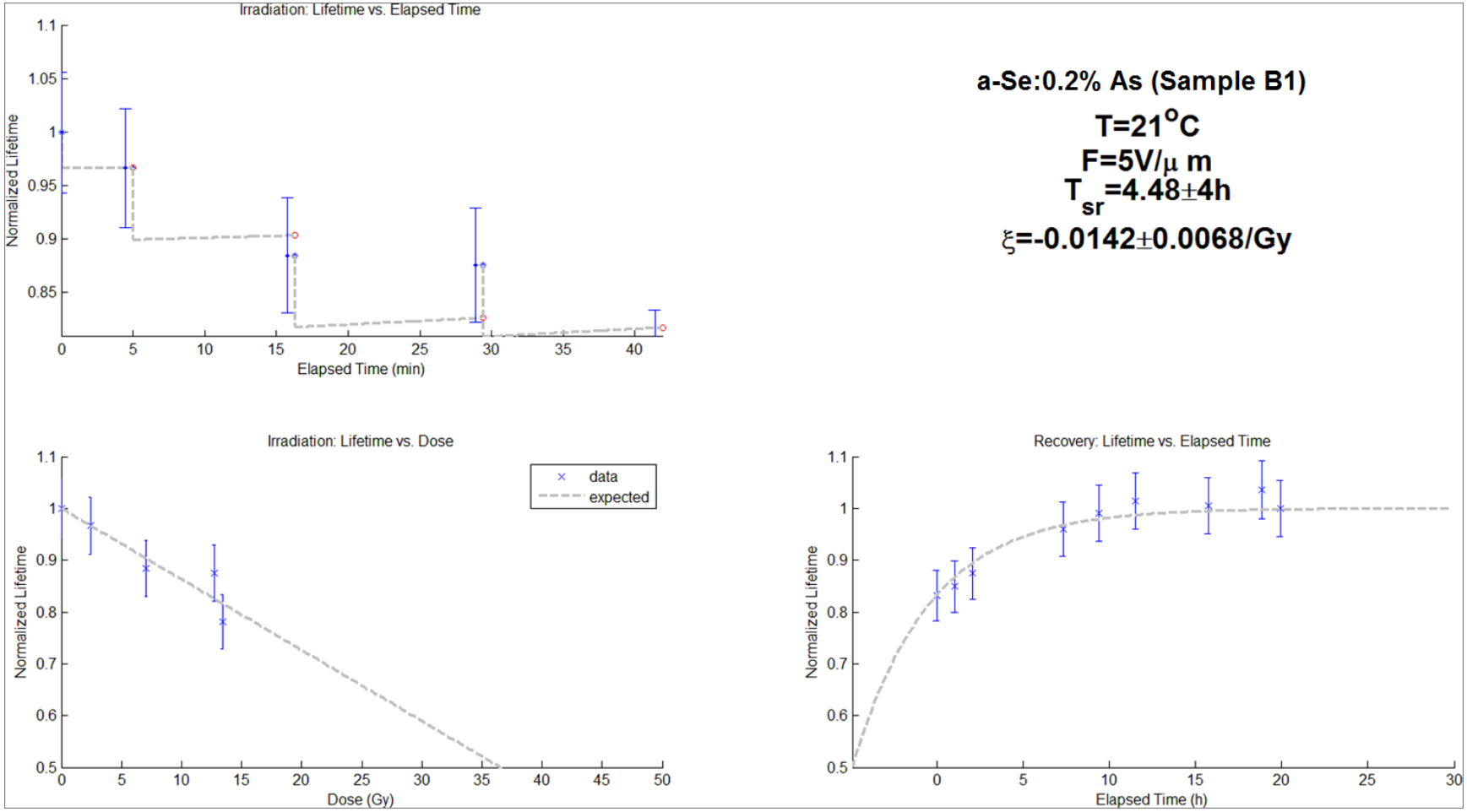

Figure A.4: Plots of the irradiation and recovery experiment for sample B1 at a temperature of 21°C and a field of 5 V/μm .

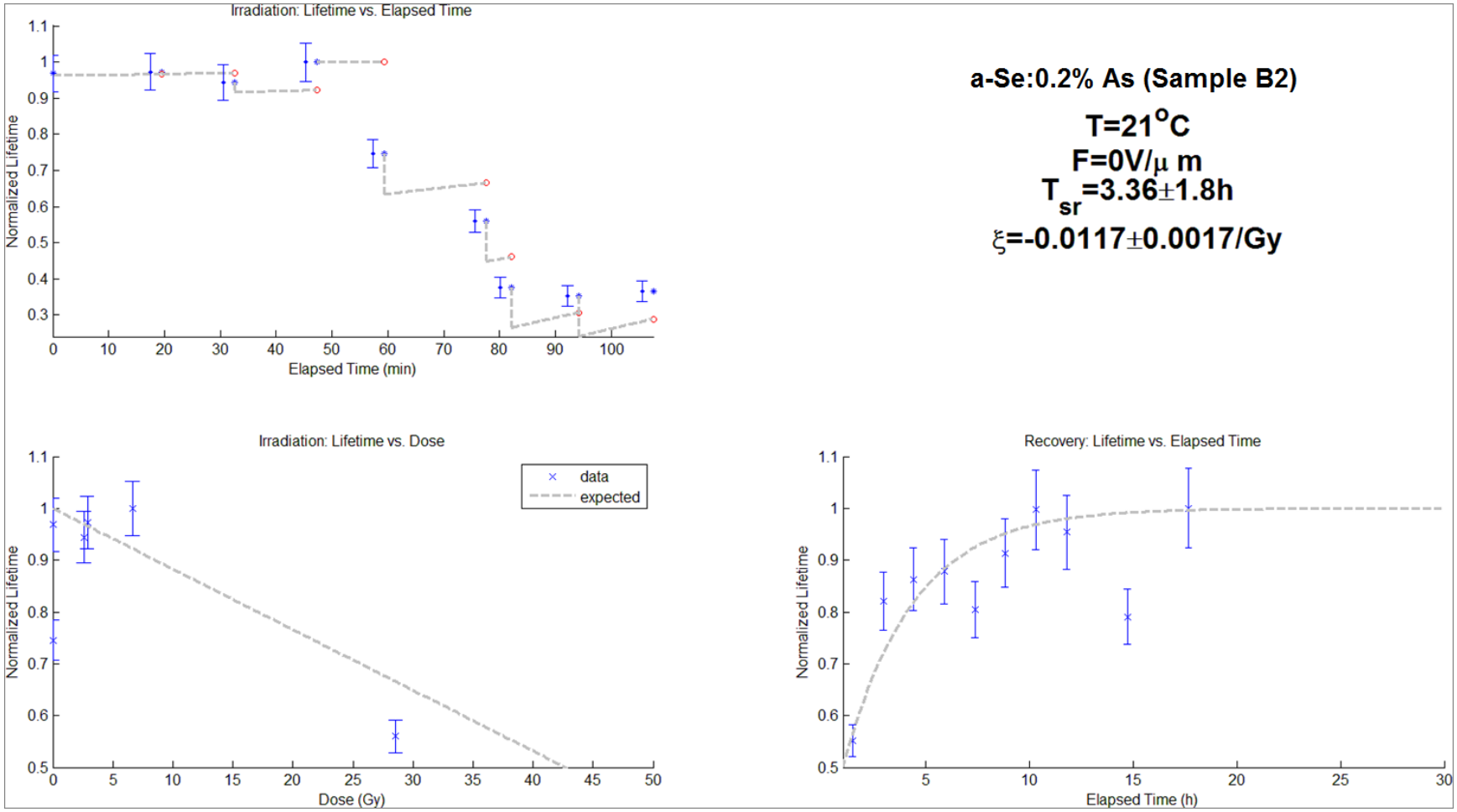

Figure A.5: Plots of the irradiation and recovery experiment for sample B2 at a temperature of 21°C and a field of 0 V/μm .

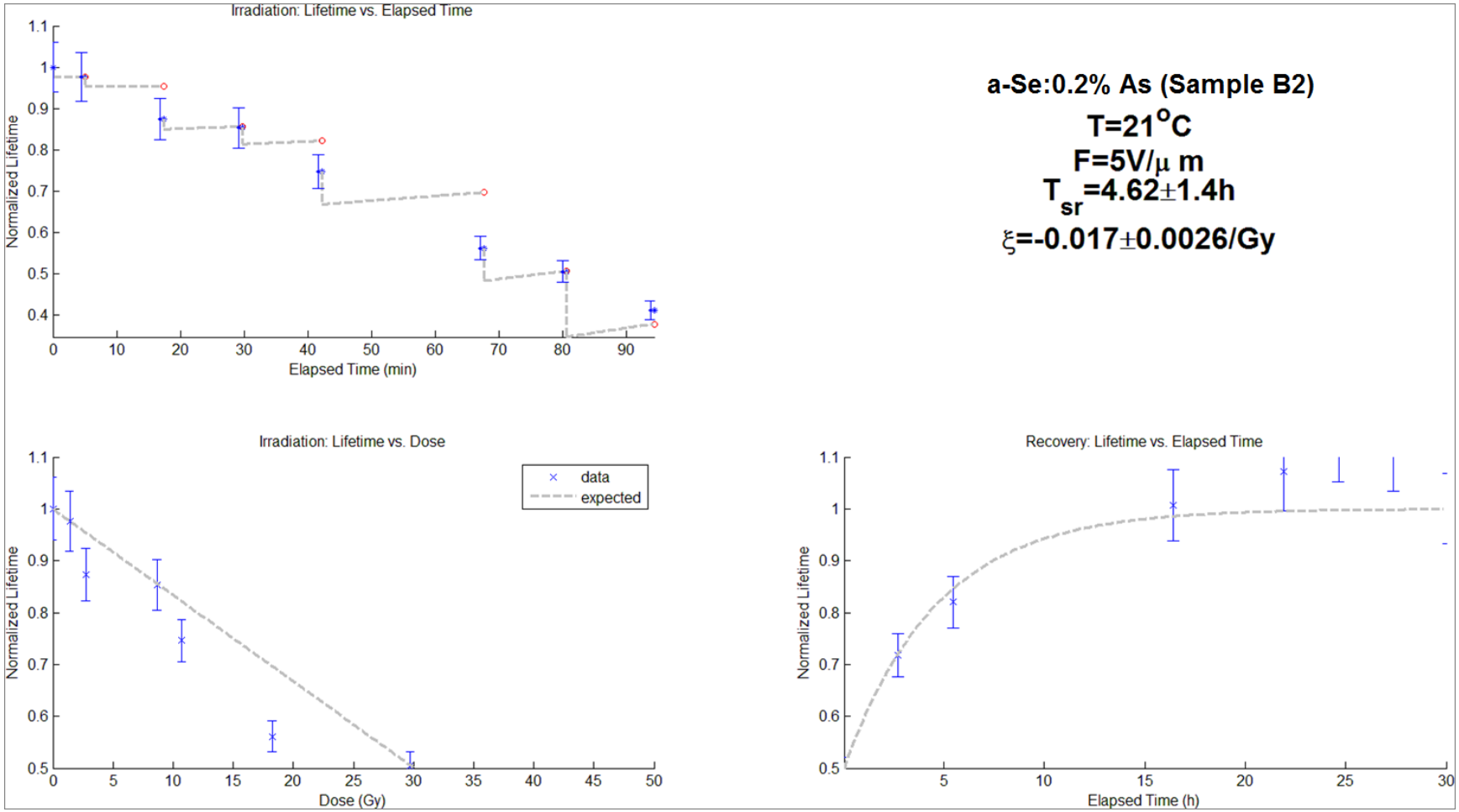

Figure A.6: Plots of the irradiation and recovery experiment for sample B2 at a temperature of 21°C and a field of 5 V/μm .

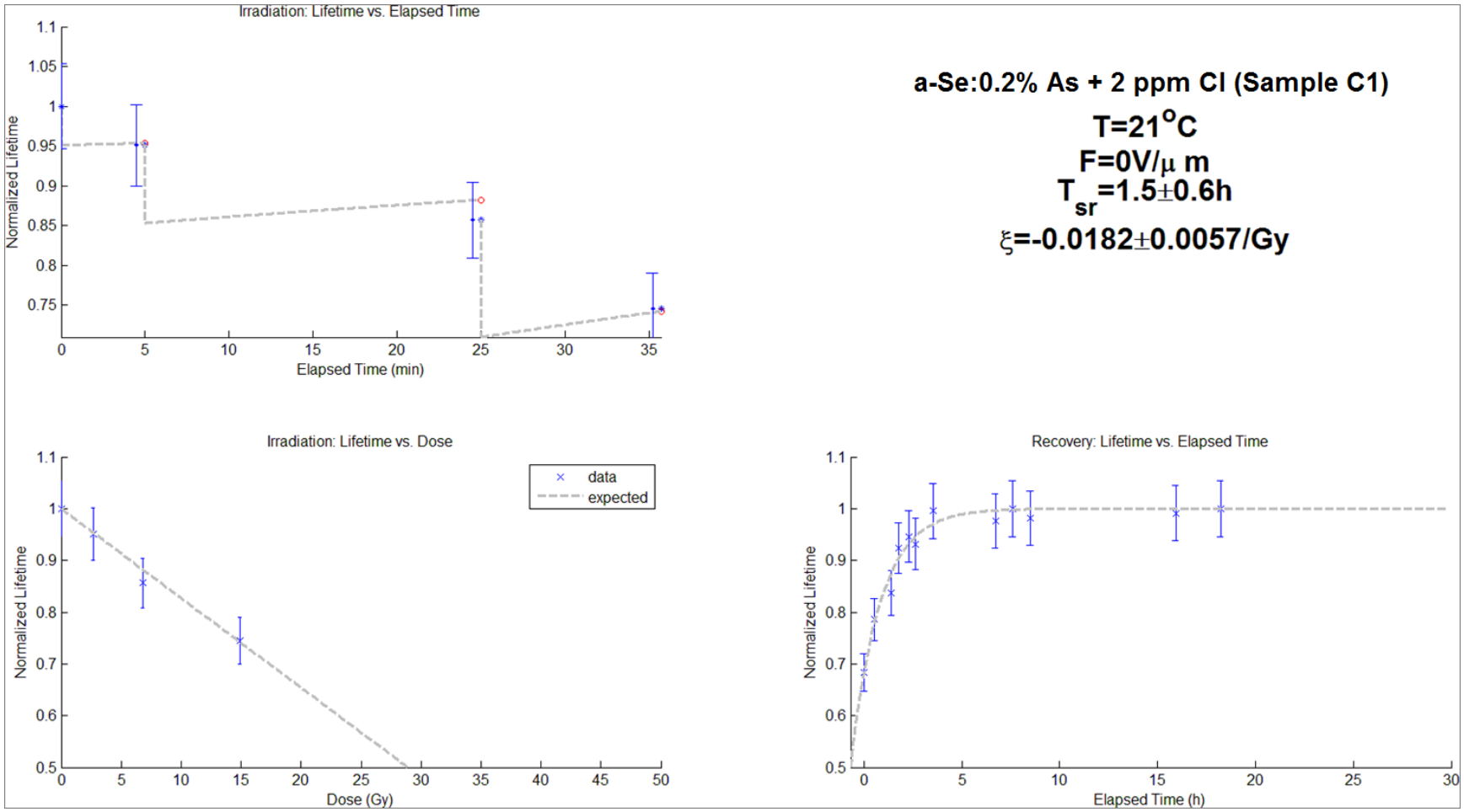

Figure A.7: Plots of the irradiation and recovery experiment for sample C1 at a temperature of 21°C and a field of 0 V/μm .

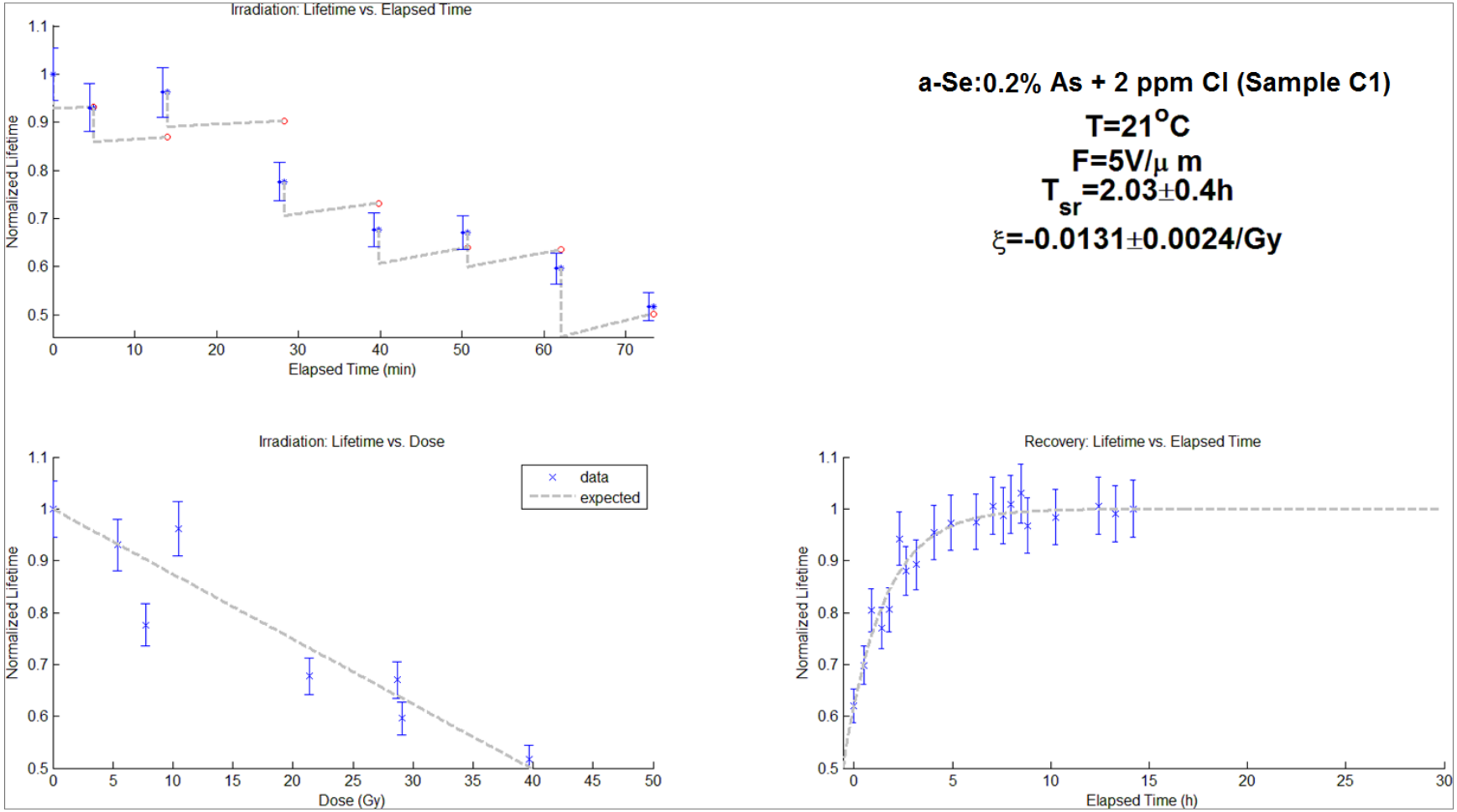

Figure A.8: Plots of the irradiation and recovery experiment for sample C1 at a temperature of 21°C and a field of 5 V/μm .

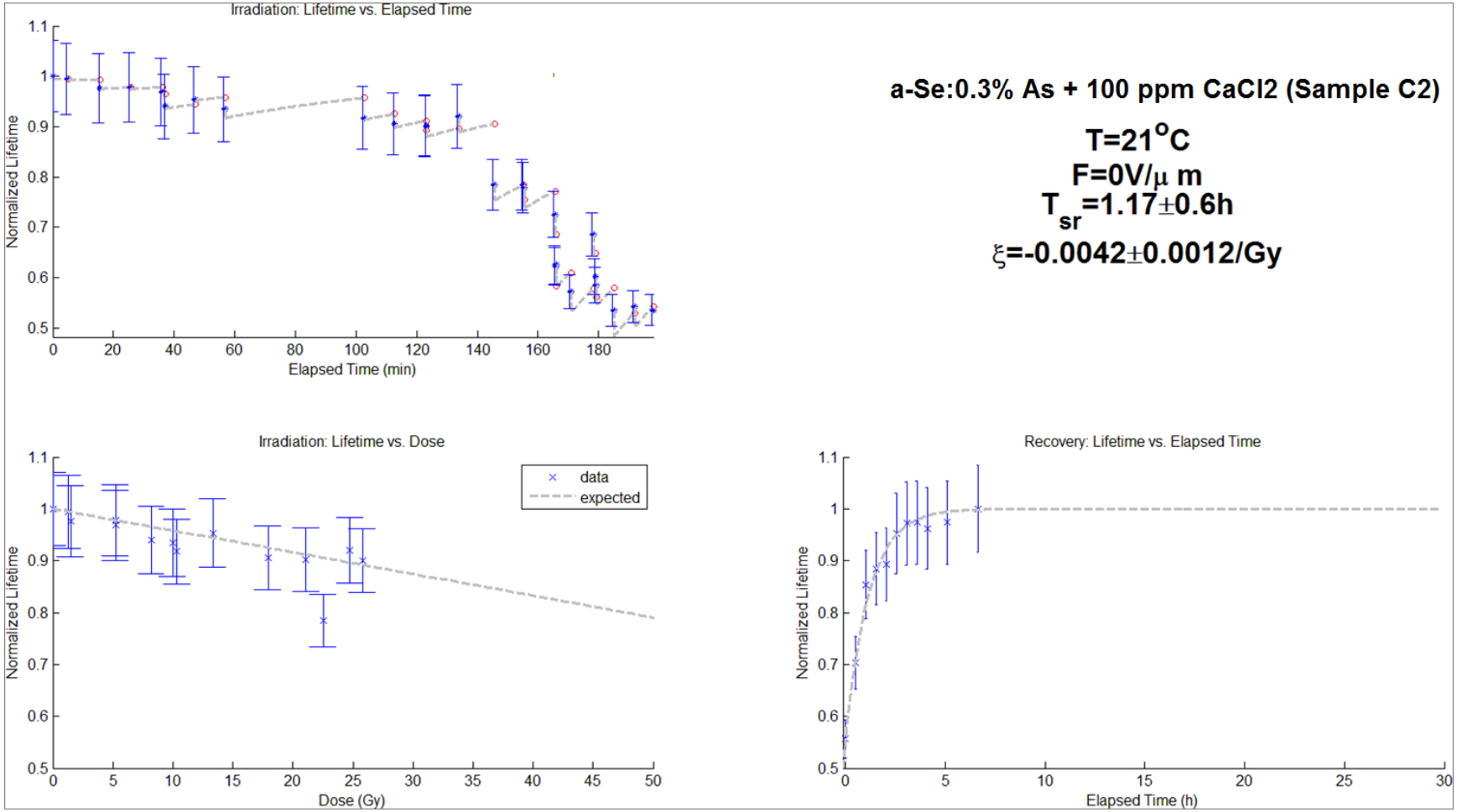

Figure A.9: Plots of the irradiation and recovery experiment for sample C2 at a temperature of 21°C and a field of 0 V/μm .

A.2 Experiments Performed at a Sample Temperature of $35\,^{\circ}\mathrm{C}$

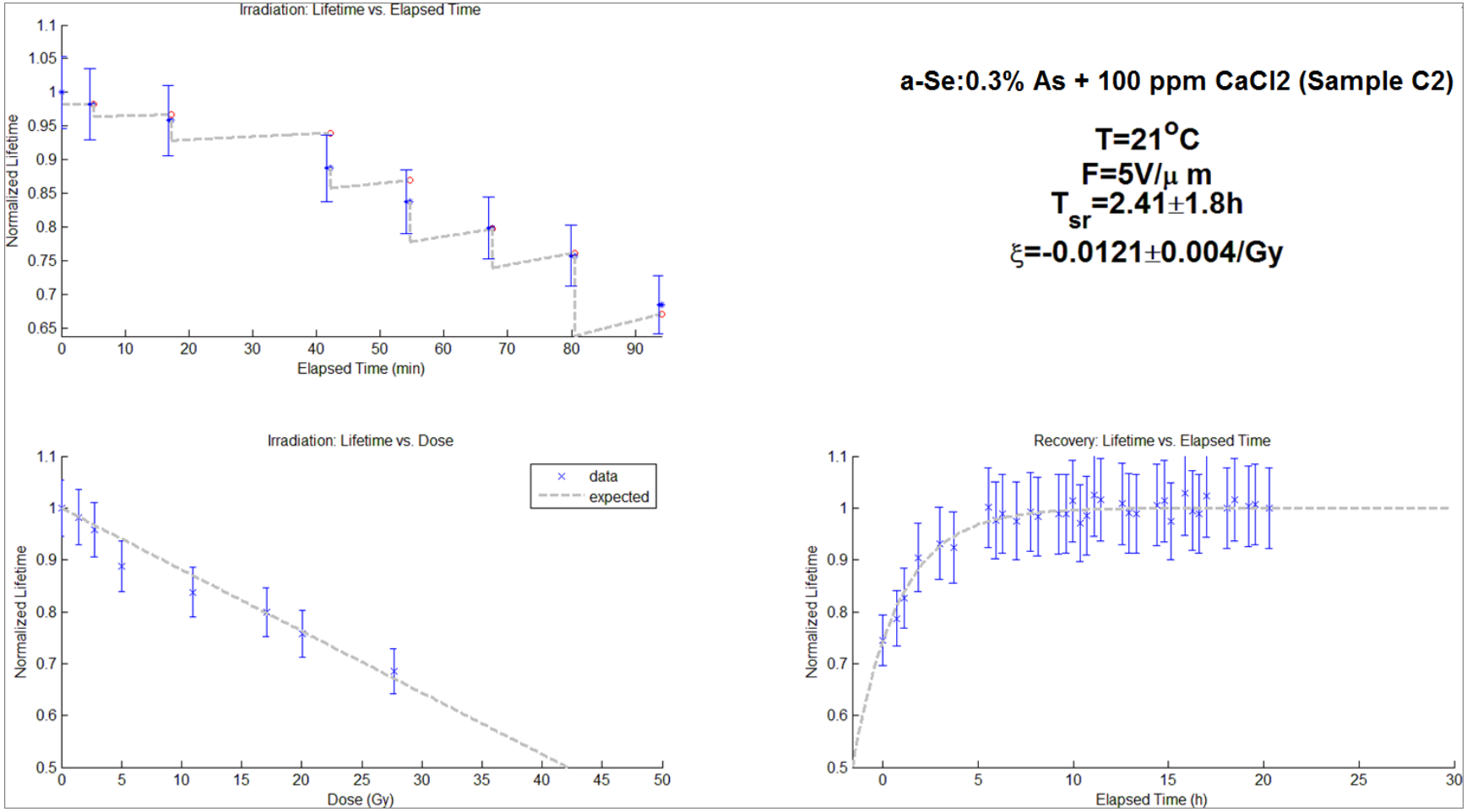

Figure A.10: Plots of the irradiation and recovery experiment for sample C2 at a temperature of 21°C and a field of 5 V/μm .

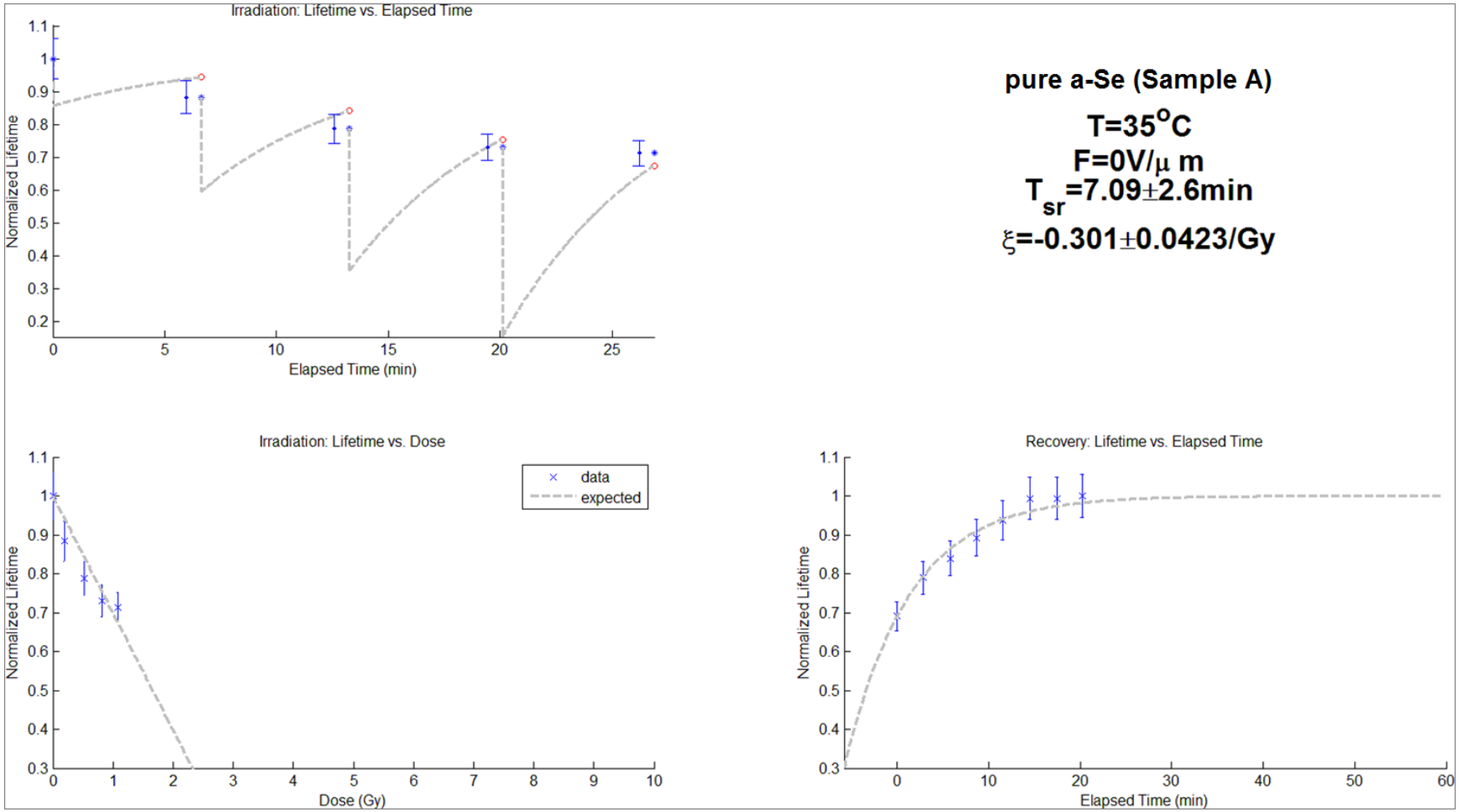

Figure A.11: Plots of the irradiation and recovery experiment for sample A at a temperature of 35°C and a field of 0 V/μm .

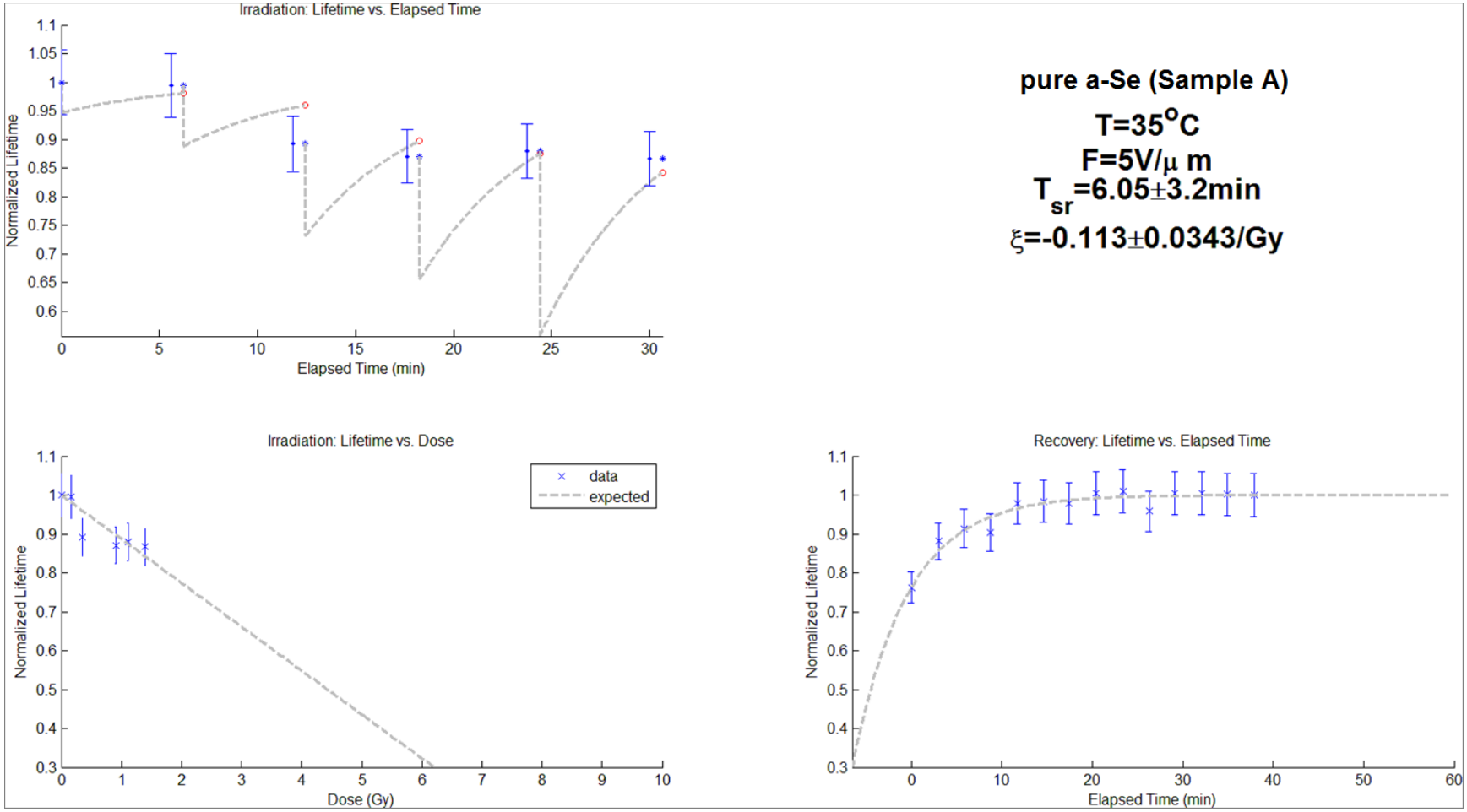

Figure A.12: Plots of the irradiation and recovery experiment for sample A at a temperature of 35°C and a field of 5 V/μm .

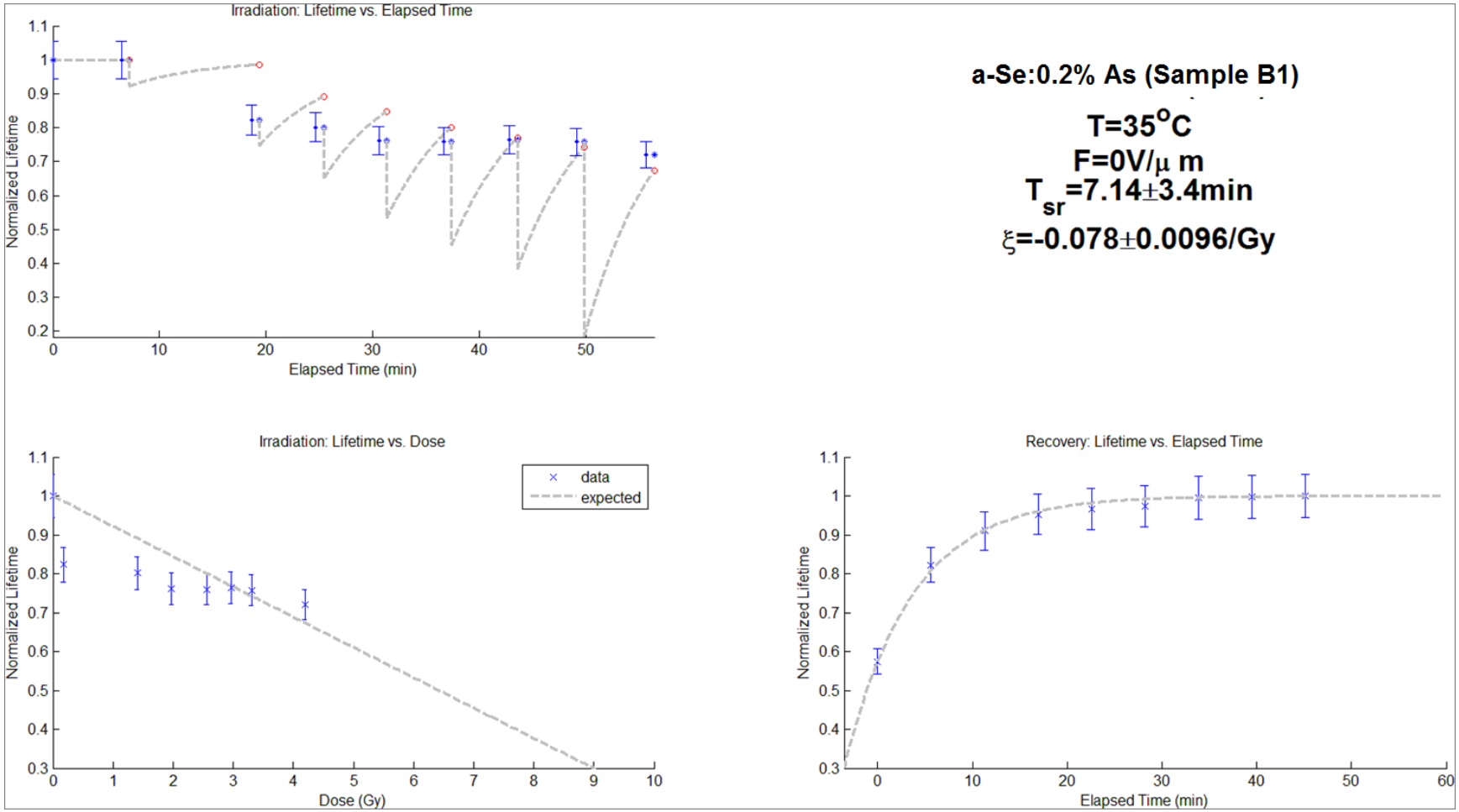

Figure A.13: Plots of the irradiation and recovery experiment for sample B1 at a temperature of 35°C and a field of 0 V/μm .

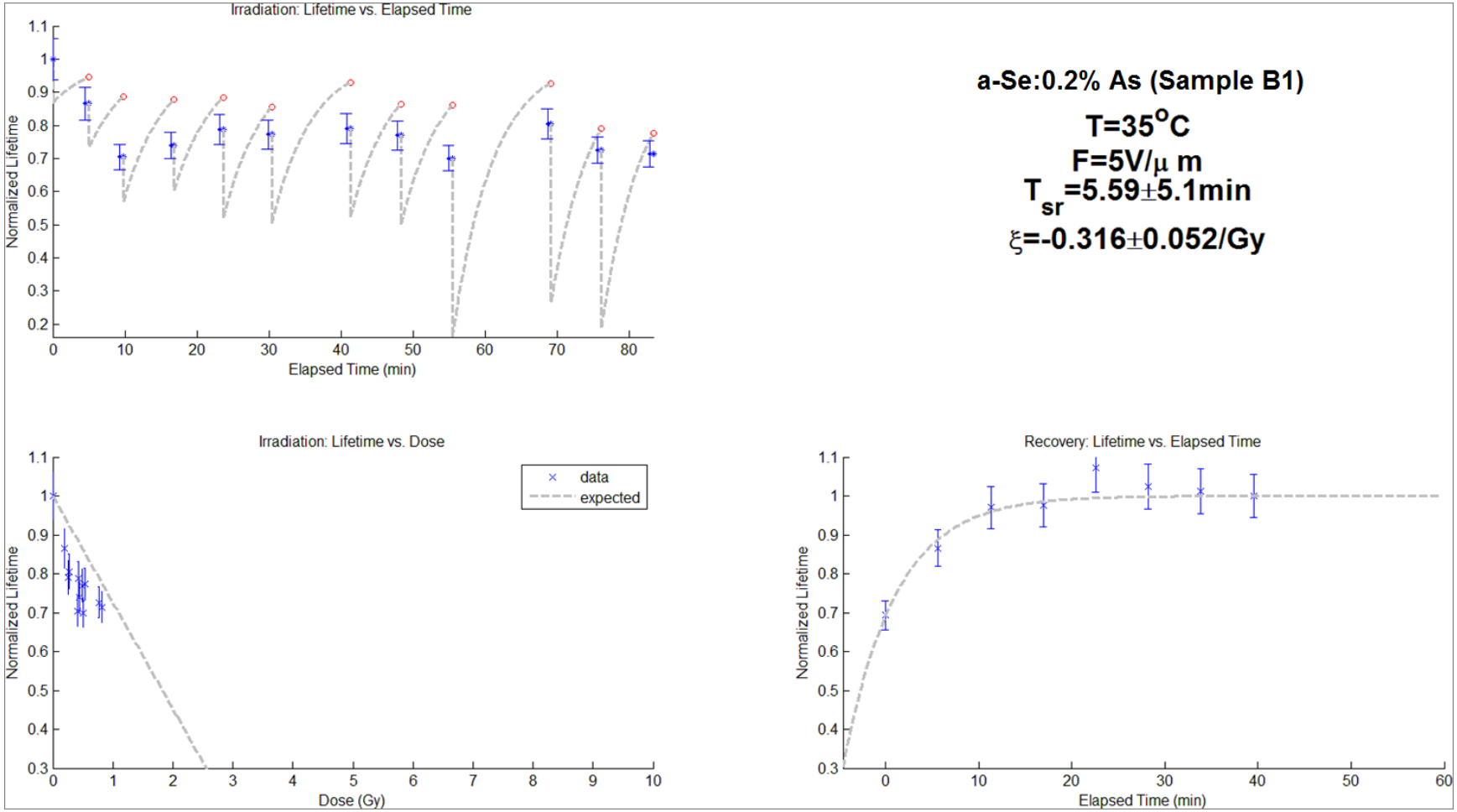

Figure A.14: Plots of the irradiation and recovery experiment for sample B1 at a temperature of 35°C and a field of 5 V/μm .

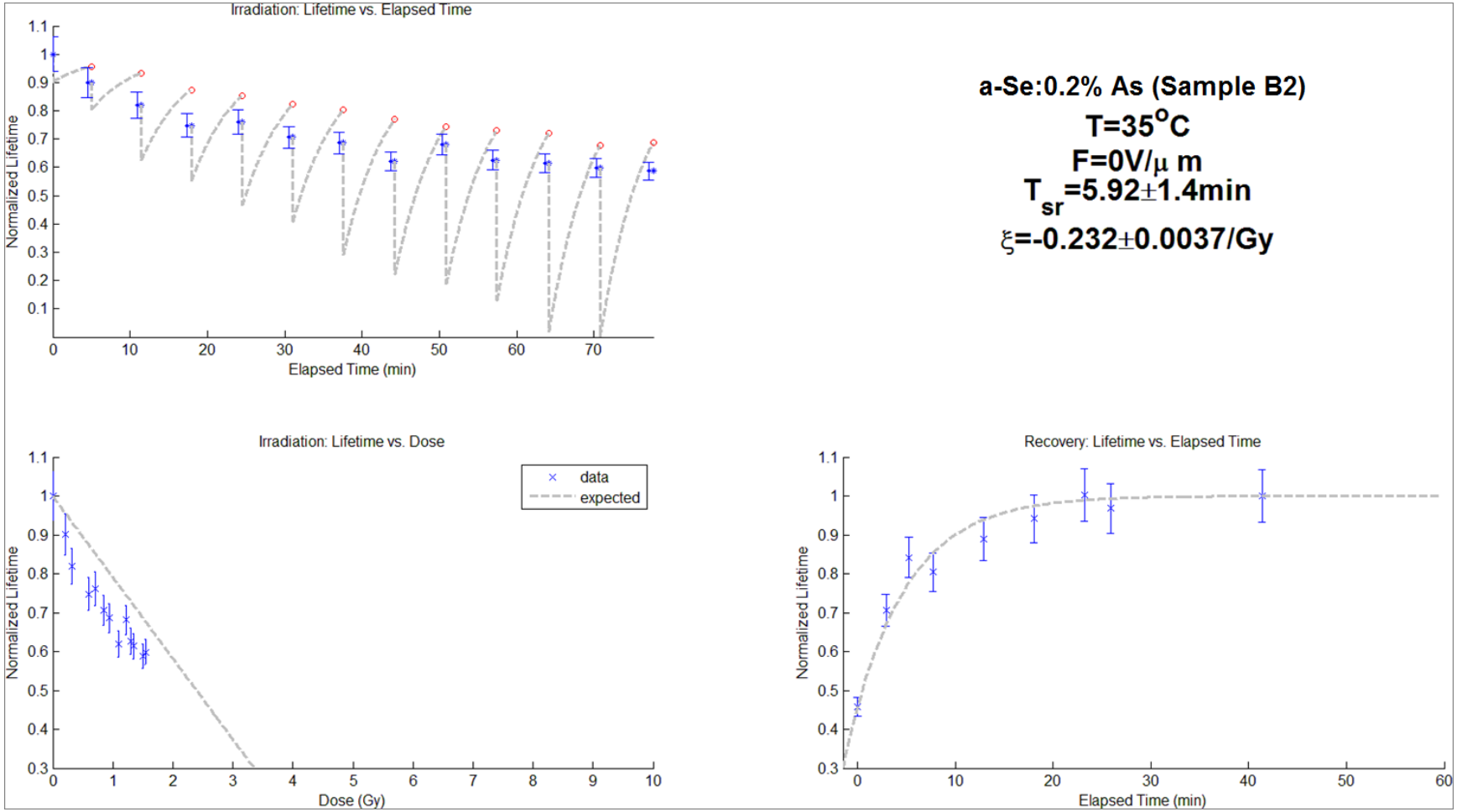

Figure A.15: Plots of the irradiation and recovery experiment for sample B2 at a temperature of 35°C and a field of 0 V/μm .

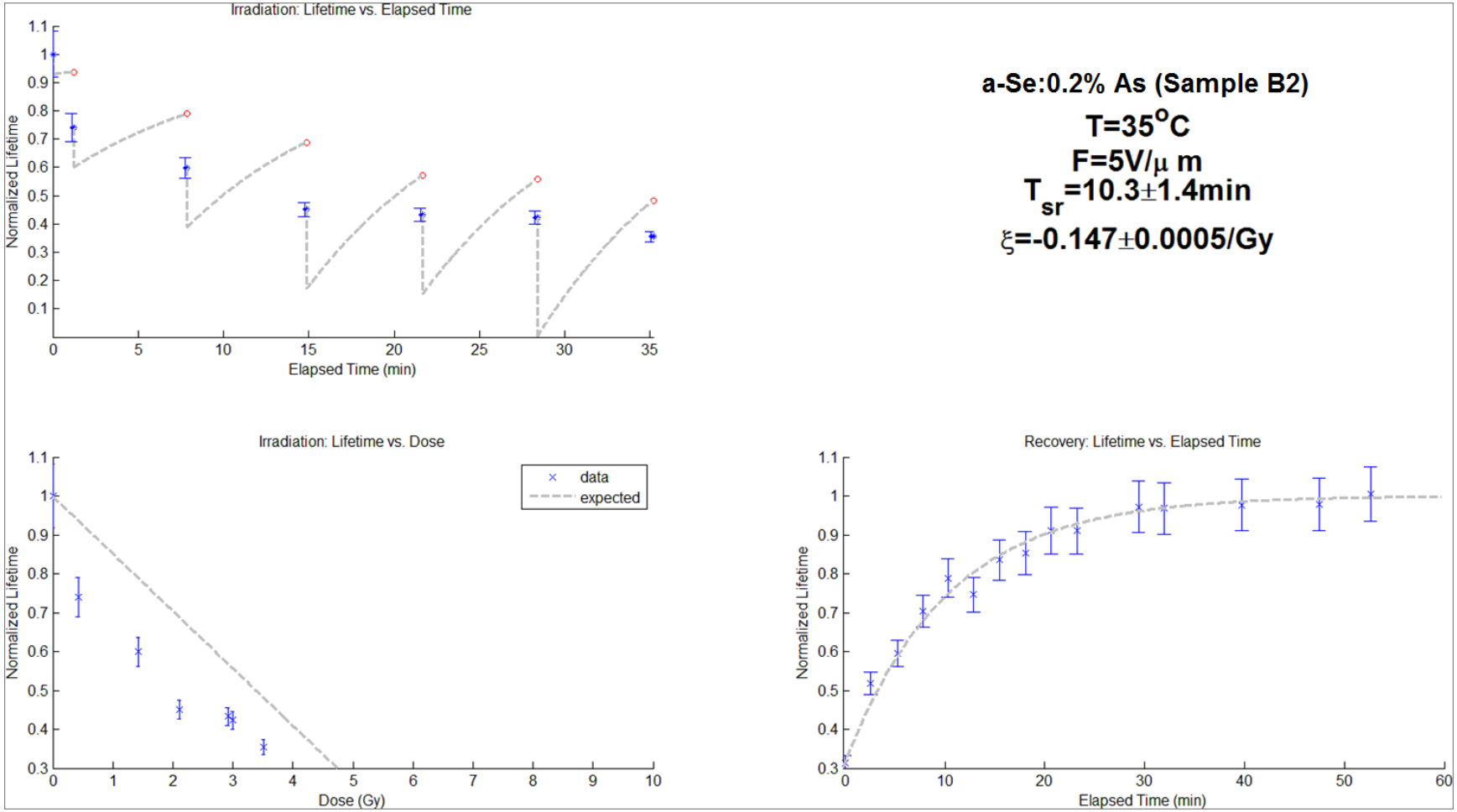

Figure A.16: Plots of the irradiation and recovery experiment for sample B2 at a temperature of 35°C and a field of 5 V/μm .

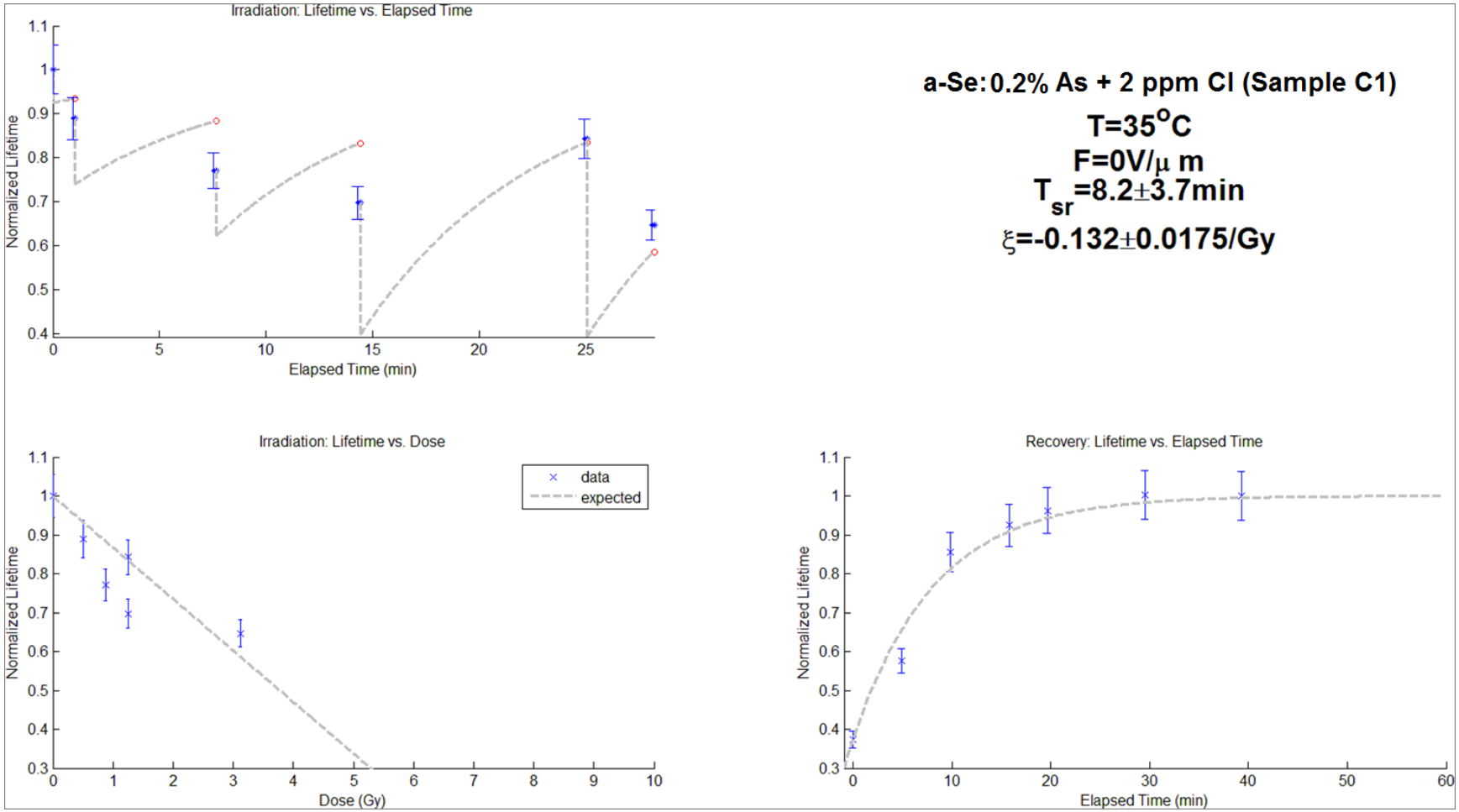

Figure A.17: Plots of the irradiation and recovery experiment for sample C1 at a temperature of 35°C and a field of 0 V/μm .

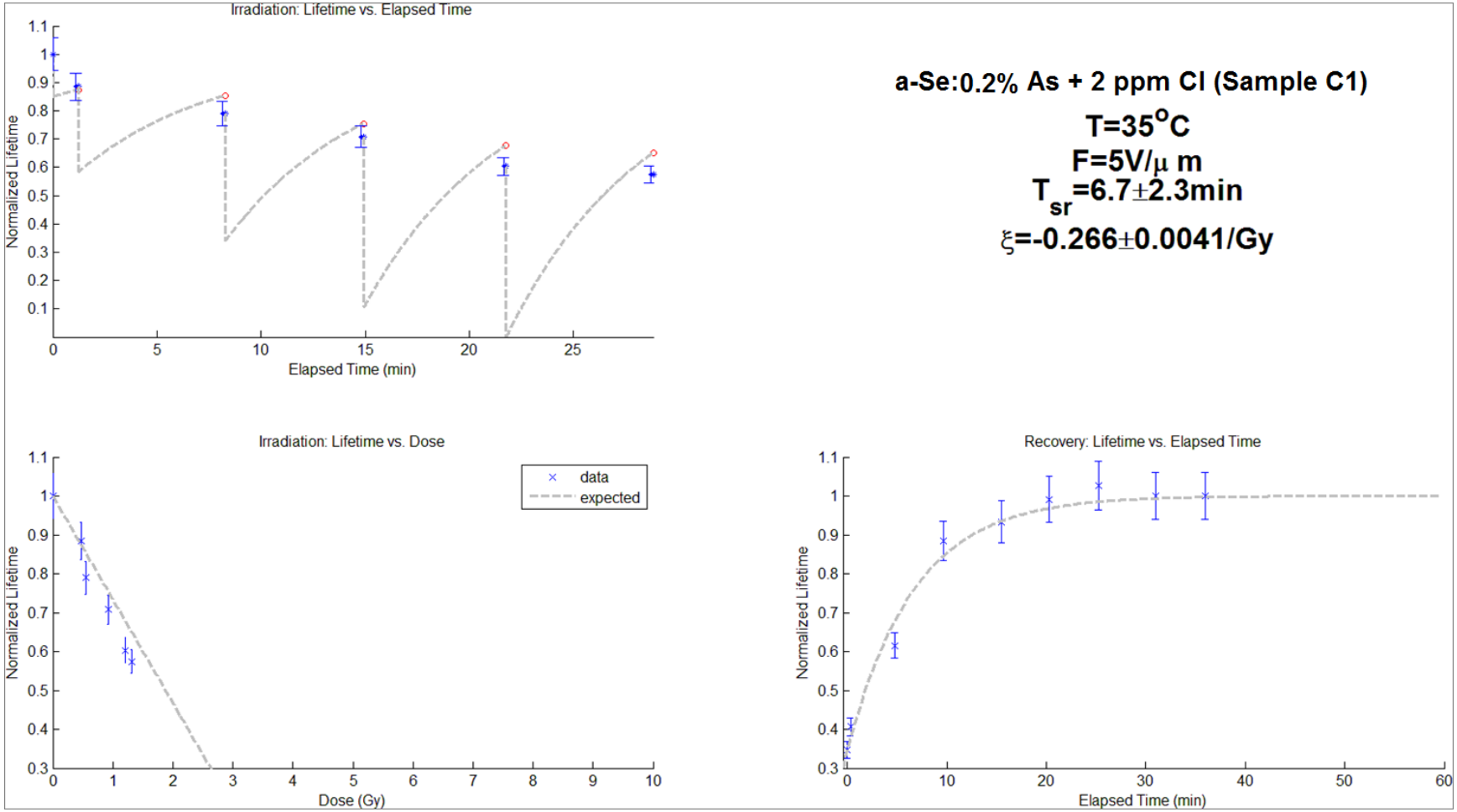

Figure A.18: Plots of the irradiation and recovery experiment for sample C1 at a temperature of 35°C and a field of 5 V/μm .

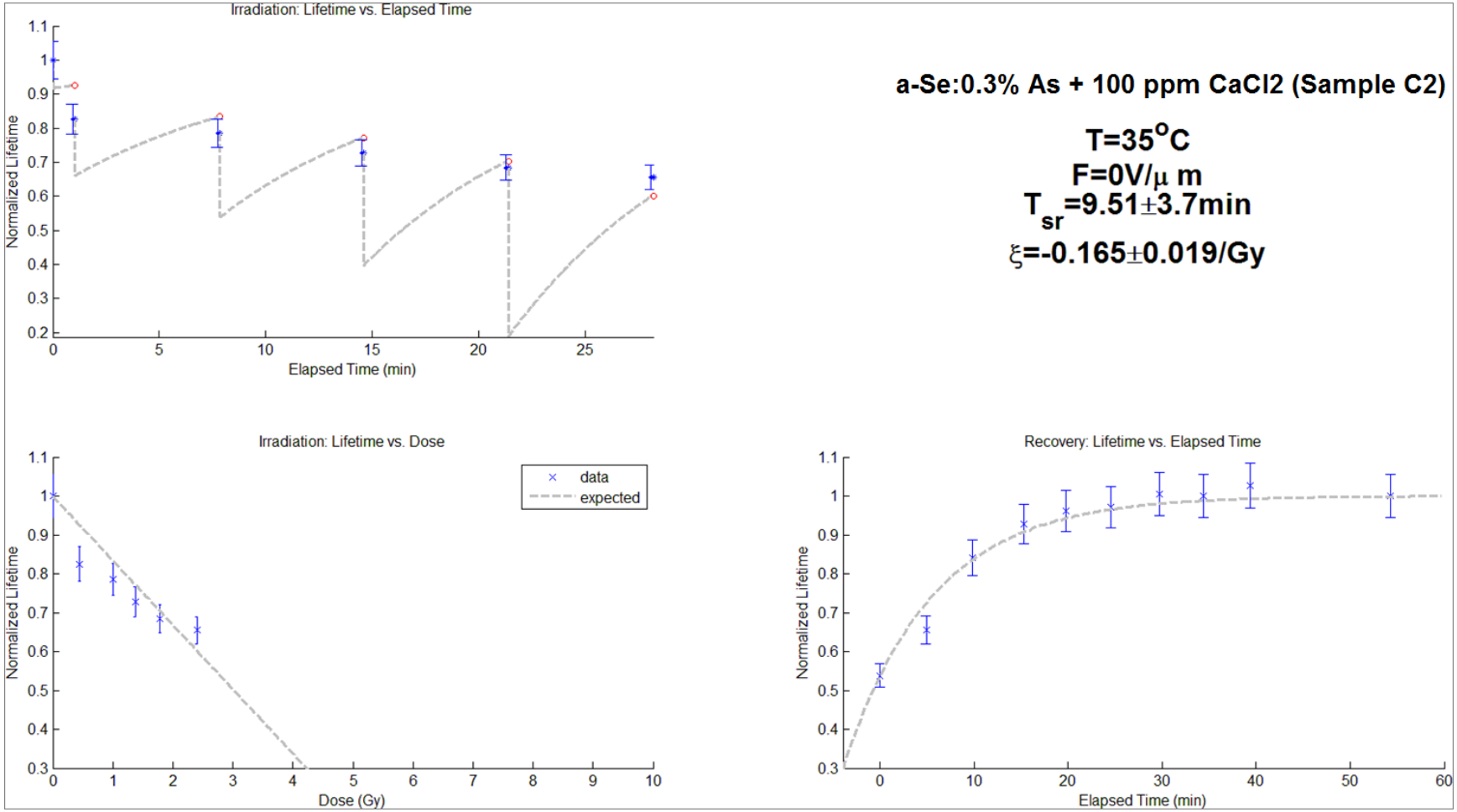

Figure A.19: Plots of the irradiation and recovery experiment for sample C2 at a temperature of 35°C and a field of 0 V/μm .

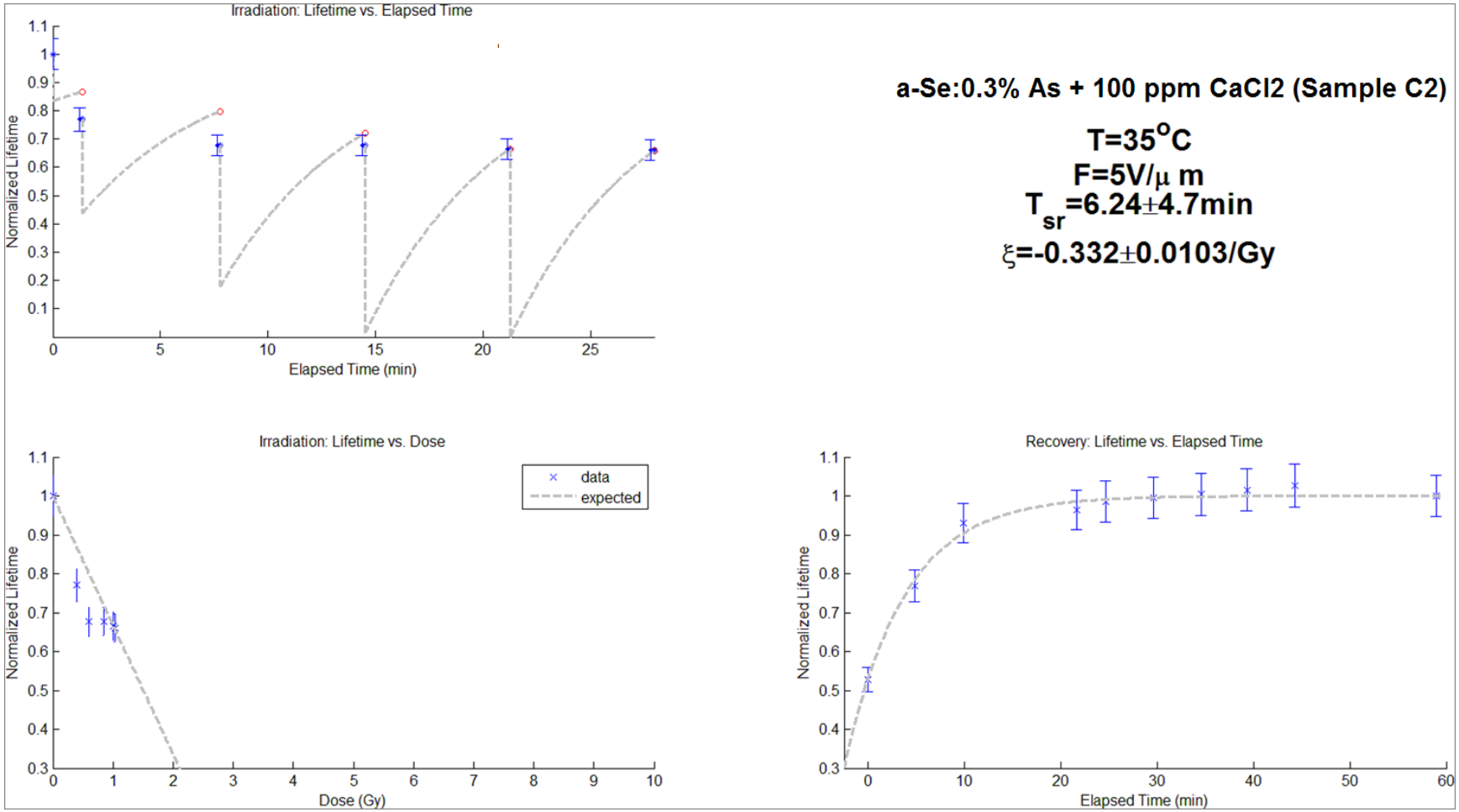

Figure A.20: Plots of the irradiation and recovery experiment for sample C2 at a temperature of 35°C and a field of 5 V/μm .

References

[1] B. Fogal, "Electronic transport properties of stabilized amorphous selenium x-ray photoconductors," Master's thesis, Saskatchewan, 2005.

[2] C. Allen, "Relaxation in the electrical properties of amorphous selenium based photoconductors," Master's thesis, Saskatchewan, 2009.

[3] (2012, November) Direct x-ray detectors. http://www.anrad.com/products-direct-xray-detectors.htm. Analogic Corporation. Peabody, MA.

[4] S.O. Kasap, Chapter 9: "Photoreceptors - The Chalcogenicdes", in *The Handbook of Imaging Materials, Second Edition*, (Marcel Dekker, New York, 2002), 329-368.

[5] M. Yaffe and J. Rowlands, "X-ray detectors for digital radiography," *Physics in Medicine and Biology*, vol. 42, no. 1, p. 1, 1999.

[6] S. Kasap and J. A. Rowlands, "Direct-conversion flat-panel x-ray image sensors for digital radiography," *Proceedings of the IEEE*, vol. 90, no. 4, pp. 591–604, 2002.

[7] G. Lucovsky, "Selenium, the amorphous and liquid states," in *The physics of selenium and tellurium*, ser. Springer Series in Solid-State Sciences, E. Gerlach and P. Grosse, Eds., vol. 13. New York: Springer-Verlag, 1979, pp. 178–192.

[8] D. Adler and E. J. Yoffa, "Electronic structure of amorphous semiconductors," *Phys. Rev. Lett.*, vol. 36, pp. 1197–1200, May 1976. [Online]. Available: http://link.aps.org/doi/10.1103/PhysRevLett.36.1197

[9] M. Abkowitz, "Density of states in a-Se from combined analysis of xerographic potentials and transient transport data," *Philosophical Magazine Letters*, vol. 58, pp. 53–57, 1988.

[10] D. M. Pai and R. C. Enck, "Onsager mechanism of photogeneration in amorphous selenium," *Physics Review B*, vol. 11, pp. 5163–5174, 1975.

[11] Haugen, "Charge transport in stabilized a-Se films used in x-ray image detector applications," Ph.D. dissertation, Saskatchewan, 1999.

[12] A. Reznik, B. Lui, V. Lyubin, M. Klebanov, Y. Ohkawa, T. Matsubara, K. Miyakawa, M. Kubota, K. Tanioka, T. Kawai *et al.*, "The effect of temperature on photoinduced metastability in avalanche a-Se layers," *Journal of non-crystalline solids*, vol. 352, no. 9, pp. 1595–1598, 2006.

[13] K. Tanaka and K. Shimakawa, *Amorphous chalcogenide semiconductors and related materials*. Springer, 2011.

[14] S. Seltzer. (2013, April) Tables of x-ray mass attenuation coefficients and mass energy-absorption coefficients from 1 keV to 20 MeV for elements Z = 1 to 92 and 48 additional substances of dosimetric interest. http://www.nist.gov/pml/data/xraycoef/. National Institute of Standards and Technology. [Online]. Available: http://www.nist.gov/pml/data/xraycoef/

[15] M. L. Giger, F.-F. Yin, K. Doi, Y. Wu, C. J. Vyborny, R. A. Schmidt, and Z. Huo, "Computerized detection and characterization of mass lesions in digital mammography," in *Proc. IEEE Int Systems, Man and Cybernetics Conf*, 1992, pp. 1370–1372.

[16] A. Youssif, M. U. Chowdhury, and S. Ray, "Computer aided analysis of dental radiographic images," in *Proc. Digital Image Computing: Techniques and Applications*, 2005.

[17] R. Svoboda and J. Málek, "Structural relaxation in Se-rich As–Se glasses," *Journal of Non-Crystalline Solids*, vol. 363, pp. 89–95, 2013.

[18] R. Alig and S. Bloom, "Secondary-electron-escape probabilities," *Journal of Applied Physics*, vol. 49, no. 6, pp. 3476–3480, 1978.

[19] B. Streetman and S. Banerjee, *Solid state electronic devices*, 4th ed. Prentice-Hall Englewood Cliffs, NJ, 1995.

[20] S. Kasap, *Principles of electronic materials and devices*, 3rd ed. McGraw-Hill New York, 2006.

[21] J. Siewerdsen, L. Antonuk, Y. El-Mohri, J. Yorkston, W. Huang, and I. Cunningham, "Signal, noise power spectrum, and detective quantum efficiency of indirect-detection flat-panel imagers for diagnostic radiology," *Medical physics*, vol. 25, p. 614, 1998.

[22] S. Kasap, "X-ray sensitivity of photoconductors: application to stabilized a-Se," *J. Phys. D: Appl. Phys.*, vol. 33, p. 2853, 2000.

[23] M. Z. Kabir, S. O. Kasap, W. Zhao, and J. A. Rowlands, "Direct conversion x-ray sensors: sensitivity, dqe and mtf," *IEE Proceedings -Circuits, Devices and Systems*, vol. 150, no. 4, 2003.

[24] J. Black, P. Deines-Jones, S. Ready, and R. Street, "X-ray polarimetry with an active-matrix pixel proportional counter," *Nuclear Instruments and Methods in Physics Research Section A: Accelerators, Spectrometers, Detectors and Associated Equipment*, vol. Volume 513, Issue 3, p. 639643, 2003.

[25] S. Kasap and J. A. Rowlands, "Review x-ray photoconductors and stabilized a-Se for direct conversion digital flat-panel x-ray image-detectors," *Journal of Materials Science: Materials in Electronics*, vol. 11, pp. 179–198, 2000. [Online]. Available: http://dx.doi.org/10.1023/A:1008993813689

[26] A. Sultana, A. Reznik, K. Karim, and J. Rowlands, "Effect of anomalous scattering and k-fluroscence reabsorption on the performance of selenium," in *Semiconductor Conference, 2008. CAS 2008. International*, vol. 1. IEEE, 2008, pp. 193–196.

[27] S. Kasap and J. Rowlands, "Direct-conversion flat-panel x-ray image detectors," *IEE Proceedings -Circuits, Devices and Systems*, vol. 149, no. 2, pp. 85–96, 2002.

[28] C. A. Klein, "Bandgap dependence and related features of radiation ionization energies in semiconductors," *Journal of Applied Physics*, vol. 39, no. 4, pp. 2029–2038, 1968.

[29] W. Que and J. Rowlands, "X-ray photogeneration in amorphous selenium: Geminate versus columnar recombination," *Physical Review B*, vol. 51, no. 16, p. 10500, 1995.

[30] S. O. Kasap and J. A. Rowlands, "Photoconductor selection for digital flat panel x-ray image detectors based on the dark current," *and Films Journal of Vacuum Science & Technology A: Vacuum, Surfaces*, vol. 18, no. 2, pp. 615–620, 2000.

[31] S. O. Kasap, *The Optics Encyclopedia*. Wiley-VCH, 2004, vol. 4, ch. Optoelectronics, pp. 1–48.

[32] J. Mort, *The anatomy of xerography: Its invention and evolution*. McFarland, 1989.

[33] R. Street, *Hydrogenated amorphous silicon*. Cambridge University Press, 1990.

[34] A. Madan and M. Shaw, *The Physics and Applications of Amorphous Semiconductors*. Academic Press, 1988.

[35] N. Mott, "Electrons in disordered structures," *Advances in Physics*, vol. 16, pp. 49–57, 1967.

[36] P. Anderson, "Absence of diffusion in certain random lattices," *Physical Review*, vol. 109, pp. 1492–1505, 1958.

[37] M. Brodsky, *Amorphous semiconductors*, 2nd ed. New York: Springer-Verlag, Feb 1979, vol. 4.

[38] M. Cohen, H. Fritzsche, and S. Ovshinski, "Simple band model for amorphous semiconductor alloys," *Physical Review Letters*, vol. 22, pp. 1065–1072, 1969.

[39] J. Marshall and A. Owen, "Drift mobility studies in vitreous arsenic triselenide," *Philosophical Magazine*, vol. 24, pp. 1281–1290, 1971.

[40] G. Lucovsky and F. L. Galeener, "Intermediate range order in amorphous solids," *Journal of Non-Crystalline Solids*, vol. 35, pp. 1209–1214, 1980.

[41] P. Meek, "Structural inteipretations of the vibrational spectra of models of amorphous as and se," in *Proceedings of the Symposium on the Structure of Non-Crystalline Solids*, P. Gaskell, Ed. London: Taylor & Franis Ltd., 1977, pp. 235–237.

[42] J. Robertson, "Electronic structure of amorphous semiconductors," *Advances in Physics*, vol. 32, pp. 361–452, 1983.

[43] M. Abkowitz, "Changes in the photoelectric properties of glassy chalcogenides induced by chemical doping, irradiation, and thermal history," *Journal of Chemical Physics*, vol. 46, p. 4537, 1967.

[44] S. Agarwal, "Nature of localized states in amorphous semiconductors: a study by electron spin resonance," *Physical Review B*, vol. 7, pp. 685–691, 1973.

[45] N. Mott and E. Davis, *Electronic Processes in Non-Crystalline Material*. Oxford: Oxford University Press, 1979.

[46] S. Elliot, "A united model for reversible photostructural effects in chalcogenide glasses," *Journal of Non-Crystalline Solids*, vol. 81, pp. 71–98, 1986.

[47] D. Carles, G. Lefrancois, and J. Larmagnac, "A model for steady-state photoconductivity in amorphous selenimn," *Journal of Physics Letters*, vol. 45, pp. L901–L906, 1984.

[48] W. Spear, "Transit time measurements of charge carriers in amorphous selenium films," Master's thesis, University of Leicester, 1957.

[49] A. Rudenko and V. Arkhipov, "Drift and diffusion in materials with traps. i. quasi-equilibrium transport regime," *Philosophical Magazine B*, vol. 45, pp. 177–187, 1982.

[50] S. Kasap and C. Juhasz, "Time-of-flight drift mobility measurements on chlorine-doped amorphous selenimn films," *Journal of Physics D: Applied Physics*, vol. 18, pp. 703–720, 1985.

[51] M. Abkowitz and D. Pai, "Photoelectronic behavior of a-Se and some a- se:as alloys in their glass transition regions," *Physical Review B*, vol. 18, pp. 1741–1750, 1978.

[52] G. Juska, A. Matulionis, and J. Viscakas, "Measurement of thermal release and transit time in case of multiple trapping," *Physica Status Solidi*, vol. 33, pp. 533–539, 1969.

[53] J. M. Marshall and A. E. Owen, "The hole drift mobility of vitreous selenium," *Physica Status Solidi A*, vol. 12, pp. 181–191, 1972.

[54] T. E. Orlowski and M. Abkowitz, "Microstripline transient photocurrents in a-Se structure resolved in shallow band tail states," *Solid State Connnunications*, vol. 59, pp. 665–668, 1986.

[55] M. Abkowitz, "Evidence of the defect origin of states which control photoelectric behavior of amorphous chalcogenides," *Joumal of Non-Crystalline Solids*, vol. 66, pp. 315–320, 1984.

[56] ——, "Relaxation induced changes in electrical behavior of glassy chalcogenide semiconductors," *Polymer Engineering Science*, vol. 24, pp. 1149–1154, 1984.

[57] M. Abkowitz and J. M. Markovics, "Evidence of equilibrium native defect populations in amorphous chalcogenides from analysis of xerographic spectra," *Philosophical Magazine B*, vol. 49, pp. L31–L36, 1984.

[58] S. Kasap and J. A. Rowlands, "Review: X-ray photoconductors and stabilized a-Se for direct conversion digital flat-panel x-ray image detectors," *Journal of Materials Science: Materials in Electronics*, vol. 11, pp. 179–198, 2000.

[59] D. M. Pai, "Time-of-fight study of the compensation mechanism in a-Se alloys," *Journal of Imaging Science and Technology*, vol. 41, pp. 135–142, 1997.

[60] H. Song, G. Adriaenssens, E. Emelianova, and V. Arkhipov, "Distribution of gap states in amorphous selenium thin films," *Physics Review B*, vol. 59, pp. 10 607–10 613, 1999.

[61] J. L. Hartke and P. J. Regensburger, "Electronic states in vitreous selenium," *Physical Review*, vol. 139, pp. A970–A980, 1965.

[62] E. Davis, "Optical absorption, transport and photoconductivity in amorphous selenium," *Journal of Non-Crystalline Solids*, vol. 4, pp. 107–116, 1970.

[63] H. Adachi and K. Kao, "Dispersive optical constants of amorphous selenium films," *Journal of Applied Physics*, vol. 51, pp. 6326–6331, 1980.

[64] W. Spear, "Drift mobility techniques for the study of electrical transport properties in insulating solids," *Journal of Non-Crystalline Solids*, vol. 1, pp. 197–214, 1969.

[65] B. Polischuk, "Interrupted field time-of-flight transient photoconductivity technique and its applications to amorphous semiconductors," Ph.D. dissertation, Saskatchewan, 1993.

[66] M. Martini, J. Mayer, and K. Zanio, *Drift velocity and trapping in semiconductors.* Academic Press, 1972, vol. 3, ch. Transient Charge Technique, pp. 181–258.

[67] R. M. Blakney and H. P. Grunwald, "Small-signal current transients in insulators with traps," *Phys. Rev.*, vol. 159, pp. 658–664, Jul 1967. [Online]. Available: http://link.aps.org/doi/10.1103/PhysRev.159.658

[68] C. Allen, G. Belev, R. Johanson, and S. Kasap, "Relaxation of the electrical properties of vacuum-deposited a-Se1-xasx photoconductive films: Charge-carrier lifetimes and drift mobilities and films," *Journal of Vacuum Science & Technology A: Vacuum, Surfaces*, vol. 28, no. 5, pp. 1145–1156, 2010.

[69] Haugen, S. Kasap, and J. A. Rowlands, "Charge transport and electronhole-pair creation energy in stabilized a-Se x-ray photoconductors," *J. Phys. D.*, vol. 32, pp. 200–2007, 1999.

[70] S. Kasap, R. Thakur, and D. Dodds, "Method and apparatus for interrupted transit time transient photoconductivity measurements," *Journal of of Physics E: Scientific Instrumentation*, vol. 21, pp. 1195–1202, 1988.

[71] W. Helfrich and P. Mark, "Space charge limited currents in anthracine as a means of determining the hole drift mobility," *Zeitschrift Fur Physik*, vol. 166, pp. 370–385, 1962.

[72] B. Polischuk and S. Kasap, "A high-voltage interrupted-field time-of-fight transient photoconductivity apparatus," *Measurement Science & Technology*, vol. 2, pp. 75–80, 1991.

[73] J. Beutel and H. Kundel, *Handbook of medical imaging*, 2000.

[74] K. Bevington and D. Robinson, *Data reduction and error analysis for the physical sciences.* McGraw-Hill, 1969.

[75] S. Mahmood, M. Kabir, O. Tousignant, and J. Greenspan, "Investigation of ghosting recovery mechanisms in selenium x-ray detector structures for mammography," *Nuclear Science, IEEE Transactions on*, vol. 59, no. 3, pp. 597–604, 2012.

[76] H. Fritzsche and T. Az, "Search for explaining the staebler-wronski effect," *MRS Proceedings*, vol. 467, 0 1997. [Online]. Available: http://journals.cambridge.org/article_S1946427400316736

[77] E. M. Petrie, *Handbook of adhesives and sealants*. McGraw-Hill New York, 2000.

[78] S. Bishop, U. Strom, and P. Taylor, "Optically induced localized paramagnetic states in chalcogenide glasses," *Physical Review Letters*, vol. 34, no. 21, pp. 1346–1350, 1975.

[79] ——, "Optically induced metastable paramagnetic states in amorphous semiconductors," *Physical Review B*, vol. 15, no. 4, p. 2278, 1977.

[80] K. Tanaka and A. Odajima, "Photodarkening in amorphous selenium," *Solid State Communications*, vol. 43, no. 12, pp. 961–964, 1982.

[81] K. Tanaka, "Photoinduced structural changes in chalcogenide glasses," *Rev. Solid State Sci*, vol. 4, pp. 641–659, 1990.

[82] G. Pfeiffer, M. Paesler, and S. Agarwal, "Reversible photodarkening of amorphous arsenic chalcogens," *Journal of non-crystalline solids*, vol. 130, no. 2, pp. 111–143, 1991.

[83] K. Shimakawa, A. Kolobov, and S. Elliott, "Photoinduced effects and metastability in amorphous semiconductors and insulators," *Advances in Physics*, vol. 44, no. 6, pp. 475–588, 1995.

[84] S. O. Kasap, V. Aiyah, A. Baillie, and A. G. Leiga, "X-ray induced hole trapping in electroradiographic plates," *Journal of Applied Physics*, vol. 69, no. 10, pp. 7087–7096, 1991.

[85] L. Baetz. (2013, April) Simulation of x-ray spectra. https://w9.siemens.com/cms/oemproducts/home/x-raytoolbox/spektrum/pages/default.aspx.

[86] K. Shimakawa, K. Fukami, H. Kishi, G. Belev, and S. Kasap, "X-ray induced effects on photocurrents in amorphous Se films," *Japanese journal of applied physics*, vol. 46, pp. L192–L195, 2007.

[87] M. Z. Kabir, M. Yunus, S. Kasap, O. Tousignant, H. Mani, and P. Gauthier, "Sensitivity of stabilized a-Se based x-ray photoconductors," *Current Applied Physics*, vol. 6, no. 3, pp. 393–398, 2006.